LEON DE MORAIS NUNES

COMPUTATIONAL FLUID DYNAMICS APPLICATION FOR GAS-POWDER FLOW INVESTIGATION IN A COAXIAL NOZZLE DESIGN FOR ADDITIVE MANUFACTURING

UNIVERSIDADE FEDERAL DE UBERLÂNDIA
FACULDADE DE ENGENHARIA MECÂNICA
2022

LEON DE MORAIS NUNES

APLICAÇÃO DE FLUIDODINÂMICA COMPUTACIONAL PARA INVESTIGAÇÃO DE ESCOAMENTO GÁS-PARTICULADO NO PROJETO DE UM BOCAL COAXIAL PARA MANUFATURA ADITIVA

UNIVERSIDADE FEDERAL DE UBERLÂNDIA
FACULDADE DE ENGENHARIA MECÂNICA
2022

LEON DE MORAIS NUNES

COMPUTATIONAL FLUID DYNAMICS APPLICATION FOR GAS-POWDER FLOW INVESTIGATION IN A COAXIAL NOZZLE DESIGN FOR ADDITIVE MANUFACTURING

Dissertação apresentada ao Programa de Pós-graduação em Engenharia Mecânica da Universidade Federal de Uberlândia, como parte dos requisitos para a obtenção do título de **MESTRE EM ENGENHARIA MECÂNICA**.

Área de concentração: Mecânica dos Fluidos

Orientador: Prof. Dr. Aristeu da Silveira Neto

Coorientador: Prof. Dr. Arthur Alves Fiocchi

UBERLÂNDIA - MG

2022

Ficha Catalográfica Online do Sistema de Bibliotecas da UFU
com dados informados pelo(a) próprio(a) autor(a).

N972
2022

Nunes, Leon de Morais, 1993-
COMPUTATIONAL FLUID DYNAMICS APPLICATION FOR GAS-POWDER FLOW INVESTIGATION IN A COAXIAL NOZZLE DESIGN FOR ADDITIVE MANUFACTURING [recurso eletrônico] / Leon de Morais Nunes. - 2022.

Orientador: Aristeu da Silveira Neto.
Coorientador: Arthur Alves Fiocchi.
Dissertação (Mestrado) - Universidade Federal de Uberlândia, Pós-graduação em Engenharia Mecânica.
Modo de acesso: Internet.
Disponível em: http://doi.org/10.14393/ufu.di.2021.59
Inclui bibliografia.
Inclui ilustrações.

1. Engenharia mecânica. I. Silveira Neto, Aristeu da , 1955-, (Orient.). II. Fiocchi, Arthur Alves,1981-, (Coorient.). III. Universidade Federal de Uberlândia. Pós-graduação em Engenharia Mecânica. IV. Título.

CDU: 621

Bibliotecários responsáveis pela estrutura de acordo com o AACR2:
Gizele Cristine Nunes do Couto - CRB6/2091
Nelson Marcos Ferreira - CRB6/3074

UNIVERSIDADE FEDERAL DE UBERLÂNDIA
Coordenação do Programa de Pós-Graduação em Engenharia Mecânica
Av. João Naves de Ávila, nº 2121, Bloco 1M, Sala 212 - Bairro Santa Mônica, Uberlândia-MG, CEP 38400-902
Telefone: (34) 3239-4282 - www.posmecanicaufu.com.br - secposmec@mecanica.ufu.br

ATA DE DEFESA - PÓS-GRADUAÇÃO

Programa de Pós-Graduação em:	Engenharia Mecânica				
Defesa de:	Dissertação de Mestrado Acadêmico, nº 617, PPGEM				
Data:	29/08/2022	Hora de início:	14:00	Hora de encerramento:	15:50
Matrícula do Discente:	12012EMC016				
Nome do Discente:	Leon de Morais Nunes				
Título do Trabalho:	Computational fluid dynamics application for gas-powderflow investigation in a coaxial nozzle design process for additive manufacturing				
Área de concentração:	Transferência de Calor e Mecânica dos Fluidos				
Linha de pesquisa:	Dinâmica dos Fluidos e Transferência de Calor				
Projeto de Pesquisa de vinculação:					

Reuniu-se por meio de videoconferência a Banca Examinadora, designada pelo Colegiado do Programa de Pós-graduação em Engenharia Mecânica, assim composta: Professores Doutores: Arthur Alves Fiocchi (coorientador) - FEMEC/UFU; Francisco José de Souza - FEMEC/UFU; Alexandre Megiorin Roma - USP/SP; e Aristeu da Silveira Neto - FEMEC/UFU, orientador do candidato.

Iniciando os trabalhos o presidente da mesa, Dr. Aristeu da Silveira Neto, apresentou a Comissão Examinadora e o candidato, agradeceu a presença do público, e concedeu ao Discente a palavra para a exposição do seu trabalho. A duração da apresentação do Discente e o tempo de arguição e resposta foram conforme as normas do Programa.

A seguir o senhor(a) presidente concedeu a palavra, pela ordem sucessivamente, aos(às) examinadores(as), que passaram a arguir o(a) candidato(a). Ultimada a arguição, que se desenvolveu dentro dos termos regimentais, a Banca, em sessão secreta, atribuiu o resultado final, considerando o(a) candidato(a):

Aprovado.

Esta defesa faz parte dos requisitos necessários à obtenção do título de Mestre.

O competente diploma será expedido após cumprimento dos demais requisitos, conforme as normas do Programa, a legislação pertinente e a regulamentação interna da UFU.

Nada mais havendo a tratar foram encerrados os trabalhos. Foi lavrada a presente ata que após lida e achada conforme foi assinada pela Banca Examinadora.

Documento assinado eletronicamente por **Aristeu da Silveira Neto**, **Professor(a) do Magistério Superior**, em 29/08/2022, às 15:57, conforme horário oficial de Brasília, com fundamento no art. 6º, § 1º, do Decreto nº 8.539, de 8 de outubro de 2015.

Documento assinado eletronicamente por **Arthur Alves Fiocchi**, **Professor(a) do Magistério Superior**, em 29/08/2022, às 15:57, conforme horário oficial de Brasília, com fundamento no art. 6º, § 1º, do Decreto nº 8.539, de 8 de outubro de 2015.

Documento assinado eletronicamente por **Francisco José de Souza**, **Professor(a) do Magistério Superior**, em 29/08/2022, às 15:57, conforme horário oficial de Brasília, com fundamento no art. 6º, § 1º, do Decreto nº 8.539, de 8 de outubro de 2015.

Documento assinado eletronicamente por **Alexandre Megiorin Roma**, **Usuário Externo**, em 29/08/2022, às 15:58, conforme horário oficial de Brasília, com fundamento no art. 6º, § 1º, do Decreto nº 8.539, de 8 de outubro de 2015.

A autenticidade deste documento pode ser conferida no site https://www.sei.ufu.br/sei/controlador_externo.php?acao=documento_conferir&id_orgao_acesso_externo=0, informando o código verificador **3874249** e o código CRC **7853452A**.

"I dedicate this dissertation to my parents, Sonia and Amauri, for always
been here for me".

AGREDECIMENTOS

Primeiramente, gostaria de agradecer ao Prof. Dr. Aristeu da Silveira Neto e ao Prof. Dr. Arthur Alves Fiocchi, por terem me dado esta maravilhosa oportunidade de poder desenvolver um trabalho multidisciplinar dentro das áreas de Mecânica de Fluidos e Manufatura Aditiva. Agradeço imensamente também ambos pelo aprendizado, constantes ensinamentos, conselhos e principalmente pela paciência que tiveram comigo durante o desenvolvimento deste trabalho. Agradeço a todos os meus colegas dos laboratórios: Laboratório de Mecânica de Fluidos (MFLab) e ao Laboratório de Ensino e Pesquisa em Usinagem (LEPU) da Universidade Federal de Uberlândia, pela ajuda e conselhos de sempre. Agradeço muito a minha colega e amiga de curso Ana Paula Moreira por sempre ter estado disposta a me ajudar no que foi preciso.

Agradeço muito ao meu pai, Amauri pelos conselhos e ajuda de sempre. Agradeço muito minha mãe Sonia por sempre ter sido a pessoa que sempre me escutou e dedicou seu tempo a mim. Agradeço ao meu irmão Lucius, minha sobrinha Micaela e minha cunhada Juliana todo o apoio e carinho de sempre. Agradeço a minha avó Bia toda a confiança e orgulho que sempre depositou em mim. Agradeço à Cristiane todo o carinho, amor e companheirismo que sempre me mostrou e toda a ajuda e energia positivas que me deu, principalmente nos momentos mais complicados. Obrigado por sempre estar ao meu lado. Agradeço a todos os meus amigos e amigas que estiveram, perto ou longe, me dando todo o suporte e carinho desde sempre.

Agradeço ao imenso apoio da Ambev, Ambev Tech e Beer Garage. Em especial agradeço ao meu time do Chapter de Pesquisa e Desenvolvimento por terem me apoiado e confiado desde sempre no meu trabalho e pelas inúmeras dicas e conselhos.

Agradeço ao Conselho Nacional de Desenvolvimento Científico e Tecnológico (CNPq) pelo suporte financeiro e agradeço à Faculdade de Engenharia Mecânica da Universidade Federal de Uberlândia, juntamente com todo o corpo docente, em especial os docentes que lecionaram os cursos os quais participei, por todo o ensinamento e suporte aportados.

Agradeço à FAPEMIG pelo apoio por meio do Projeto de Pesquisa APQ-01759-17. Agradeço às empresas e aos responsáveis dos softwares gratuitos que eu utilizei, como Solid Edge® e o Ansys Fluent®.

Por fim, agradeço a Deus pelo dom da vida, do conhecimento e por ter sempre estado ao meu lado dando forças para seguir em frente e finalizar esta pesquisa.

NUNES, L., **Computational Fluid Dynamics Application for Gas-Powder flow Investigation in a Coaxial Nozzle Design for Additive Manufacturing** 2022. 141 f. Master Thesis, Universidade Federal de Uberlândia, Uberlândia.

ABSTRACT

Direct Energy Deposition (DED) is one of the seven Additive Manufacturing (AM) classes. It is increasingly used to repair and construct parts in the industry. The DED methodology uses heat to melt the substrate and the deposited material. There are different ways to perform this task, and over the years, additional patents and methods appeared. Other materials can be applied, such as metals, ceramics, polymers as well as mixtures, to produce composite materials. The nozzle plays an essential role in the overall process and studying its influence and mechanical design aspects is crucial. Computational Fluid Dynamics (CFD) is an important engineering tool, and it is being widely used for better and fast design. The use of a CFD tool to optimize the nozzle and improve the deposition system can be a quick and efficient way to increase the overall efficiency of this type of machine. The gas-solid model proposed in this current study improved the knowledge about particle transportation using a nozzle, and it was verified that for a low Reynolds Number, the higher the Stokes Number, the higher the particle Concentration on the desired area of deposition. It was also confirmed that decreasing the Reynolds Number implies an increase in particle Concentration. Considering higher Reynolds Numbers, Re = 1 000 and Re = 1 250, it was concluded that there is no pattern for the particle Concentration due to the agglomeration formation, changing the shape of the particles and generating a new solid body, modifying the drag force and, then, the particle deposition behavior. The research developed on this dissertation helped to understand the particle behavior considering different flow regimes applied for a range of multiple Reynolds and Stokes Numbers. It was possible, as well, to map the particle deposition pattern behavior and to understand the effects of the fluid flow over the particle concentration on the deposition point.

Keywords: CFD, simulation, metal deposition, DED, LENS, LMD, turbulence, multiphase flows, fluid mechanics.

NUNES, L., **Aplicação de Fluidodinâmica Computacional para Investigação de Escoamento Gás Particulado no Projeto de um Bocal Coaxial para Manufatura Aditiva,** 2022. 141 f. Dissertação de Mestrado, Universidade Federal de Uberlândia, Uberlândia.

RESUMO

Direct Energy Deposition (DED) ou Deposição de Energia Direcionada (DED) é uma das sete classes de manufatura aditiva (MA). É um processo que vem cada vez mais sendo usado para as áreas de reparo e construção de peças na indústria. A metodologia DED consiste no aquecimento até a fusão do substrato e do material depositado. Existem diferentes maneiras de realizar esta tarefa e ao longo dos anos diferentes patentes e métodos surgiram. Diferentes materiais podem ser utilizados tais como metais, cerâmicas, polímeros bem como misturas para produzir materiais compósitos. O bocal apresenta um papel importante no processo global e estudar sua influência e aspectos do seu projeto mecânico são pontos cruciais. A Fluido Dinâmica Computacional (Computational Fluid Dyanmics, CFD) é uma importante ferramenta e está sendo utilizada amplamente para um melhor e mais rápido desenvolvimento de projeto. O uso de ferramentas como o CFD para otimizar o bocal e melhorar o sistema de deposição pode ser uma rápida e eficiente forma de aumentar a eficiência global deste tipo de máquina. O modelo gás-sólido proposto na segunda etapa das simulações realizadas melhorou o conhecimento sobre o transporte de partículas utilizando um bocal, e foi verificado no mesmo que para um baixo Número de Reynolds, quanto maior o Número de Stokes maior será a Concentração de partículas. Também foi verificado que reduzindo-se o Número de Reynolds implica em um aumento na Concentração das partículas. Considerando altos Número de Reynolds, Re = 1 000 e Re = 1 250, pode-se concluir que não existiu um padrão para a Concentração de partículas, devido à aglomeração delas, modificando-se a forma das mesmas e gerando-se um corpo sólido o que implicou na modificação da força de arrasto, e, por consequência, o padrão de deposição. A pesquisa realizada nesta dissertação ajudou a entender o comportamento das partículas considerando diferente regimes de escoamento aplicados para uma variação nos Número de Reynolds e Stokes. Foi possível, também, mapear o padrão de deposição das partículas e entender os efeitos do escoamento do fluido sobre a concentração das partículas no ponto de deposição

Palavras-chave: FDC, simulação, deposição metálica, DED, LENS, LMD, turbulência, escoamentos multifásicos, mecânica de fluidos.

GLOSSARY

The axisymmetric condition is the problem using an axisymmetric axis in the domain, computing cylindrical effects from three-dimension geometries to two-dimension geometries.

The axisymmetric axis is the axis used in the axisymmetric boundary conditions.

The boundary conditions are the constraints necessary to solve a boundary value problem.

The carrier gas is the gas used to transport solid particles up to the deposition area.

The deposition angle is the inclination angle with the nozzle vertical center line (or nozzle spin line).

The feeding rate is the particle mass flow rate feeding the carrier channel in the deposition nozzle.

Laser power is a way to control the amount of energy absorbed by a deposition area.

The laser pulse type is the classification of different types of non-continuous-wave lasers.

The mesh cell number is the number of cells in each mesh for a specific geometry, directly related to the mesh and simulation quality.

The mesh size represents the dimensions of a give cell used in the proposed mesh**.**

The mesh quality is a mesh characteristic that permits high-fidelity numerical PDE simulations, following the real physics of the problem.

The particle flux is the gas-powder flow over the deposition area.

The particle size is the particle diameter for a given particle cloud used.

The shield gas is the gas used to protect the deposition area atmosphere, usually coming from another nozzle channel.

The scanning velocity is the machine’s longitudinal velocity, usually numerically controlled (CNC).

The standoff distance is the distance between the nozzle tip and the last deposited layer.

The substrate is the building surface for fusing to a part being formed.

The simulation convergence criteria are when the simulation’s previously defined errors are below a given reference value.

The simulation time step is a fixed amount of time by the way a given simulation advances.

The work atmosphere is the medium where a deposition process is performed.

TERMOS TÉCNICOS INGLÊS/PORTUGUÊS

3D multiphase model: modelo multifásico 3D.

Additive manufacturing: manufatura aditiva.

Aerospace materials repair: reparo de materiais aeroespaciais.

Argon: argônio.

Axial axisymmetric jet: jato axial axissimétrico.

Carrier gas: gás transportador.

Catchment efficiency: eficiência de captação (pelo substrato).

Ceramic coating: revestimento cerâmico.

Composites: compósitos.

Computational Fluid Dynamics: fluidodinâmica Computacional.

Control system: sistema de controle.

Cooper: cobre.

Cracking: trincamento.

Deposition head: sistema completo de deposição: incluindo o laser.

Dilution levels: níveis de diluição.

Direct Energy Deposition: deposição de Energia Direcionada.

Discrete phase model: modelo de fase discreta.

Droplet: gotícula.

Feeding mechanism: mecanismo de alimentação.

Flow pattern: padrão (modo) do escoamento.

Focal position: posição focal.

Grooves: ranhuras.

Hardness: dureza.

Heat transfer: transferência de calor.

Heat treatment: tratamento Térmico.

Inert atmosphere: atmosfera inerte.

Laser beam: feixe de Laser.

Laser cladding process: processo de revestimento com laser.

Laser Melt Deposition: deposição por fusão à laser

Laser pulse shape: forma do pulso de laser.

Laser-based direct metal deposition: deposição direta de metal à base de laser.

Layer solidification: solidificação da camada.

Low-pressure turbine blades: palhetas do estágio de baixa pressão de turbinas.

Melt pool: poça de fusão.

Microstructure: microestrutura.

Natural Convection: convecção natural.

Neutron analysis: análise com o uso de nêutrons.

Nozzle: bocal.

Overheating: sobreaquecimento.

Porosity: porosidade.

Powder feed position: posição do alimentador de particulado em pó.

Powder feed rate: taxa de alimentação (de particulado em pó).

Powder flux: fluxo de particulado em pó.

Powder-gas: gás-particulado.

Pre-heating system: sistema de pré-aquecimento.

Pre-mixed powder: particulado em pó pré-misturado.

Residual stress: tensões residuais.

Ricochet effect: efeito de Ricochete.

Scanning velocity (speed): velocidade de Varredura.

Setup: configuração.

Shield gas: gás protetivo.

Solenoid valve: válvula solenoide.

Stand off distance: distância de afastamento (do substrato).

Substrate: substrato.

Track formation: formação do caminho de deposição.

Turbulent intensity: intensidade de turbulência.

Vacuum: vácuo.

X-ray diffraction: difração de raio-x.

SYMBOLS, ACRONYMS, AND OPERATORS USED

C: Particle Concentration or DPM Concentration (Ansys Fluent®)

C_D: Drag coefficient

CFD: Computational Fluid Dynamics

DED: Direct Energy Deposition

DPM: Discrete Particle Model

d_p: Particle diameter

k: Turbulent kinetic energy

LBMD: Laser Based Metal Deposition

Ra: Average arithmetic deviation of the evaluated profile in µm

RANS: Reynolds-Averaged Navier-Stokes equations

Re: Reynolds Number

SST-kω: Shear Stress Tensor kω turbulence model

St: Stokes Number

t: Time

URANS: Unsteady Reynolds-Averaged Navier-Stokes equations

$\overline{u_i'u_j'}$: Reynolds tensor

Δ: Variation

∂: Partial derivative

$\vec{\nabla}()$: Gradient

$\vec{\nabla}.()$: Divergent

$d()$: Ordinary derivative

$\tilde{()}$: Filtering operator

µ: Dynamic viscosity

μ_t: Turbulent dynamic viscosity

N: Kinematic viscosity

ν_t: Turbulent kinematic viscosity

ρ: Density

τ_{ij}: Tensor de Reynolds sub-malha

τ_p: Tempo de relaxação

Δ_t: Time step

LIST OF FIGURES

Figure 3.4 - Probe points position on the geometry. These probes were placed in the positions to capture the velocities in the regions with higher gradients…………………………………60
Figure 3.5 - Boundary Conditions used on the current study 1, including the Axisymmetric axis used to replicate the cylindrical condition………………………………………………..61

LIST OF TABLES

CONTENTS

CHAPTER I

INTRODUCTION

According to Sargent and Schwartz (2019), three-dimensional (3D) printing or also known as additive manufacturing (AM) is a fast and highly flexible manufacturing process that has been gain space in product design and product manufacturing for the past 30 years. The vast expansion of 3D printing is mainly due to good capabilities, low prices, and the diversity of materials that can be used (SARGENT;SCHWARTZ, 2019). Different industries, like aerospace and medical, adopted 3D printing to build their projects (SARGENT;SCHWARTZ, 2019).

3D printers have four primary properties that make this process a unique construction method (SARGENT AND SCHWARTZ, 2019): reduced waste, capacity to create parts with high internal complexity, cost reduction for small productions, and ease of design change. For this reason, the technology is expanding considerably between industries, accounting for 5 % to 10 % of manufacturing in the long term (SARGENT AND SCHWARTZ, 2019).

Annual grants dedicated to 3D printing-related patents more than doubled, from 247 in 2010 to 545 in 2015 (HORNICK, 2017). According to Campbell *et al.* (2019), consumer unit sales increased by 49,4 %. Analyzing the Wohlers Report 2020, the global market size of AM industry was over USD 11 billion in 2019 (WOHLERS, 2020). The perspective is growing up to over USD 35 billion by 2024. The importance of the AM was genuinely highlighted in the fight against the COVID-19 pandemic (LARRANETA; DOMINGUEZ-ROBLES; LAMPROU, 2020), being a critical factor in speeding up the production of essential hospital components like the valves for respiratory machines and personal protective equipment. Javaid and Haleem (2019) presented in their study the status and applications of AM in dentistry, including the elaboration of dental crowns, bridges, and orthodontic braces. Other examples are shown in Figure 1.1.

This technology includes different processes applied to other classes of materials. According to the ASTM F2792-10 standard (2012), AM technologies can be classified into seven categories: binder jetting, directed energy deposition, material extrusion, material jetting, powder bed fusion, sheet lamination, and vat photopolymerization. Zeng *et al.* (2016) created a table based on the ASTM F2792-10 standard (2012). It is shown in Table 1.1 the different processes. This classification above regards the AM technologies and materials used for various applications. It is possible also to classify the other methods considering how the material is deposited, as Guo and Leu (2013) described, considering the material feeding in liquid form, filament/paste form, powder form, or solid sheet form.

Figure 1.1 - Other AM applications in dentistry. These ten classes represent different dental area applications from education to teeth repair.

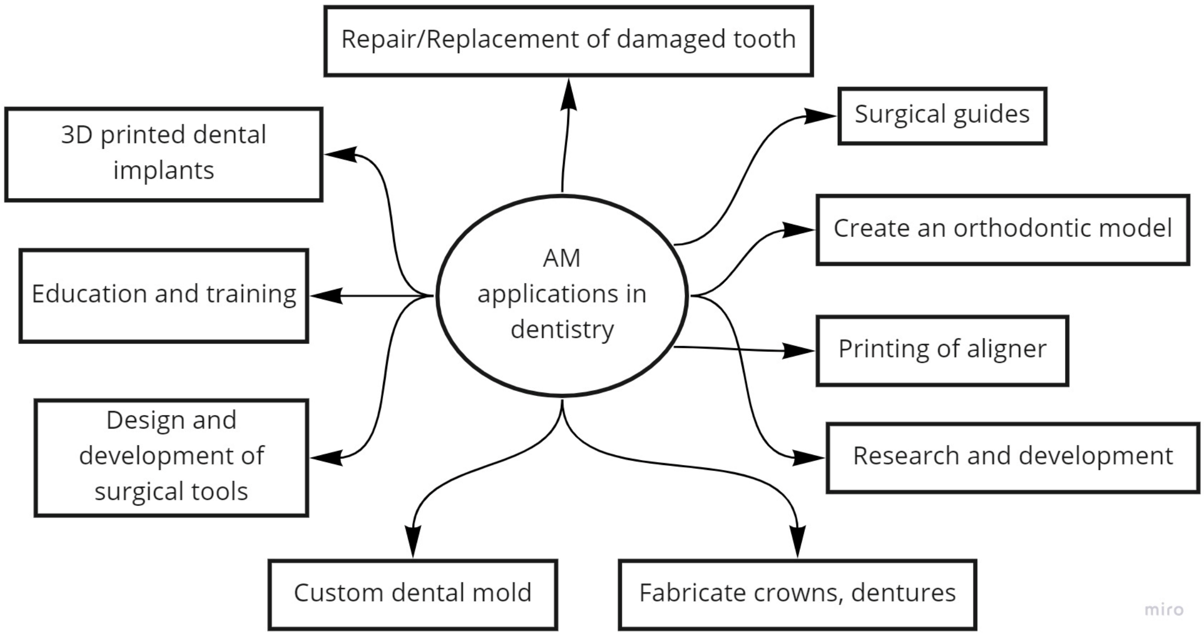

Source: Adapted from Javaid and Haleem, 2019.

Gibson *et al.* (2015) describe Direct Energy Deposition (DED) as creating solid 3D parts using heat to melt the material and the substrate. This process can work for ceramics, polymers, and metal matrix composites but is broadly applied to metals and their alloys. The system for this application uses energy, usually a laser or electron beam, in a narrow and focused region to heat the substrate and the deposited material. Both substrate and material are melted when the deposition occurs, different from the powder bed fusion techniques. The DED process schematic is shown in Figure 1.2.

Figure 1.2 - Example of DED nozzle with the main components including the shielding gas channel, the laser beam channel, and the carrier channel (powder transportation).

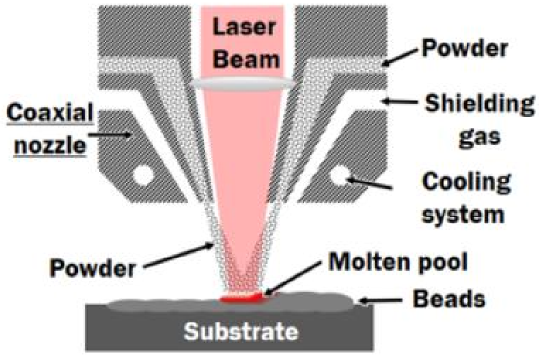

Source: adapted from Javaid and Haleem, 2019.

Different DED machine concepts were developed (GIBSON *et al.*, 2015). Some of these machines are Laser Engineered Net Shaping (LENS, KEICHER AND MILLER, 1998), Directed Light Fabrication (LEWIS *et al.*, 1994), Direct Metal Deposition (DMD), 3D Laser Cladding, Laser Generation, Laser-Based Metal Deposition, Laser Freeform Fabrication (LFF), Laser Direct Casting, LaserCast (HOUSE *et al.*, 1996), Laser Consolidation, LasForm, and others as described by Gibson *et al.* (2015). It is also verified that the laser cladding and Laser Metal Deposition (LMD) processes are the same as the others but with a different name, considering different patents.

Although all these machines have almost the same approach, they usually differ in the laser power used and the laser type, spot size, powder, inert gas delivery method, and feedback and motion control (GIBSON *et al.*, 2015). Svetlizky et al. (2021) reviewed the main DED physical characteristics and defects, including the challenges and the critical variables. Considering the blown-powder DED process, there are three main divisions for these variables: system specifications dependent, feedstock (powder) dependent, and deposition process dependent (SVETLIZKY *et al.*, 2021). The main variables are presented in Figure 1.4. Developing in situ monitoring techniques with closed-loop adaptative control have recently been developed (SVETLIZKY *et al.*, 2021). Besides that, numerical simulations help to predict different process conditions and applications. It is shown in Figure 1.5 the description of a workflow simulation of a compositionally grade rocket nozzle processing (SVETLIZKY *et al.*, 2021).

Table 1.1: AM processes categories. Source: Zeng *et al.* (2016) and ASTM F2792-10.

Process category	**Specific technology**	**Corresponding Materials**
Vat photopolymerization	Stereolithography - SLA	UV curable resins
Material jetting	MJM (MultiJet Modeling)	Waxes, ceramics, UV curable resins
Binder jetting	3DP (3D printing)	Waxes, composites, polymer, ceramics, metals
Material extrusion	Fused Deposition Modeling - FDM	Thermoplastics
Powder bed fusion	Selective Laser Sintering - SLS	Waxes, thermoplastics, metals
Powder bed fusion	Selective Laser Melting - SLM	Waxes, thermoplastics, metals
Powder bed fusion	Electron Beam Melting – EBM	Waxes, thermoplastics, metals
Sheet Lamination	Laminated Object Manufacturing - LOM	Paper, metals, thermoplastics
Directed energy deposition	Laser Metal Deposition - LMD	Metals
Directed energy deposition	Laser-Engineering Net Shaping - LENS	Metals
Directed energy deposition	Direct Metal Deposition - DMD	Metals
Directed energy deposition	Direct Laser Deposition - DLD	Metals
Directed energy deposition	Electron-Beam Additive Manufacturing - EBAM	Metals

Online in-situ monitoring is still a big challenge for DED processes. Detecting defects in real-time with sufficient response time, for example, controlling the powder stream distribution is still a limiting factor for DED AM procedures (SVETLIZKY *et al.*, 2021). For the specific case of powder stream flux control and prediction, an essential tool is Computational Fluid Dynamics (CFD).

Fluid mechanics is an engineering branch focused on the fluids (gas or liquids) in movement (fluid dynamics) or at rest (fluid static) (WHITE, 1979). Multiple applications are related to the understanding and analysis of flow behavior. Examples include the study of a vessel's blood flow, airflow inside the lungs, oil transport inside the pipelines, an airplane airfoil design, and even a building or bridge project. Thus, it becomes an essential subject for any engineering project. Inherently to the fluid flow, there is a classification regarding the flow dynamic, where the flow may be laminar or turbulent.

The turbulence is present not just in the flow dynamics analysis but in public life, any situation or system where there is a high dynamism with an extremely high number of degrees of freedom, as Silveira-Neto (2020) pointed out. Considering the Fluid Mechanics application (SILVEIRA-NETO, 2020), the turbulence phenomenon is characterized by multiple dynamics structures, with different topological shapes and complexity levels directly influenced by the Reynolds Number (Re) that the bigger the Re, the more complex the structures. These structures are presented in different wavenumbers and will interact with each other in a highly nonlinear and simultaneous way, evidencing the multiplicity of these phenomenon characteristics quantities.

Figure 1.3 - DED main parameters, including the system specifications and all the deposition variables.

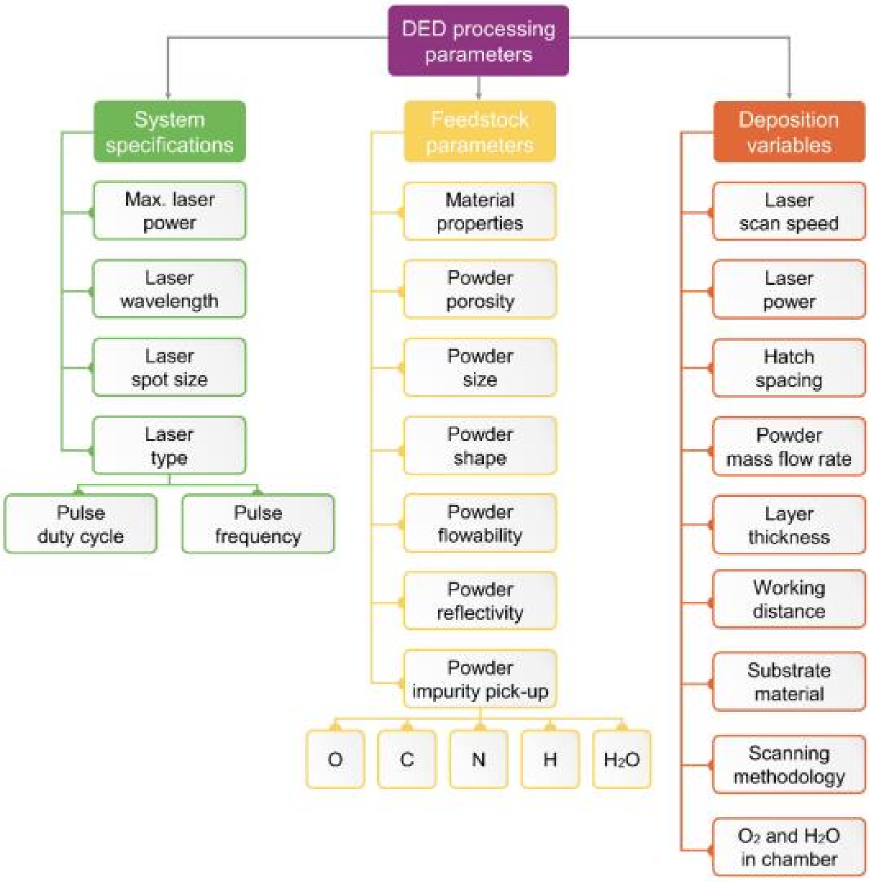

Source: Svetlizky *et al.*, 2021.

The phenomenon will also be continuous because the minor structures will be much bigger than the mean free path, and the deterministic chaos will govern it, that is, extremely dependent on the initial conditions (and dependent also on the solution conditions, considering the numerical analysis). The turbulence will increase molecular diffusion because it increases the local gradients. The turbulent flows are also rotational, three-dimensional, and transformative. That is, there is the transformation of mean flow internal energy in turbulent kinetic energy, turbulent kinetic energy in thermal energy, and potential energy in turbulent kinetic energy.

Figure 1.4 - Flow chart for DED AM of a rocket critical component combined with Finite Element Model simulation.

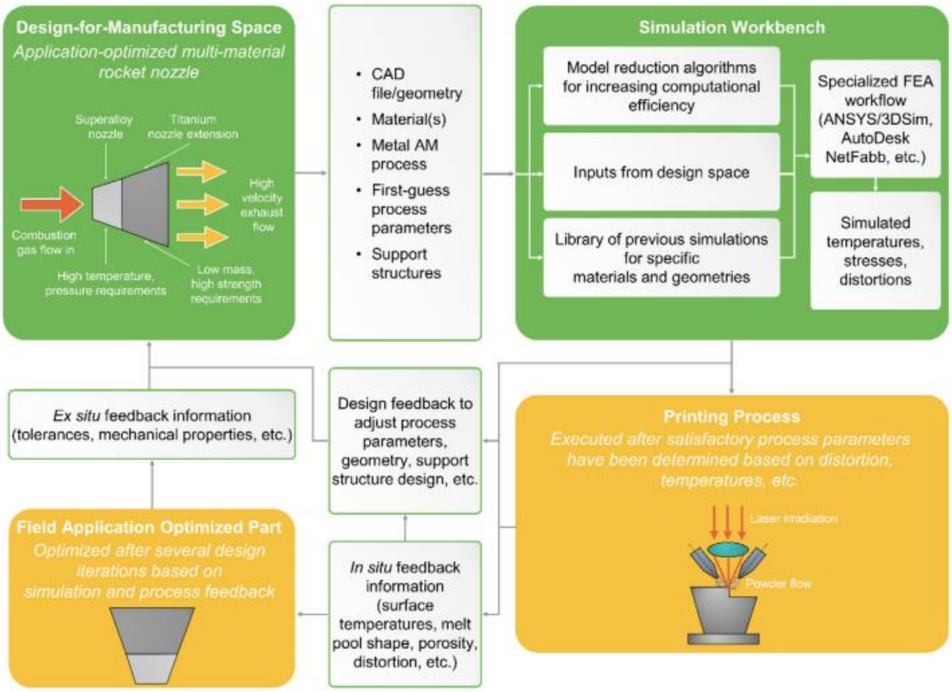

Svetlizky *et al.*, 2021.

According to Silveira-Neto (2020), modeling a physical phenomenon is a way to represent this phenomenon. This can be done by a physical model, a theoretical model, or a material model. A simulation will be based either on the material or theoretical models. Thus it is possible to have different kinds of simulations, theoretical or even material ones. However, even a material experiment, a mathematical model, or a computational model will be physical representations of reality, so all of them will be physical models, as pointed out by Silveira-Neto (2020). Considering the theoretical modeling, CFD is increasingly taking place over the years. The CFD application started around the middle of the 1960s, with some successful cases in the 1970s and starting with industrial applications around the 1980s (MOREIRA, 2011). Initially, according to Johnson; Tinoco; Yu (2005), the development method was almost entirely made by analytic approximation methods of Navier-Stokes equations and wind tunnel tests. Today is an essential part of any machine that works or is affected by any flow. In 2002, more than 20000 CFD cases were run on Boeing Facilities (JOHNSON; TINOCO; YU, 2005).

CFD can be described as the flow dynamic analysis using a computational approach using a numerical model (VERSTEEG; MALALASEKERA, 2007; FERZIGER; PERI, 2002; POPE, 2001). Once it needs a powerful computational capacity, it is logical to link the CFD evolution with the computational power evolution and algorithm breakthrough, as shown by Johnson; Tinoco; Yu (2005). CFD modeling can simulate multiple designs at an inexpensive cost (JOHNSON; TINOCO; YU, 2005), and this is a crucial point for airplane design companies like Boeing or Embraer. The computational evolution that allowed the CFD implementation is linked to hardware improvement and better algorithms and computational methods. However, as Moreira (2011) pointed out, the main contributor was the evolution of numerical methods, including discretization and solution schemes. For example, in 1980, the max node points used was 3454; in 2000, this number increased to 1,2 million node points (VOLLER; PORT-ANGEL, 2002).

CFD simulation can have multiple applications in science and industry and is increasingly critical in project optimization and cost reduction. Gimenes et al. (2008) optimized gas sensor positioning using a CFD tool to study the gas dispersion in an oil platform. Silva; Silveira-Neto; Vale (2014) studied the droplet breakup effect using a two-way Euler-Lagrange CFD simulation. The breakup phenomenon is fundamental in different industrial applications such as internal combustion engines. De Souza; De Vasconcelos Salvo; De Moro Martins (2012) studied the behavior of gas-particle multiphase flow using a Large Eddy Simulation (LES) to analyze two small sampling cyclone separators. Arrizubieta *et al.* (2014) and Ferreira *et al.* (2018) performed a nozzle design procedure using CFD tools to improve the gas-particle flow inside a Laser-Based Metal Deposition (LBMD) deposition nozzle. The new generation of these metallic deposition machines is being enormously improved using tools like CFD.

Ferreira *et al.* (2020) developed multiple experimental techniques such as optical and weighting material experiments and proposed a 2D axisymmetric CFD model to study three different nozzle designs obtaining good agreement with the material experiment results. It is shown in Figure 1.5 the model velocity results. Sebastian *et al.* (2021) proposed a 3D CFD model to study the gas glow behavior in a coaxial nozzle applied for a DED process. The gas flow setup was based on the previous experience of the manufacturer, and the CFD model helped to improve the machine configuration. The computational results obtained by the author are observed in Figure 1.6. This current work used the model proposed by Sebastian *et al.* (2021) to develop a 2D axisymmetric model for gas flow. In sequence, this model served as an input for a multiphase 2D model, simulating different configurations for the gas fluid flow. Developing a 2D multiphase model reduces the time to obtain the gas-particle flow behavior and can also help researchers and industry engineers to understand fast and better the DED machine nozzle functioning.

Figure 1.5 - Particle velocities for the three nozzles studied. Nozzle A presents a powder stream diverging from the central point. This effect is reduced by analyzing Nozzle B and almost avoided by considering Nozzle C which contains the most centralized powder.

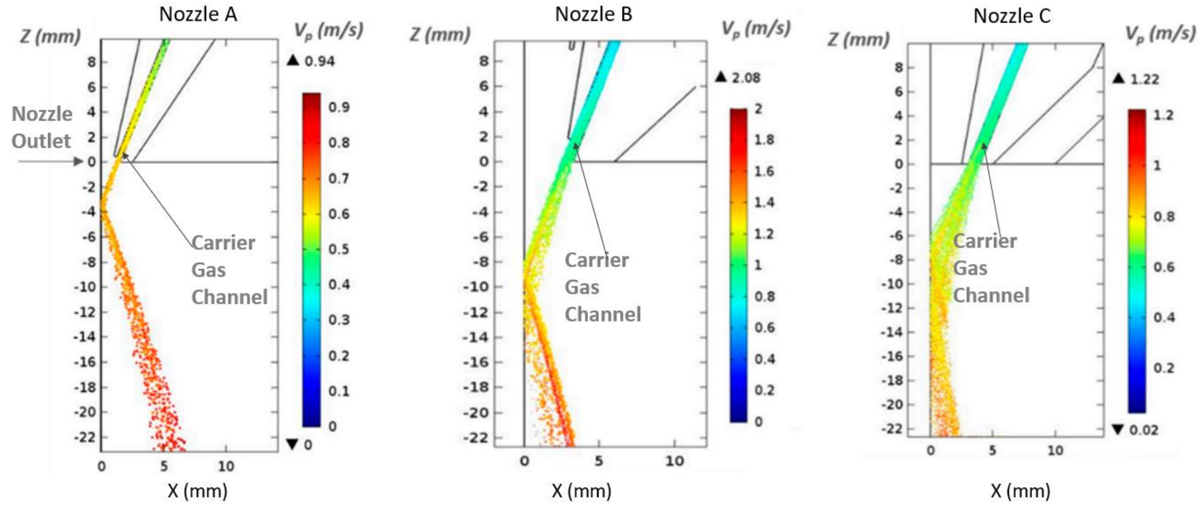

Source: adapted from Ferreira *et al.*, 2020.

Figure 1.6 - Velocity isovalues for the tested nozzle, considering the three channels used in the configuration.

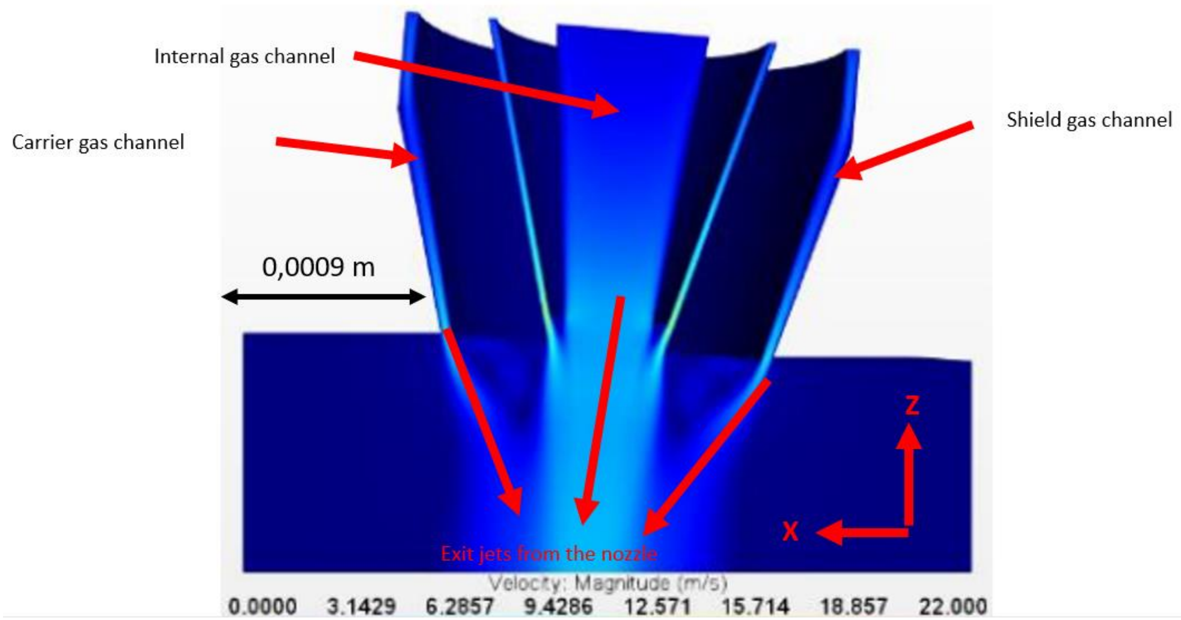

Source: adapted from Sebastian *et al.*, 2021.

For the work developed, there are some hypotheses to be tested using the proposed model:

1) The increase in the St will increase the C?
2) The reduction in the Re will increase the C?

One crucial point is ensuring the model is accurate enough to perform the hypothesis evaluation. This task is for now performed, ensuring that the simulation's physics is befitting the usual real cases. For full validation, a material experiment should be performed. The idea behind hypotheses 2 and 3 is based on the Re and St definition. Increasing the Re is supposed that the particles will have more influence coming from the fluid flow and then will deviate more, decreasing the Concentration on the desired deposition point. In the opposite way, the increase in the Stokes Number will make the particles less influenced by the fluid flow with less deviation, bringing more of them to the desired deposition point.

CHAPTER II

BIBLIOGRAPHIC RESEARCH

This chapter contains all the bibliographic research performed, including the Additive Manufacturing review, including the use of CFD for process parameters studies and nozzle design. It is presented the Fluid Mechanics review as well, including the main mathematical calculation and models and the description of the multiphase and discrete model. Finally the computational model is briefly discussed and presented.

2.1 Additive Manufacturing

In this section is presented the bibliographic research collected for the additive manufacturing process, including the nozzle design and process parameters assisted by CFD.

2.1.1. Review Articles

Kranz, Herzog and Emmelmann (2015) performed an experimental investigation verifying the influence of part position and orientation on accuracy and surface quality. Despite the potential of laser additive manufacturing processes, most design engineers face problems when developing a manufacturing plan using this technology. Studying the main influences of position and orientation, the authors came up with a guide, present in the paper, that can be used for this kind of application and other laser-based deposition technologies. Each structure presented has an excellent and unfavorable example, with underlying process restrictions and further recommendations.

Pinkerton (2015) studied the state of art related to LMD, including articles on the three stages of the application: the metallic powder and gas flow, the melt pool formation, and the clad track formation. Different approaches have been used over the last few years, but generally, the authors started to use more numerical approaches since the advance in computational processing capacity. However, the experiments can take advantage of this because they can use more sophisticated statistical models. The author highlights the functionality of the overall process model and the use of analytical processes to understand better the unknown related to the aspects of this manufacturing process. Still, many different research approaches have not yet been used and can be helpful in the industrial community.

Ngo *et al.* (2018) reviewed an extensive bibliography about the AM process, including all primary processes. The authors mention some works considering the DED technology description, advantages, and disadvantages. In addition, it describes this technology's economic and time benefits, presenting different analyses from multiple authors. As well, it shows microstructure and porosity problems analysis and the points concerning the influence of operation parameters on the deposited parts. The material waste and time reduction with profit increase using these new metallic AM technologies are similarly mentioned using different studies. An overview of metallic AM is given, and different articles were found to support this current research.

Camargo *et al.* (2020) systematically reviewed AM processes in three different applications: ceramic coating, AM of ceramics, and AM of composites with ceramic reinforcement. The authors presented the methodology used to classify the articles found. Thirty-one papers were selected for study, and for each article, information about raw material, substrate, process parameters, properties, and material sampling were collected. This methodology and the database presented can help future researchers and their work.

2.1.2. Atmosphere

Zhang and Coddet (2016) studied the effects of environmental pressure and nozzle geometry on particle concentration, distribution, and velocity in the LMD process. The LMD system with the coaxial powder nozzle is installed in a large-scale vacuum chamber to perform the tests, as shown in Figure 2.1.

Based on the previous experimental arrangement, a CFD 3D multiphase model was created to simulate different angle and outlet environment configurations. Figure 2.2 shows that a vacuum can lead to a more focused and concentrated powder flow. When using Helium instead of Argon as a carrier gas, the particle velocities increased considerably, from 261 m/s for Ar to 326 m/s for He.

Ruiz et al. (2018) studied the effect of a mixture of argon and helium on the LMD application, considering three different types of mixture for three different laser powers, considering a cross experiment design. They evaluated the results with two different types of experiment analysis, one evaluating the melt pool temperature and cooling time and the other characterizing the deposited layer based on some crucial geometrical factors. The increased helium concentration slightly reduces the clad height, as can be seen in Figure 2.3.

Figure 2.1 - The material experiment setup studied, for LMD process. The systems have a vacuum chamber used to perform the study of the effect of vacuum in the deposition process.

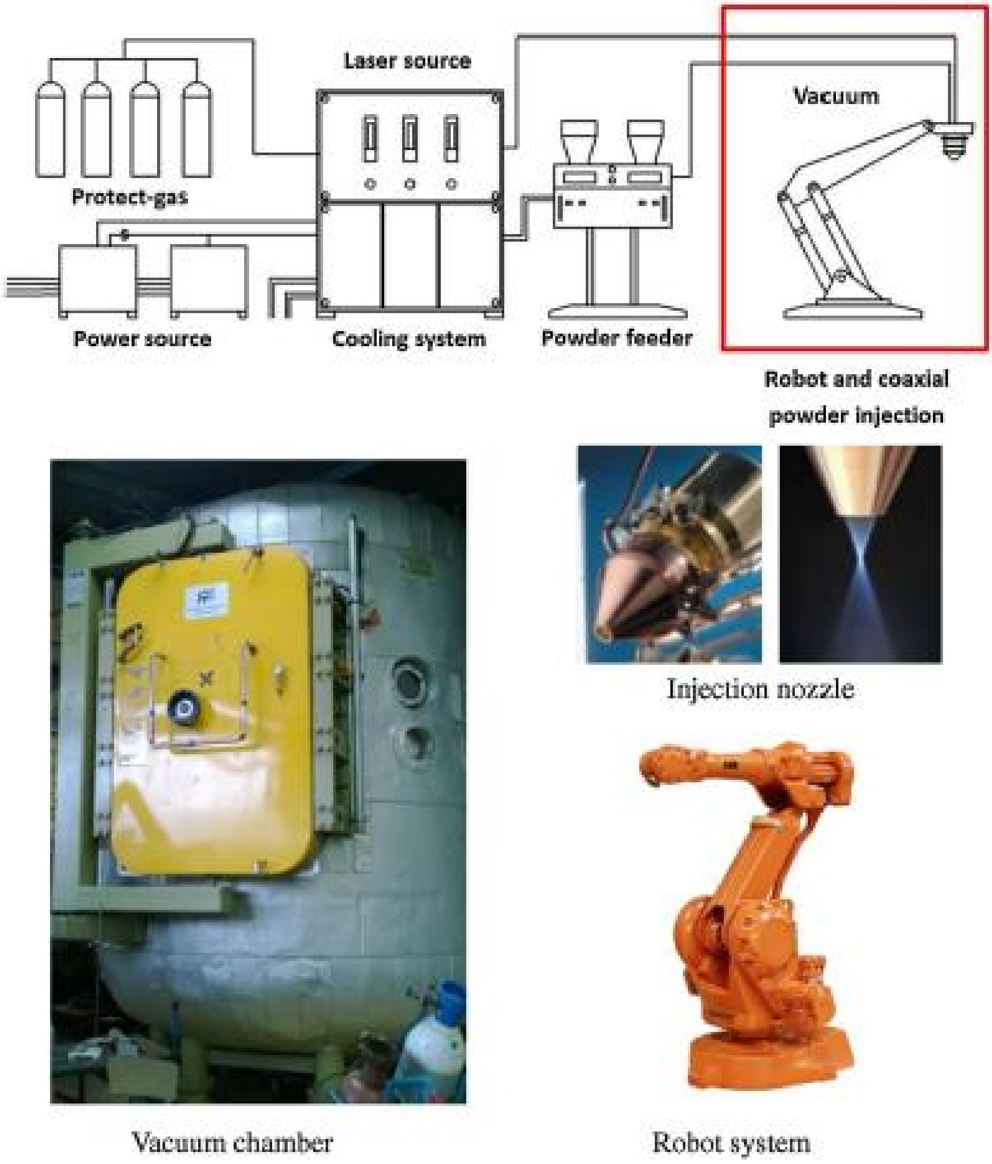

Source: adapted from Zhang and Coddet, 2016.

Figure 2.2 - Results obtained by the CFD model developed. It is possible to observe the increase in the particle concentration value when the vacuum is used.

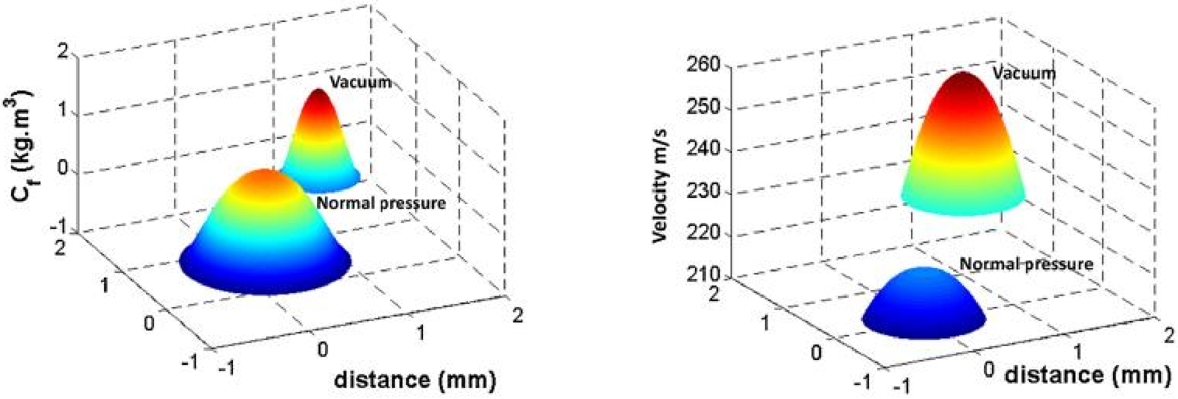

Source: adapted from Zhang and Coddet, 2016.

Figure 2.3 - Results obtained by the experiment developed. The increase in Helium concentration culminates in the clad height reduction.

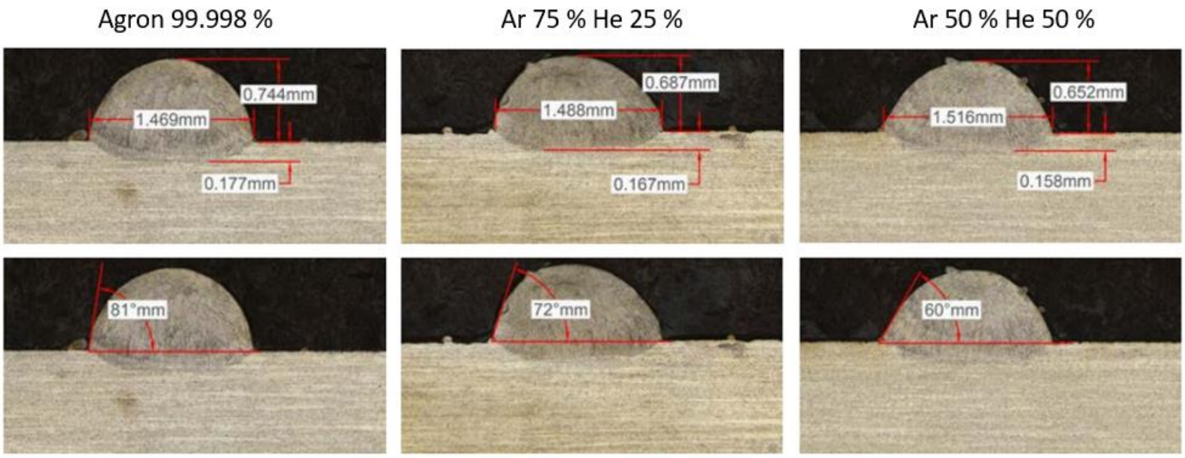

Source: adapted from Ruiz *et al*., 2018.

2.1.3. Laser Source

Lin (2000a) studied the effects of laser attenuation due to laser powder flux interaction below the nozzle and catchment efficiency during a 304 L stainless steel powder on mild steel with a 1 kW CO_2 coaxial LMD process, using two different configurations based on the Lin (2000b), applying two types of powder flux structures: focused (external nozzle) and columnar (inward nozzle). This is observed in Figure 2.4.

Figure 2.4 - Nozzle configurations used in the experiment.

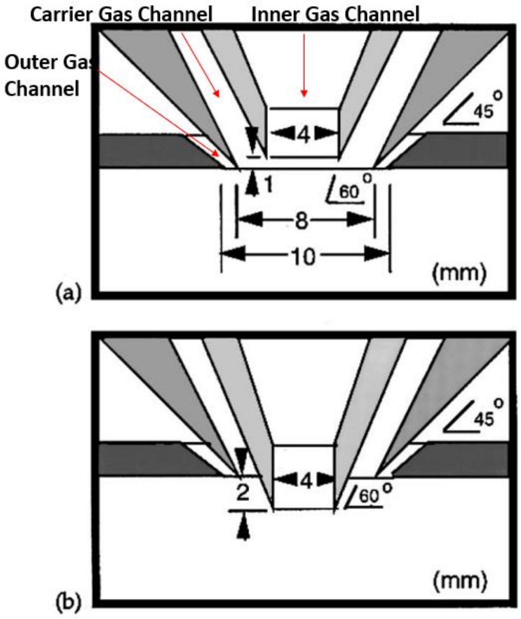

Source: adapted from Lin, 2000b.

Furthermore, it was verified that more than 50 % of the laser energy was attenuated by the powder stream in a focused stream using an outward position as noted in Figure 2.5. The catchment efficiency (η), measured by the weight ratio of the powder delivered to the powder deposited on the mild steel substrate during the LMD, is lower for the outward position, as it is possible to be observed in Figure 2.6.

Figure 2.5 - Laser attenuation results from the experiment developed, (a)initial stream width (w') equal to 3 mm (b) w' equal to 1 mm.

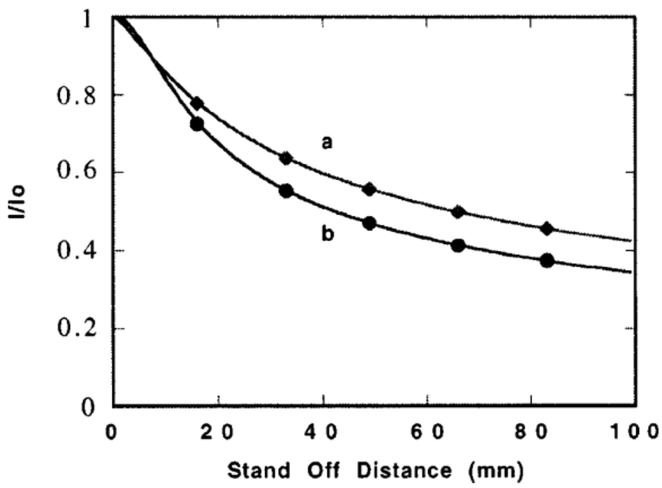

Source: Lin, 2000a.

Figure 2.6 - Catchment efficiency results from the experiment developed, (a) nozzle in the inward position and (b) nozzle in the outward position.

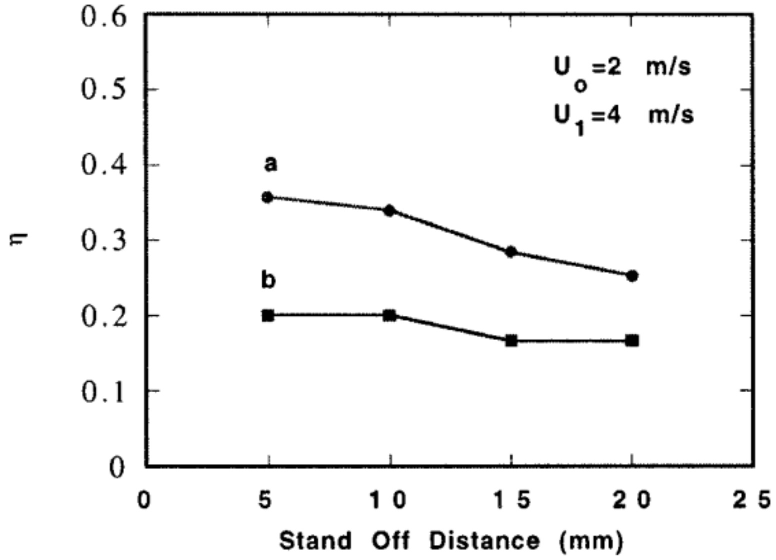

Source: Lin, 2000a.

Qi *et al.* (2006) studied the heat transfer and fluid flow in a coaxial LMD process applied to a laser metal deposition. It was created as a model to simulate the complex multiphysics phenomenon of deposition in a melt pool, including the laser beam and powder particle laser interaction and the behavior inside the melt pool. The model was compared with an experimental setup to be evaluated. It was verified with the model that by increasing the powder flow rate or the distance from the nozzle, the laser attenuation increases as well. The final solidified track is dependent on the laser power. An increase in the laser power produced a less smooth track despite the good metallurgical properties. The model and the experiment results confirmed a discrepancy of 22 % on molten pool geometry.

2.1.4. Nozzles

Crow *et al.* (1982) created a review work focused on the modeling definition for dilute-gas-particle flow. The work reviewed non-dimensional parameters, like volume fraction of the particle and gaseous phases, bulk density of particle and gas, and Stokes Number. Finally, the author discusses different models for one-dimensional and two-dimensional flows.

Lin (2000) studied the effects of nozzle arrangement and flow settings over the powder flow structure used for a LMD system using a numerical model in FLUENT®. His work showed an increase of more than 50 % in powder concentration using the outward nozzle arrangement compared with the inward nozzle arrangement. Additionally, this study verified that increasing the velocity will bring the focus close to the nozzle exit, but it will reduce the powder concentration.

Arrizubieta *et al.* (2014) present a new design methodology for a coaxial nozzle for the LMD process based on a CFD model. This study identified two major concerns related to using a rectangular entrance for the carrier gas and the flow pattern at the nozzle exit if a non-grooved internal cone is used inside the internal cone. For the first problem, a solution was proposed to put a chamfer on the entrance, better guiding the powder flow, as it is possible to be verified in Figure 2.7.

For the second one, it was added some grooves to the nozzle, reducing the tangential component of the force over the particles, as shown in Figure 2.8. Besides that, a thermal investigation was conducted to evaluate any overheating due to the laser interaction. It was verified that the nozzle heating could not be neglected, and a cooling channel was designed and simulated in different conditions. When using water flow between 1,0 L/min and 1,4 L/min, the nozzle temperatures were below 50 ◦C, ensuring the nozzle's integrity. Lately, the deposition angle was likewise inspected, considering the flow pattern at the nozzle exit, with the configuration shown in Figure 2.9. As it is possible to be analyzed in Figure 2.10, high inclination values lead to a reduction in powder concentration flux.

Figure 2.7 - Distribution of the powder in the XZ section, (a) before the chamfer (b) after the chamfer.

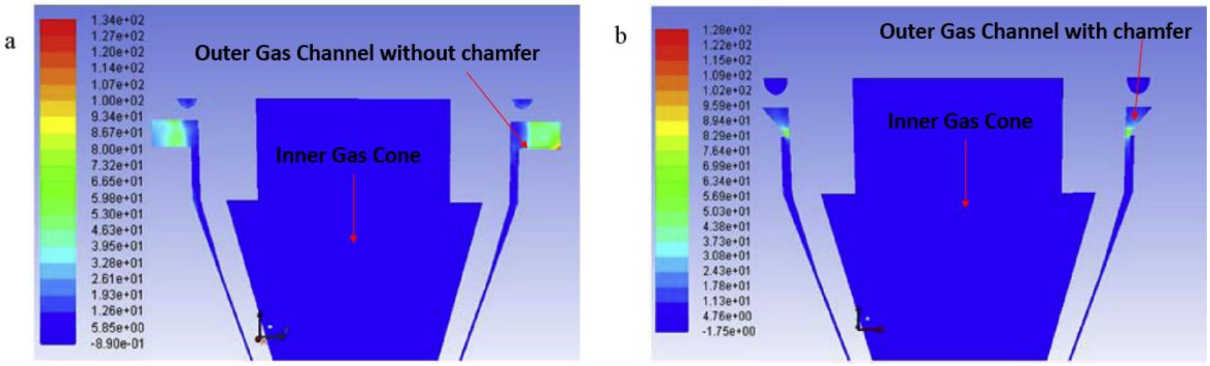

Source: adapted from Arrizubieta *et al.*, 2014.

Figure 2.8 - Effects caused by the application of internal grooves (a) distribution of the powder in an isometric view, (b) powder particle paths.

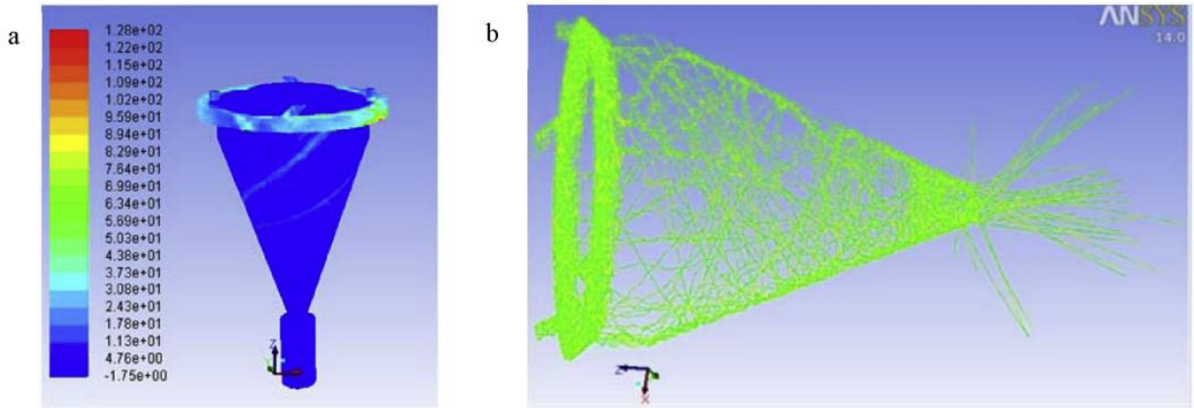

Source: adapted from Arrizubieta *et al.*, 2014.

Figure 2.9 - Different positions and inclinations of the nozzle analyzed for DED process.

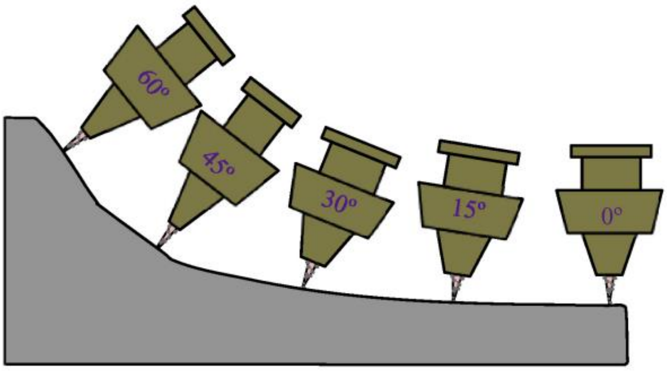

Source: adapted from Arrizubieta *et al.*, 2014.

Figure 2.10 - Powder flux paths colored by residence time and powder concentration flux, (a) for a 0◦ angle and (b) for a 45◦ angle .

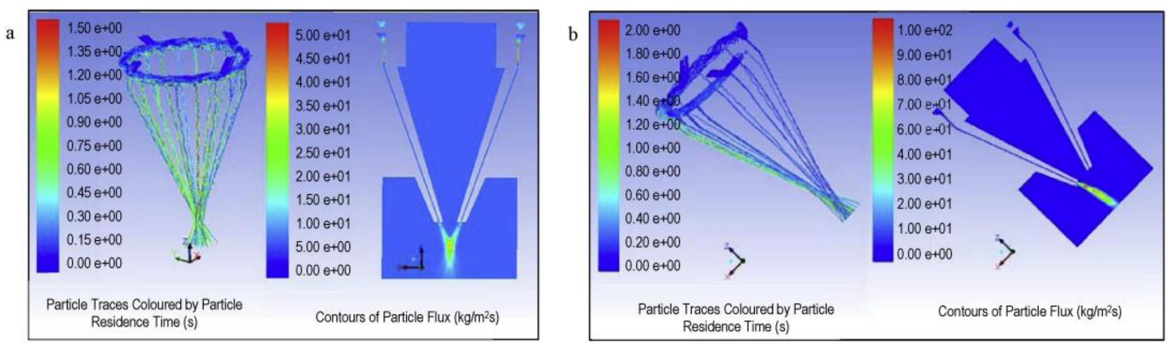

Source: adapted from Arrizubieta *et al.*, 2014.

Elise *et al.* (2018) created a CFD model to study the influence of inlet gas velocity and nozzle geometry on the flow shape at the nozzle exit, both essential factors in the efficiency analysis. In addition, an experimental investigation was executed. The CFD simulation was performed considering an inert atmosphere and after considering air. The results were compared with an experimental design developed. Three different designs were studied, and it was verified that the CFD simulation overestimated the experimental analysis with a 1,1 to 2,6 correlation factor for all results. This difference was related to a wrong calibration of the Pitot tube. Moreover, it was observed that an external atmosphere does not need to be considered since the vortex appeared much lower than the usual working distance and, in this case, should not impact the velocity field.

Two types of different nozzles, a three-jet, and a coaxial powder feeding nozzle, used in LMD applications were tested by Zhong *et al.* (2017). Since the geometry of the nozzles mainly defines the powder stream, computational and material experiments were performed. It was taken from the material experiment, the laser intensity distribution (LID), and the powder intensity distribution (PID), and these profiles were used in the simulation. It was noted then the powder stream effects on the track were deposited. The main result verified was that the three-jet nozzle had a high rate of particles hitting the substrate but a low catchment efficiency, which was not seen in the coaxial nozzle. The authors proposed that this phenomenon occurred due to the different particle velocities, more significantly with the use of the coaxial nozzle. Furthermore, the track cross-sectional analyses verified that for the coaxial nozzle use, the track microstructure was more homogeneous, mainly because of the more extensive penetration obtained from this type of nozzle. This result is seen in Figure 2.11.

Figure 2.11 - Metallographic prepared cross-sections of a track processed with (a) three-jet nozzle and (b) coaxial nozzle.

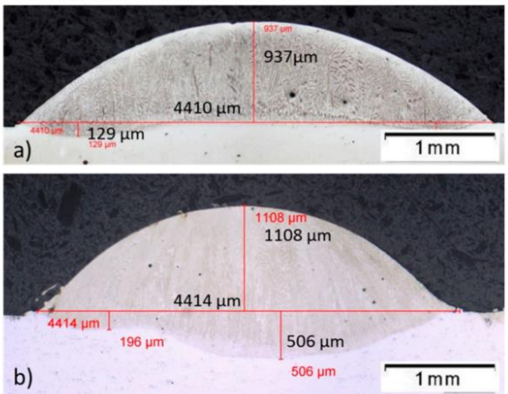

Source: Zhong *et al.*, 2017.

2.1.5. Process Parameters

Vetter *et al.* (1994) investigated different deposition parameters in the LMD process, considering an experimental approach. A coaxial nozzle was evaluated with different geometry parameters, including deposition angle and their influence over the aspects of pressure and velocity, both critics of laser cladding systems. It was shown that using a coaxial distribution of the laser beam and powder-gas mixture improves the energy distribution over the incoming powder. It was similarly proposed that a well-controlled gas velocity and shape are essential for the quality of the process.

Lin and Steen (1998) studied the influence of a coaxial nozzle design on the LMD process. Their work was one of the first to study coaxial nozzles, using a 2D model in FLUENT. A catchment efficiency study was performed, considering that a ricochet effect should be present when the particles touch the melt pool. The results are presented in Figure 2.12. It was demonstrated in this study that this novel nozzle could improve the powder stream. The interaction between the laser beam and the powder concentration can be controlled by generating a free oxidation deposited surface. Besides, changing the jet's exit can bring an improvement in quality and increase process efficiency.

Lewis and Schlienger (2000) studied the aspects of practical considerations on direct metal deposition assisted by lasers, considering both Direct Light Fabrication (DLF) and Laser Engineered Net Shaping (LENS®). The metallic additive manufacturing process is spreading more and more around the industries, mainly because of the one-step work that this kind of technology allows. However, practical aspects like accuracy, surface finish, tensile properties, deposition microstructure, or even the deposition of alloys, dissimilar metals, composites, and functional grades should be considered. Usually, as presented in the study, for DLF or LENS®, process accuracy is ±0,2, presenting Ra = 10 μm. The tensile yield strength from parts obtained from both DLF and LENS® exceeded that of the conventional process. Due to the laser deposition characteristics, there is usually no need to post-treat the fabricated parts thermally, mainly because it is possible to obtain an excellent and homogeneous microstructure using the correct machine configuration. A great advantage presented by the authors is the possibility to combine the metallic components in different ways to create different alloys or even dissimilar materials or composites, variating the metal grades in different part locations based on different part location strength requirements.

Figure 2.12 - The effect of the stream angle on the catchment efficiency. It is possible to verify that reducing the stand-off distance the catchment efficiency is reduced as well.

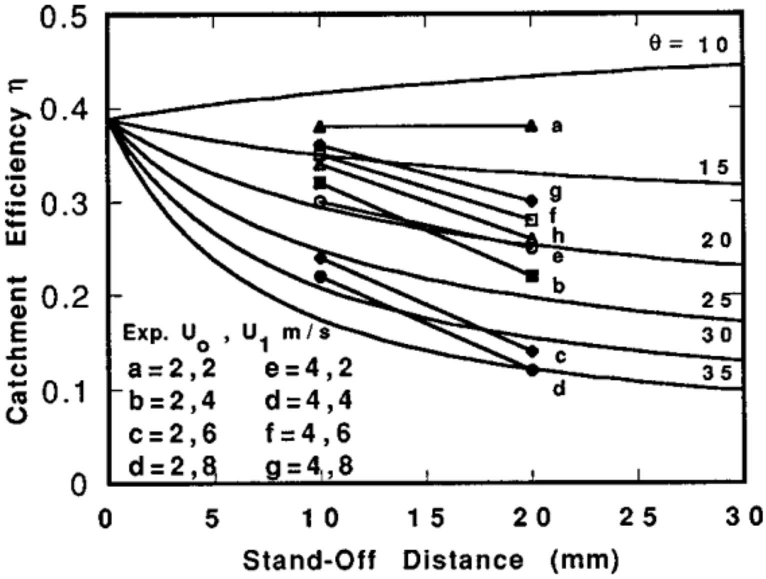

Source: Lin and Steen, 1998.

Pan and Liou (2004) realized a computational approach to simulate gas-particle flow for a coaxial nozzle design applied to the direct laser deposition process. They tested different parameters like deposition angle, nozzle outlet powder passage width, and the influence of the carrier gas. Although the work did not show essential points like experimental comparison or mesh characteristics, it still presents relevant coaxial nozzle design and optimization results. It is shown that changing the deposition angle to 45◦ generates the called focused stream structure with an abrupt increase in the powder concentration, as it is possible to be observed in Figures 2.13 and 2.14. Reducing the nozzle outlet powder passage width culminates in a slight increase in the concentration along the central axis. Furthermore, it was shown that the carrier gas could give a more narrowed powder stream, as it is shown in Figure 2.15.

The use of different angles can be necessary for specific deposition patterns and the optimization of these specific cases is an important factor to keep the process quality and efficiency. It is possible to observe in Figure 2.14 the concentration reduction with the increase in the deposition angle. This pattern indicates the efficiency reduction considering high angles. The use of a computational tool to study all these patterns is a faster way to perform important conclusions about the process and obtain important insights.

Figure 2.13 - Contours of concentration for (a) 45° and (b) 60°. It is possible to verify the increase in the number of particles/mm³ with a smaller angle, case (a).

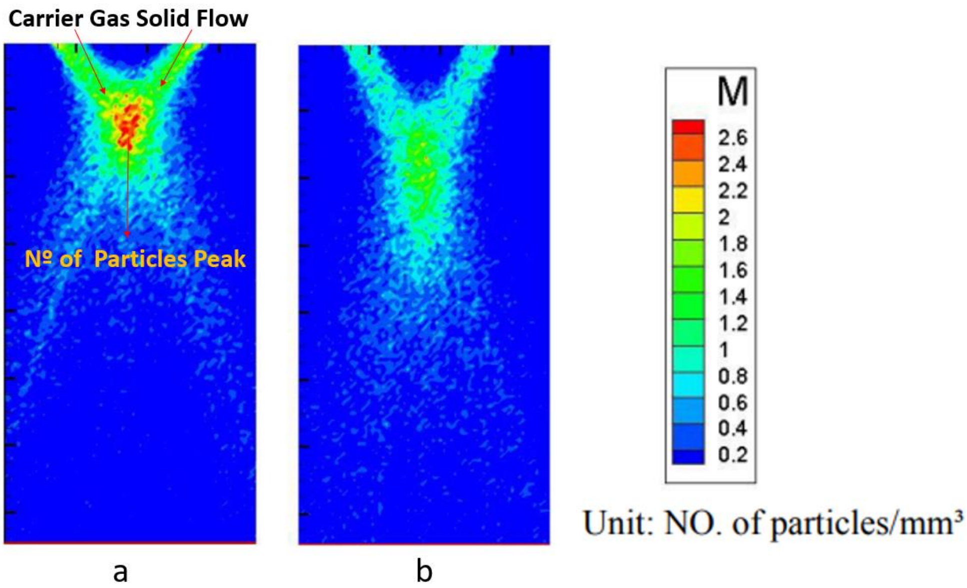

Source: adapted from Pan and Liou, 2004.

Figure 2.14 - Concentration variation in (a) axial and (b) radial directions for 45° and 60°.

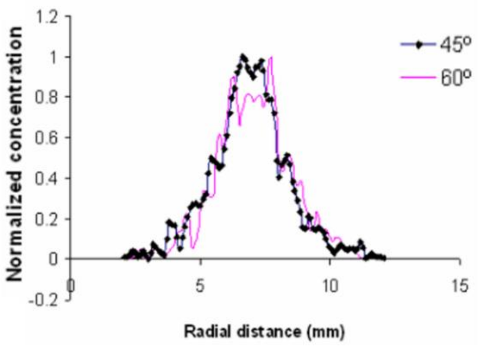

Source: Pan and Liou, 2004.

Figure 2.15 - Concentration variation in the axial and radial direction, considering different carrier gases.

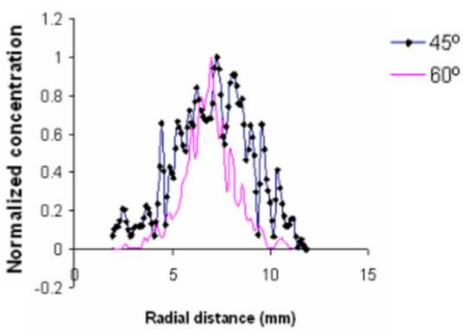

Source: Pan and Liou, 2004.

Pinkerton and Li (2004) constructed a mathematical model to predict powder concentration in powder flux based on the nozzle geometry. Additionally, they tried to predict the particle and laser interaction. The mathematical model created was in good agreement with the experiment, generating a design procedure that can be used to predict powder concentration before and after the merging point, as it is shown in Figure 2.16.

Figure 2.16 - (a) modeled powder concentration distributions and (b) images of the real powder flow from the material experiment.

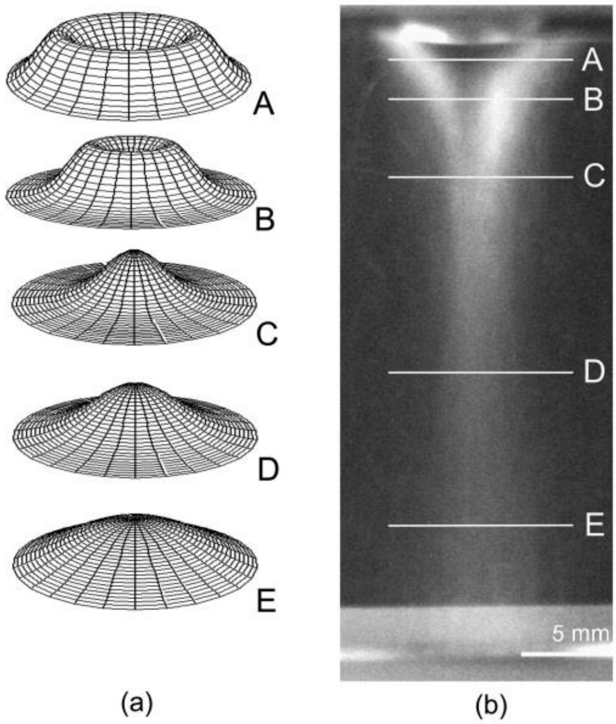

Source: Pinkerton and Li, 2004.

Zekovik *et al.* (2007) developed a 3D discrete phase model (DPM) to study parameter effects on the laser-based direct metal deposition process using four radially symmetrical nozzles. A FLUENT® model was designed, and a material experiment was conducted to evaluate the numerical model in a free flow condition, considering the beginning of the deposition event and deposition over a thin structure. Standoff distance influence was evaluated too. The model created agreed with the experimental investigation, verifying that using a secondary flow is essential to protect the process, mainly on flat surfaces, shown in Figure 2.17. In addition, it was presented that the spatter formation on the nozzle tips is mainly due to the ricochet of the powder particles reaching the nozzle tips, as it is possible to be confirmed in Figure 2.18.

Figure 2.17 - Path lines of the gas free flow for the studied case. It is possible to verify the convergence of the path lines to a central point near 4,75 mm bellow the nozzles exit.

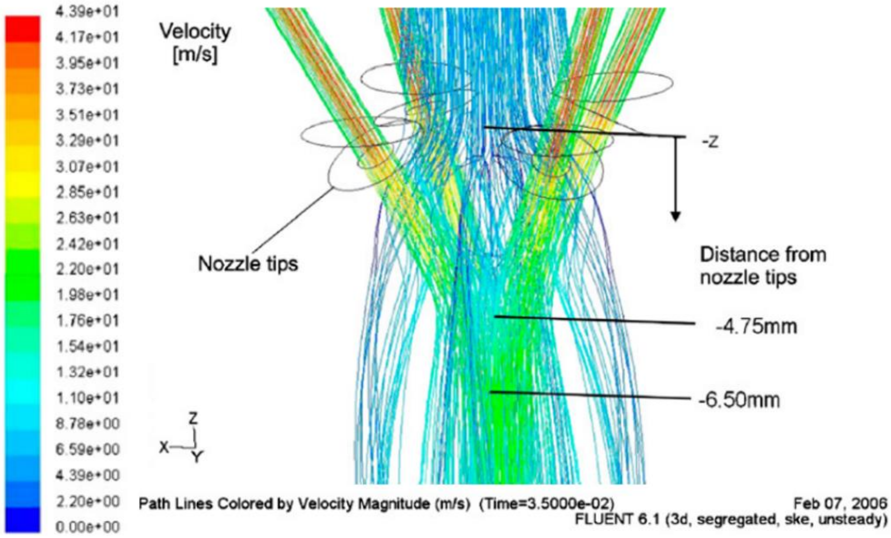

Source: Zekovik *et al.*, 2007.

Lee (2008) implemented a Taguchi experimental method (Design of Experiment, DOE) to evaluate the influence of some LMD parameters such as standoff distance, deposition angle, powder feed rate, scanning speed, shield gas type, laser pulse shape, and focal position. The experimental setup was performed using two radial coaxial nozzles, connected with an independent feeding mechanism with a pre-heating system and counting with image acquisition and processing structure to evaluate the spot regions done by the laser to assess the laser power arriving at the substrate. It is shown in Figure 2.19 the complete setup used for this experiment.

Figure 2.18 - Vertical cross-section of powder cloud below the analyzed nozzles, including (a) digital image, (b) concentration contours in the plane 100 μm offset from the plane of symmetry, and (c)concentration contours in the plane of symmetry.

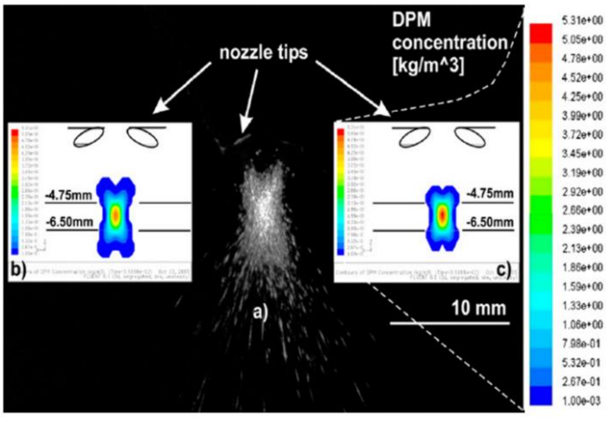

Source: Source: Zekovik *et al.*, 2007.

Figure 2.19 - Diagram showing the experiment setup and the LMD parameters used.

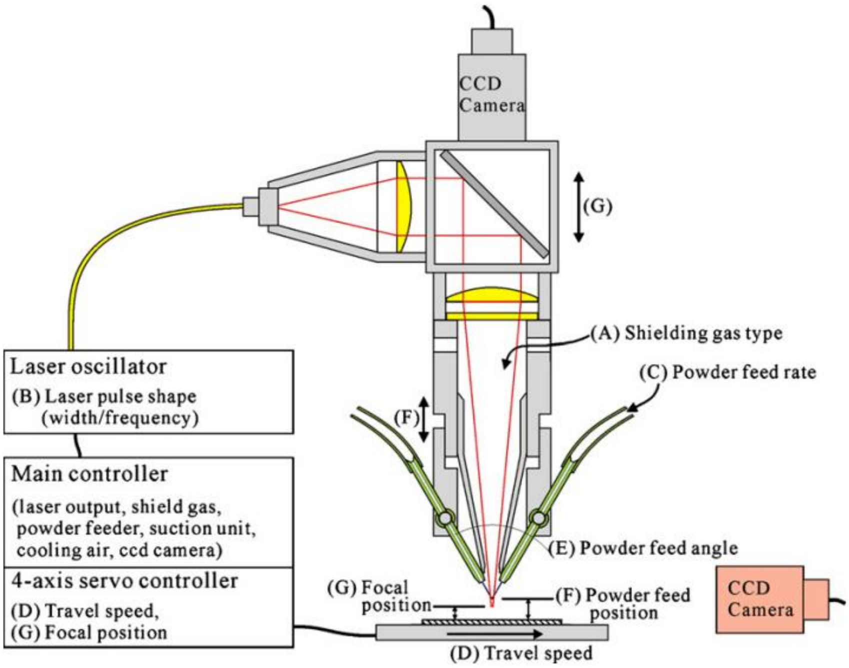

Source: Lee, 2008.

Based on the experiment results and statistical analysis, the more critical parameters verified were standoff distance, deposition angle, powder feed rate, and scanning speed. The less essential parameters were the shield gas type, the laser pulse shape, and the focal position. These results can be noted in the graphs present in Figure 2.20. The optimal configuration for the process was using zero mm as standoff distance with a deposition angle of 50°, powder feed rate of 0,62 g/s, and scanning velocity of 6,7 m/s.

Ibarra-Medina *et al.* (2011) created an integrated model to simulate the LMD process, from the nozzle powder-gas flow dynamics to the melt pool formation and behavior during the cladding operation. The model includes all the heat interactions and, in an advanced way, can generate a more reliable deposited layer. The simulation results were compared to an experiment, and good agreement was found. Comparing the profiles of track transversal cross section for the experimental and modeled, showing similar trends for height, although the model overestimated in 16 % the width.

A study by Zhu *et al.* (2011) considers the effects of the wall presence on the powder concentration peak and position. First, a computational model was built considering a free jet deposition and after with different size walls. Second, an experiment was performed in agreement with the computational procedure. It was found that the powder peak concentration decreases with the wall height and the powder peak position increases with the height, as it is possible to be inspected in Figure 2.21.

Figure 2.20 - Effects of the LMD parameters, including the negative impact in the deposition efficiency when the powder feed angle, the powder feed position, the travel speed and the laser pulse shape are increased.

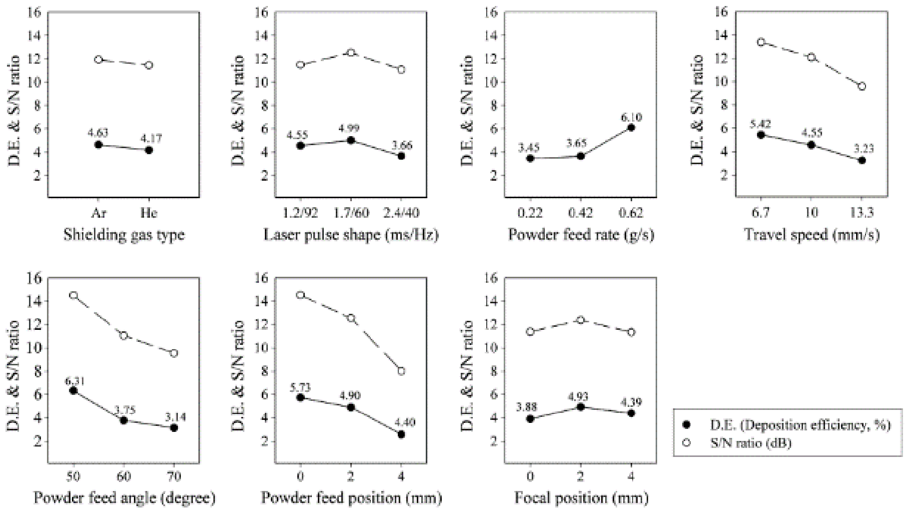

Source: Lee, 2008.

Figure 2.21 - Powder concentration distribution in (a) X direction and (b) Y direction. For the highest wall height, it is possible to verify the concentration peak reduction.

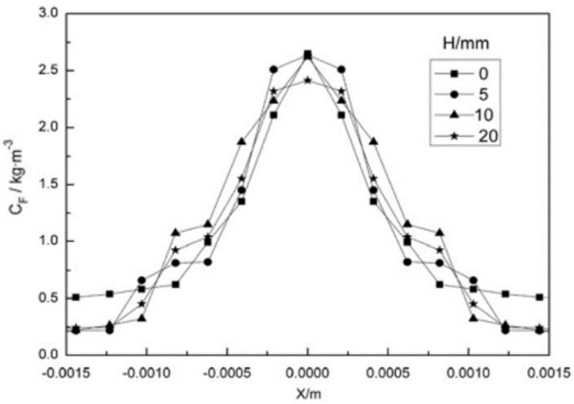

Source: Zhu *et al.*, 2011.

Balu, Leggett and Kovacevic (2012) proposed a computational model to study the effects of some essential parameters on the particle-gas flow structure for the laser-based powder deposition process applied for multi-material application. Process parameters, like carrier gas flow rate, powder mass flow, deposition angle, powder particle shape and diameter, substrate presence, and the restitution coefficient considering particles colliding with walls, were evaluated. It was found that an increase in the gas flow rate culminates in a reduction of powder particle concentration. Instead, the powder particle mass flow rate increases the powder concentration. The authors similarly variated the deposition angle, and it was found that an increase in the deposition angle leads to a more elliptical powder stream structure. This can increase the interaction time between particle and laser and brings a shadow effect on the substrate, reducing the melt pool quality. When a substrate was present, the ricocheting effect was observed in both experimental and computational models. Considering that different powder particles with different masses can be accelerated in different ways, evaluating the flow structure and checking the material distribution on the track built once multi-material is used is a concern. The computational model agrees with the experiment and can be used to model the powder flow structure.

Graf, Gumenyuk and Rethmeier (2012) a process for repair application considering the re-filling procedure for machined grooves. The study proposed V-shape and U-shape grooves considering two filling materials: stainless steel and titanium alloy. The U-shape groove presented the worst results for the stainless steel deposition due to accessibility problems, where the laser beam could not adjust perfectly on the groove walls. Stainless steel deposition inside the two different V-shape grooves demonstrated promising results, with deposition efficiency of 78 % and 75 %, respectively, for V-groove 1 and 2, as it is shown in Figure 2.22.

Figure 2.22 - V-shape and U-shape grooves results comparison for stainless steel. It is possible to verify that the U-shape produced the worst deposition result.

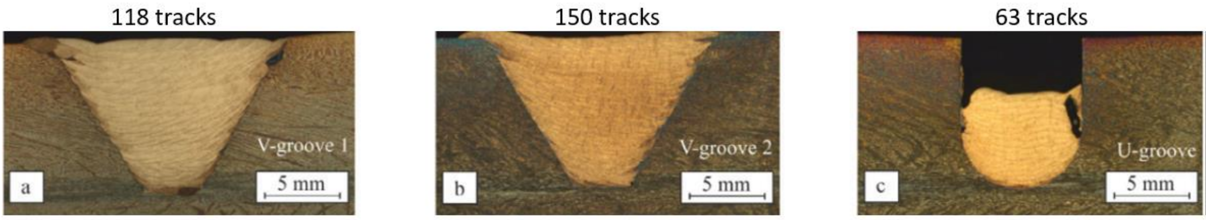

Source: Graf, Gummenyuk and Rethmeier, 2012.

One concern for the titanium alloy deposition was considering the cooling time that can affect the quality, considering that the titanium highly reacts with atmospheric gases. However, even with no additional inert gas protection, the tests conducted showed promising results in hardness and microstructure, with a powder deposition efficiency of 72 %. It is shown in Figure 2.23 the results for titanium.

Figure 2.23 - V-shape and U-shape grooves results comparison for titanium, again with V-groove presenting better qualitative results.

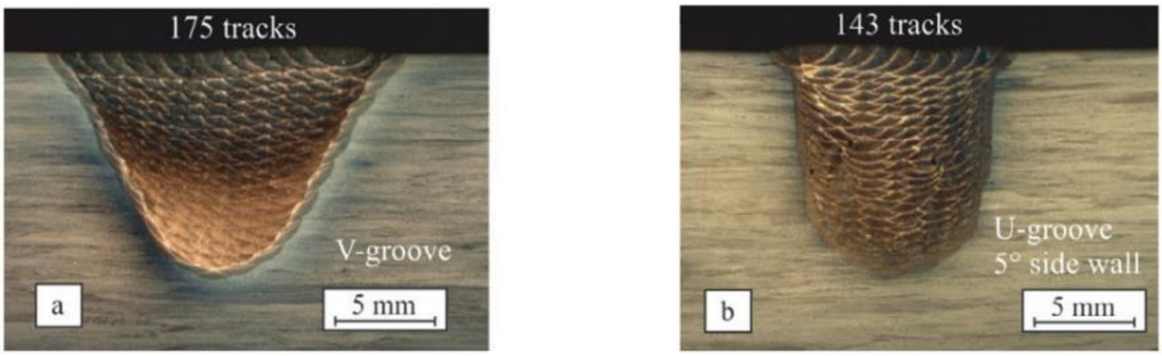

Source: Graf, Gummenyuk and Rethmeier, 2012.

Graf et al. (2013) designed a complete factorial experiment to study the influence of different parameters for LMD in maintenance, repair, and overhaul (MRO). Considering that different factors can influence the LMD, the authors proposed a cross-factor analysis to evaluate bead width using laser power (P), laser spot diameter (d), welding velocity (v), and powder mass flow (m) as variables and combining them in a randomized way. The results showed that bead width is most influenced by laser power, and bead height is most influenced by welding velocity and powder mass flow. An equation was developed using a linear factor combination, and good agreement was confirmed with the experimental results. The authors pointed out that the design of this experiment was limited because some constraints between the factors could not be included. These constraints can then be applied in practical computer design applications.

Ibarra Medina (2013) created an integrated numerical model that simulates different stages of the LMD process since the metallic powder flows up to the layer solidification in the melted pool, including heat transfer over the powder flux through the nozzle and after it. The model also connects powder flow to the metal track formation, creating an integrated model of all the primary LMD process moments. Different scenarios were included to investigate the interaction phenomenon present. An experimental setup consisting of the designed nozzle and a high-power diode laser LDL160-1500 assembled with an image acquisition system was developed to get the powder-flow image. A good agreement was observed between the experimental and the model, considering the merging zone. The differences found after the merging zone was mainly due to experimental techniques adopted. It was as well verified that the position of the substrate directly affects the mass concentration because the particles ricocheted from the substrate can be dragged inside the main powder flow. Another observation was about the assistive gas effects, where increasing the inner gas flow slightly increases the powder consolidation distance, and increasing the carrier flow reduces the consolidation distance, improving the focus and, consequently, the quality. The results are shown in Figure 2.24.

Figure 2.24 - Modelled powder stream (a) Front view, (b) perspective view and (c) transverse particle distribution. It is possible to observe the concentration peak at P2 as well as a sharper deposition pattern.

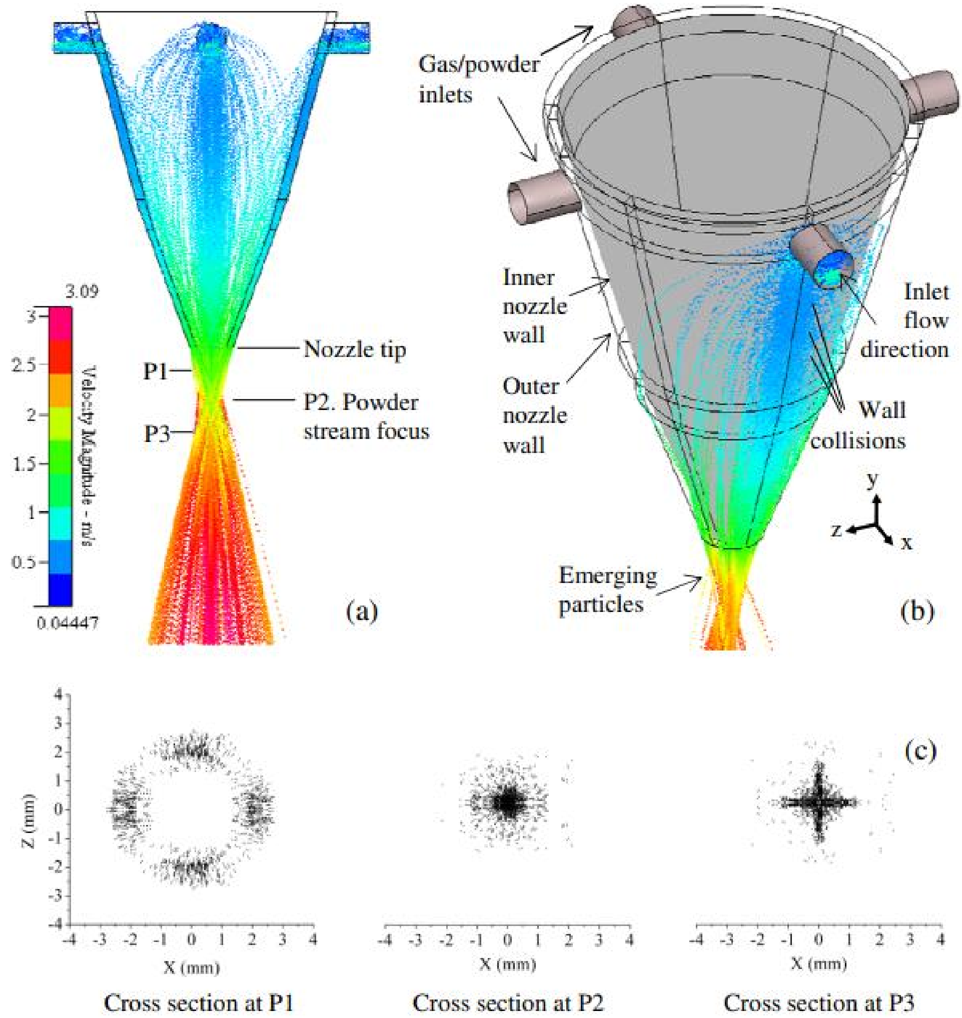

Source: Ibarra Medina, 2013.

Graf *et al.* (2015) studied both to obtain the best performance between good quality for complex parts prototyping using the SLM technique and fast production using the LMD technique. A process chain was developed and tested, and the results showed that the SLM part microstructure had higher porosity and smaller grain size than the LMD part microstructure. Combining both processes to produce different geometries on the same part can significantly reduce time, as shown by the study. The turbine manufactured by the SLM-LMD process combination showed that this procedure could be applied for small batch production to avoid heat-affected areas. In addition, it was found that a combination of different materials is allowed when using these techniques, considering that it is possible to adjust the material composition for a coating application using LMD, for example.

Zeng *et al.* (2016) overview AM technologies and focus on the Direct Energy deposition methods. The LMD method is presented and divided into three main parts: powder conveyance and dispersion, molten pool dynamics, and track formation. Numerical models can be constructed for all of them, and the authors developed an example of CFD. Model to evaluate the powder feeding system and behavior on the deposition formation. It was concluded with this simulation that if the powder particles reach higher velocities, they cannot be absorbed by the melted pool, generating another output, the rebounding velocity. The maximum velocity found in the simulation was 10 m/s.

Arrizubieta *et al.* (2017) designed a control system for the LMD process based on a solenoid valve to control the metallic particle flux fed to the process, expecting a reduction in material waste and geometrical errors. Two critical conditions were tested: the deposition beginning and the deposition over curves. An experimental setup was made to perform the tests, and a CFD model based on the previous work of Arrizubieta *et al.* (2014) was used. The regulation system is based on comparing the actual and theoretical velocity values. The results showed that the material accumulation at the deposition's beginning and the end were prevented. Where the direction change, the deposition over-height was reduced by 46 %.

Zeng *et al.* (2017) applied CFD simulation of the gas-powder flow as a modeling tool to test different geometries for the LMD. Nozzle design optimization. Four systems were modeled to give an insight into substrate standoff position and flow, based on the flow pattern at the nozzle exit, as flow shape, flow velocity, and powder concentration. Despite no experimental comparison, the results show the influence of critical parameters, like powder concentration and powder velocity, used to calculate process efficiency. The maximum particle velocity reached is around 40 m/s before the focus collision. The maximum powder concentration for the four nozzles was 0,0953 kg/m3 at the middle of the domain. It is proposed to use the model as a tool for heat transfer boundary conditions in a holistic Laser Metal Deposition model, considering radiation effects.

Chouhan *et al.* (2018) studied the behavior of a droplet falling over the substrate melt pool considering a Volume of Element (VOF) 2D flow model. The primarily driven forces of the flow inside the melt pool, Marangoni forces and Natural Convection forces, were evaluated using the ratio of Marangoni Number (Ma) and Grashof Number (Gr). As verified by the study, it is possible to conclude that the Marangoni Number is much more significant than the Gr, indicating that the fluid flow on the melt pool is mainly guided by the surface tension (Ma) rather than the buoyancy force (Gr).

Li *et al.* (2018) proposed a CFD-DEM (Discrete Element Model) to verify the relationship between the carrier gas (Argon) with a pre-mixed powder (Cu-Al) used in an LMD procedure to select effective parameters in pre-mixed powder applications. An experimental investigation was conducted, and the experiment and the CFD-DEM model presented good agreement.

Sebastian *et al.* (2021) developed a gas flow CFD model to evaluate a coaxial nozzle with three internal annular channels. An initial set of gas flow eas selected, based on previous experience of the manufacturer. The accuracy of the proposed model was verified by performing a material experiment, and the results were compared. The material experiment gas velocity measured 10 mm from the nozzle is presented in Figure 2.25.

Figure 2.25 - Gas flow velocity measured 10 mm below the nozzle in the material experiment

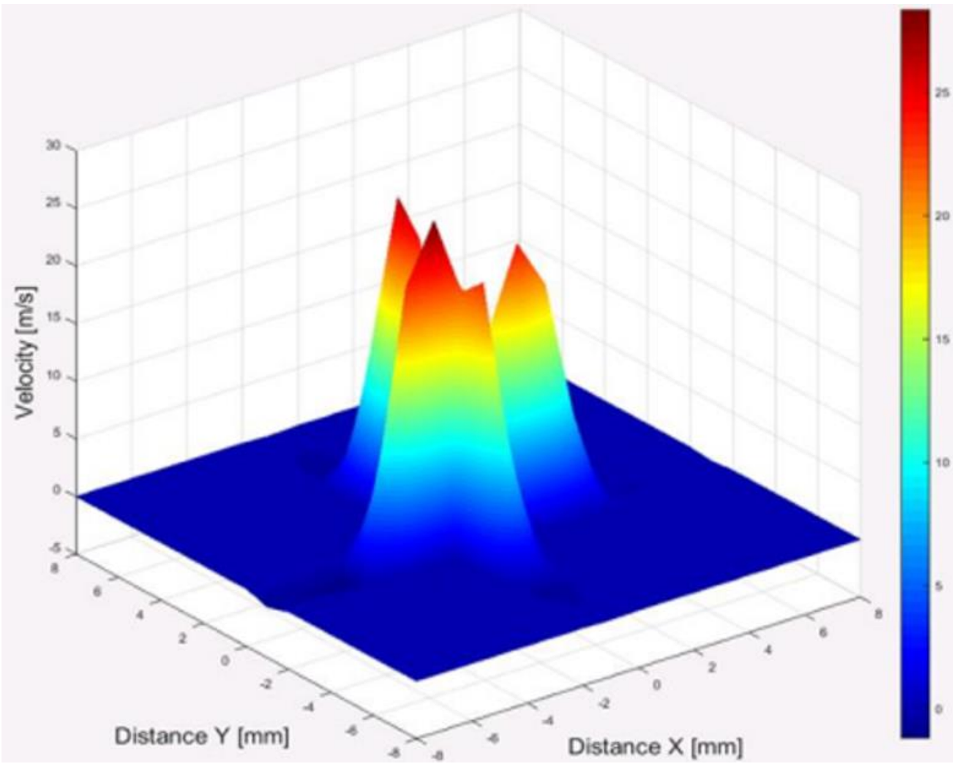

Source: Sebastian *et al.*, 2021.

2.1.6. Printed Parts Characterization

Koch and Mazumder (1993) studied the mechanical properties of the deposited parts and the deposition efficiency of an aluminum deposition system. They tested 1-D and 2-D deposition ways with a defined material deposition rate. Also, two different geometries were tested, a rectangular wall for planar vertical deposition testing, and a curved cylinder, for curved vertical deposition testing. A stress-strain test for axial and transverse specimens removed from the rectangular wall and a vessel pressure test were additionally performed.

As pointed by Koch and Mazumder (1993), the results showed that transverse specimens got a higher 0.2 % yield stress range, but the axial specimens showed higher ultimate tensile strength. The powder utilization analysis found that the weight increased to 10 g/min considering 90 % of powder utilization. Finally, it was concluded by the authors that support material is not necessary if the process is controlled in three or more dimensions.

Sexton *et al.* (2002) compared two deposition techniques, one using Tungsten Inert Gas (TIG) and another using a laser applied to powder flux. Both techniques can be applied to aerospace materials repair. To compare both, an experiment was conducted, and microstructure, hardness, cracking, porosity, and dilution levels were recorded for both processes, and it was concluded that the LMD presented clear advantages for the repair over the TIG process: low dilution, good fusion bonding and low porosity rate compared to the TIG process.

Bendeich *et al.* (2006) worked on a practical application of the LMD procedure applied to low-pressure (LP) stage turbine blade recovery. This application brings some problems, like residual stress from using an additive material of the base material, which can compromise the recovered material structure. It was proposed that a heat treatment relieve the tensions generated. An experimental procedure was performed (with two test procedures: x-ray diffraction (XRD) and neutron diffraction method analysis), and a simulation was designed to verify the effects of this temperature gradient over the region near the deposited layer, checking the positive effects of the heat treatment. The primary conclusion of the LP blade measurements was that the biggest tensile and compressive stresses are generated in the deposited layer and substrate metal. It was likewise possible to verify the positive effects of heat treatment on stress minimization and, therefore, the minimization of crack initiation probability.

Petrat *et al.* (2016) investigated different critical factors in the LMD process applied to turbine repair. Different deposition methods were investigated, and the final printed geometry influenced the nozzle position. They also performed a metallographic analysis to verify the internal porosity. It was verified and adjusted with different optimal configurations due to the study results, mainly considering the initial deposition point. Finally, the porosity was kept constant in all LMD printed parts, with no difference in power used.

2.2 Modeling Methodology

In this section is described the methodology used behind all the models used to simulate a multiphase flow representing the particle deposition in the additive manufacturing context. According to Silveira-Neto (2020), modeling is to represent physical phenomena, including a material physical model or a theoretical one. Once this model is built, it can be used for any process simulation. A mathematical model of this same problem can be staggered for a computational model that can be used to perform a computational simulation. Understanding all the steps until the construction of the physical model is a better way to understand and better design the solution for a defined problem.

2.2.1. Turbulence Modeling and Jets

The shear flows, like jets, have the emergence of instabilities due to the local strong velocity gradient and also due to the presence of surrounding noise and perturbations, as seen in Figure 2.26.

Figure 2.26 - Shear profile combination with surrounding perturbations.

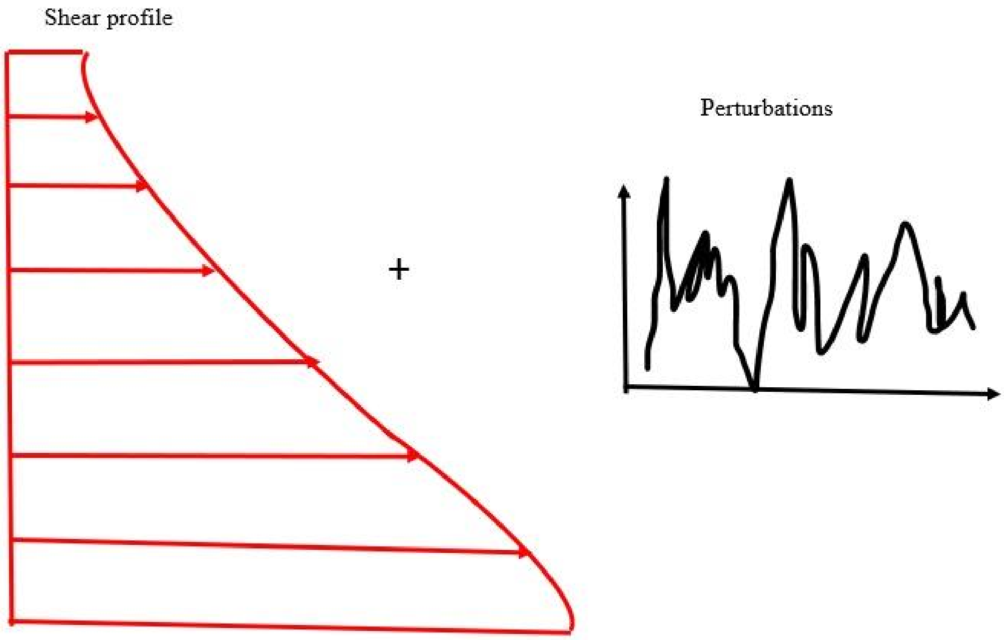

When the shear profile combines with local perturbation, this combination generates the appearance of coherent tridimensional structures, as shown by Moreira (2007). Turbulence can be classified as non-homogeneous and non-isotropic, homogeneous and non-isotropic, and, finally, homogeneous and isotropic. The classification is based on the statistical analysis of the flow and the Fourier analysis. The last one represents the transformation of the balance equations from physical space to Fourier Space, creating the π plane. This transforms the derivatives on products, making more accessible the flow turbulence analysis, allowing the representation of all non-linear interactions that happen simultaneously between all the eddy structures. It is presented in Figure 2.27 how this energy transference occurs.

Once the perturbations are injected inside the flow, they can be amplified in a specific frequency band given origin to the different known instabilities. One of these instabilities, The Kelvin-Helmholtz Instabilities, usually appears when two fluid flows are in contact and have different velocities. Silveira-Neto (2020) shows that these fluid flows are better known as free shear flows, where the fluid particles have a spatial variation in their velocity, which means regions with shear. A particular class of this flow type is the one inflectional shear with the average velocity field obeying the Rayleigh Theorem (RAYLEIGH, 1980) and Fjortoft Theorem (FJÖRTOFT, 1950). They can be divided into three fluid flows: mix layers flow, jets, and wakes.

Figure 2.27 - Energy transference between the different dynamics structures, occurring in a non-linear way. It is possibly to infer that the energy is captured by the biggest structures and it is finally transformed into thermal energy by the smallest structures or Kolmogorov structures.

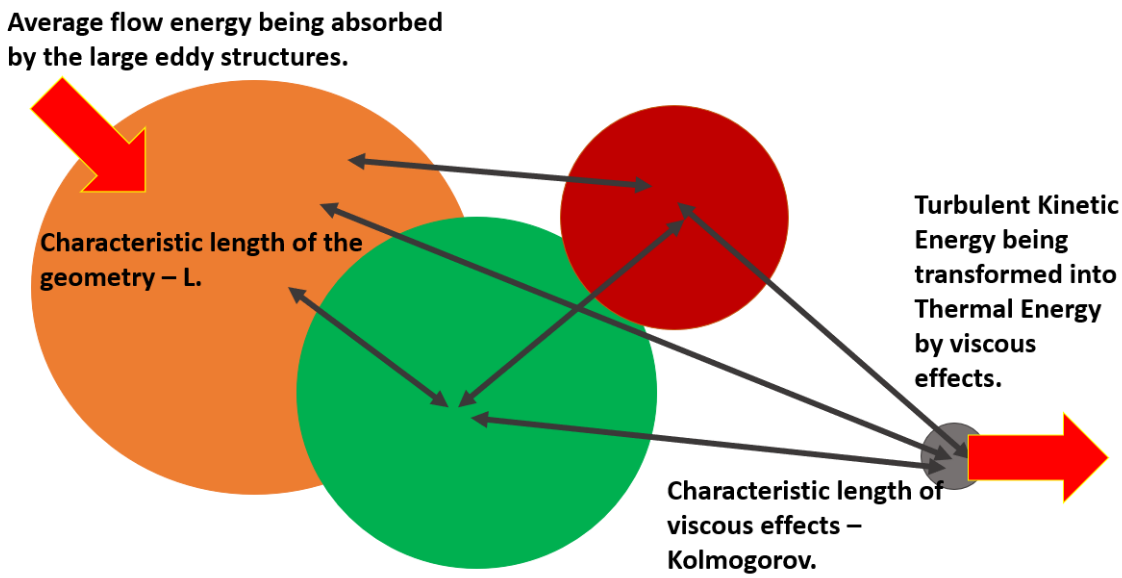

Explicitly talking about jets in spatial development, turbulence takes some specific characteristics. Jets can be classified as jets in temporal or spatial development. According to Silveira-Neto (2020), jets in spatial development result from a fluid flow injection with a given velocity inside a mean at rest or even with a different velocity, resulting in an inflectional profile of an average velocity.

The Kelvin-Helmholtz instabilities are then forced to pass through different velocities generating an unbalance (regions with high and low velocity) and then creating longitudinal structures that will culminate in complete tridimensional turbulence, affecting anybody or particle inside the fluid flow. The Kelvin-Helmholtz instabilities are present in spatial and temporal jets. Three examples of transition to turbulence present on jets are shown in Figure 2.28 (MOREIRA, 2007; GLAZE; FRANKEL, 2003). The adimensional import parameter usually used to evaluate if a flow is turbulent or not is the Reynolds Number (Re), which is described by Equation 1.

$$Re = \frac{\rho v_f D_h}{\nu} \quad (1)$$

As described by Silveira-Neto (2020), for jets, usually this number is low, and the transition initiates around Re_d = 10 (DRAZIN;REID, 1981).

Figure 2.28 - Smoke flow visualization and velocimetry of eddy pairs of particles using image.

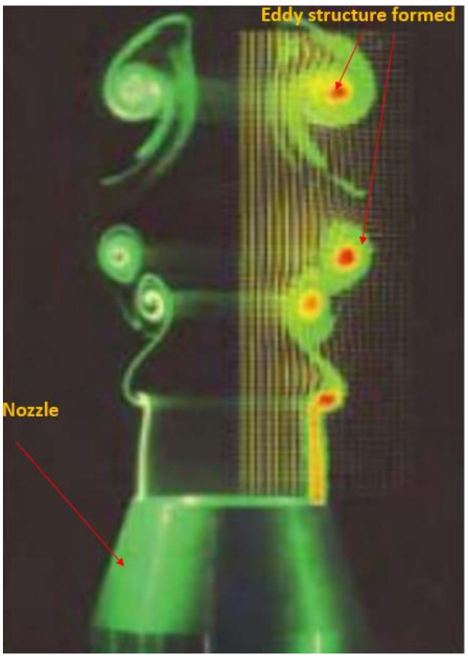

Source: adapted from Moreira, 2007.

2.2.2. Physical Model

Considering the additive manufacturing process, the central part of this type of machine is the nozzle. Then localizing the nozzle on the space, setting the coordinate system, the main variables, and hypothesis and constraints is the first step. The general scheme of the machine system is shown in Figure 2.29.

As it is possible to observe, the coordinate system is set on the table. The nozzle has a horizontal velocity, and the gas flows from the nozzle to the table surface. The flow pattern present in the system is a multiphase jet flow impinging over a flat surface. This definition is essential to elucidate which flow hypothesis will be used and which turbulence pattern will be present in the flow.

Figure 2.29 - Physical representation of the considered system.

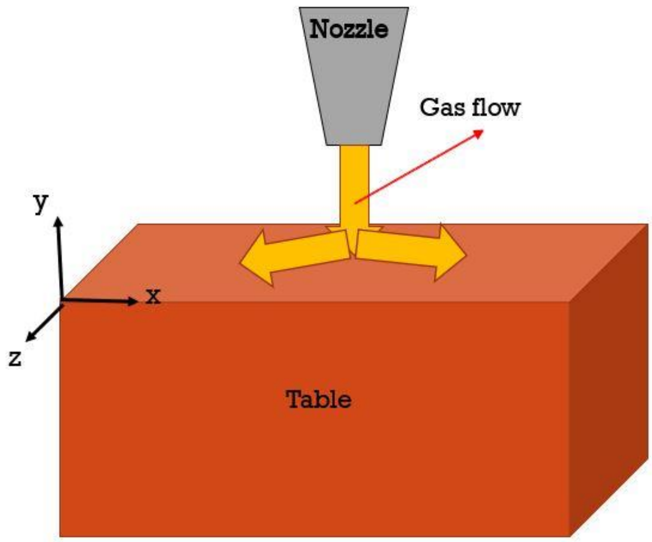

The hypothesis is to simplify the forward calculation. However, it is essential to validate if there is no crucial characteristic of the problem being missed with the simplification. The hypotheses adopted for this analysis are:

1) Incompressible gas flow.
2) The thermal effects as well as the laser interaction with the gas or with the particles. Then the energy equation will not be used.
3) The physical properties will be considered constant for the calculation.
4) The coordinate system will be considered fixed on the work table.
5) The horizontal work velocity will not be considered nor applied for this modeling procedure.

2.2.3. Differential Algebraic Mathematical Model

The following fluid flow equations are described in parts, considering all the required simplification hypotheses about the problem studied in the current research. The original equations were first obtained from the differential formulation of fluid flow described in Silveira-Neto (2020) and White (1979). Next is the formulation of the closure modeling, explaining the Reynolds Averaged Navier Stokes (RANS) Equations and modeling the turbulent viscosity using turbulence models.

2.2.3.1. Differential Algebraic Mathematical Model for an Observer Placed in the Interest Problem

According to Silveira-Neto (2020), in this case, the formulation will be applied for the velocity $\vec{V}$, seen by the non-inertial observer placed on the axis system (X,Y,Z) shown in Figure 3.4. The model that will be used for the analysis are presented in Equations 2 and 3.

$$\frac{\partial\rho}{\partial t} + \vec{\nabla}\rho\vec{V} = 0 \tag{2}$$

$$\rho\frac{D\vec{V}}{Dt} = \rho\vec{g} + \vec{\nabla}\overline{\overline{\sigma}}_{xyz} - \rho[\frac{D^2\vec{R}}{Dt^2} + \frac{D\vec{\Omega}}{Dt}\times\vec{r} + 2\vec{\Omega}\times\vec{V} + \vec{\Omega}\times(\vec{\Omega}\times\vec{r})] \tag{3}$$

It is described in Figure 2.30 how the fixed axis system can be linked with the inertial system, considered a far point inside the Universe. The table and the nozzle are immovable and do not rotate or translate. The gas flow exits the nozzle and impinges over the flat table surface. An order of magnitude analysis is then performed on Equation 3, and each term is analyzed to confirm which one is important for the current problem studied, as it presented in Equation 4.

$$\underset{1}{\rho\frac{D\vec{V}}{Dt}} = \underset{2}{\rho\vec{g}} + \underset{3}{\vec{\nabla}\overline{\overline{\sigma}}_{xyz}} - \rho[\underset{4}{\frac{D^2\vec{R}}{Dt^2}} + \underset{5}{\frac{D\vec{\Omega}}{Dt}\times\vec{r}} + \underset{6}{2\vec{\Omega}\times\vec{V}} + \underset{7}{\vec{\Omega}\times(\vec{\Omega}\times\vec{r})}] \tag{4}$$

Figure 2.30 - Positioning of the machine, considering the inertial system placed in a far point inside the Universe.

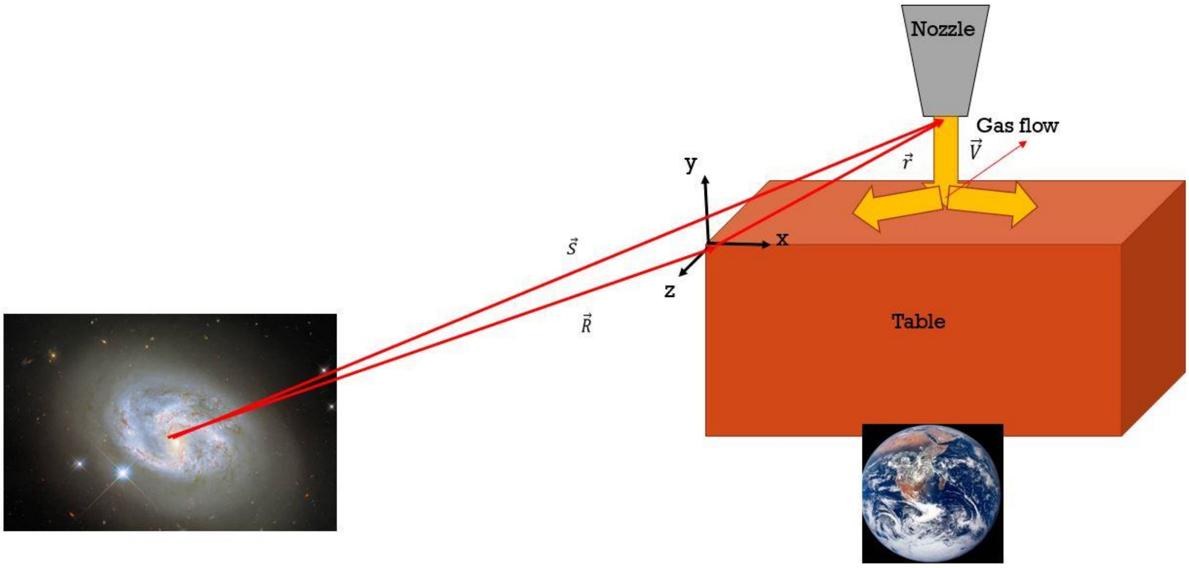

Source: adapted from Silveira-Neto, 2020.

1) Rate of change of linear momentum contained in the fluid particle / Advective net flow of linear momentum across the fluid particle surface: ~ 10^3 N/m³ .
2) Fluid particle weight: ~ 10^3 N/m³ .
3) Diffusive net flow of linear momentum: ~ 10^3 N/m³.
4) Absolute acceleration of deposition machine: ~ of the magnitude order of Earth acceleration, by Kantha and Clayson (2000) ~ 10^{-13}m/s² .
5) Euler acceleration or angular acceleration: ~ $\left\|\frac{D\vec{\Omega}}{Dt} \times \overrightarrow{R_T}\right\|$ ~ 10^{-15} rad/s²
6) Coriolis acceleration: $\|\vec{\Omega} \times \vec{V}\|$ ~ 0 rad/s. In this case, this term will be zero because the absolute angular velocity of the machine is zero.
7) Centripetal acceleration: $\|\vec{\Omega} \times (\vec{\Omega} \times \vec{r})\|$ ~ 0 m/s².

Then the final equation after the magnitude order analysis is presented in Equation 5. The boundary conditions and the initial conditions are presented in Equations 6 and 7 respectively.

$$\rho.\frac{D\vec{V}}{Dt} = \rho\vec{g} + \vec{\nabla}\overline{\overline{\sigma}}_{xyz} \quad (5)$$

$$\vec{V}(\vec{r}) = \begin{cases} \vec{0}, & se \quad \vec{r} \; = \; \vec{r}_T \\ -\vec{V}_{xyz}, & se \quad \vec{r} \; = \; \vec{r}_{P\infty} \end{cases} \tag{6}$$

$$\vec{V}(\vec{r},0) = \vec{V}_0 \tag{7}$$

The Equation 5 has a tensor to be closed, and Stokes proposed a way to close it for Newtonian fluids, based on the Equation 8. The mathematical differential model becomes the one presented in Equation 9 and 10.

$$\bar{\sigma}(\vec{r},t) = \mu(\vec{\nabla}\vec{V} + \vec{\nabla}\vec{V}^T) - \frac{2}{3}\mu(\vec{\nabla}.\vec{V}) \quad \bar{I} - p \quad \bar{I} \tag{8}$$

$$\frac{\partial\rho}{\partial t} + \vec{\nabla}\rho\vec{V} = 0 \tag{9}$$

$$\frac{\partial(\rho\vec{V})}{\partial t} + \vec{\nabla}(\rho\vec{V}\vec{V}) = -\vec{\nabla}p + p\vec{g} + \vec{\nabla}.[\mu(\vec{\nabla}\vec{V} + \vec{\nabla}\vec{V}^T) - \frac{2}{3}\mu(\vec{\nabla}.\vec{V})] \tag{10}$$

Considering the problem hypothesis described above and $\vec{\nabla}.\left(\vec{\nabla}\vec{V}\right) = \nabla^2\vec{V}$ the final mathematical differential formulation is described in Equation 11 and 12. The Einstein notation is presented in Equation 13.

$$\vec{\nabla}.\vec{V} = 0 \tag{11}$$

$$\frac{\partial(\vec{V})}{\partial t} + \vec{\nabla}.(\vec{V}\vec{V}) = -\frac{1}{\rho_0}\vec{\nabla}p + \vec{g} + \nu\nabla^2\vec{V} \tag{12}$$

$$\frac{\partial(\rho\vec{V})}{\partial t} + \vec{\nabla}(\rho\vec{V}\vec{V}) = -\vec{\nabla}p + p\vec{g} + \vec{\nabla}.[\mu(\vec{\nabla}\vec{V} + \vec{\nabla}\vec{V}^T) - \frac{2}{3}\mu(\vec{\nabla}.\vec{V})] \tag{13}$$

The next step is to take the averaged Navier Stokes equations (Boussinesq-Reynolds averaged equations). Once turbulence is present in the fluid flow, it is necessary to compute the time variation of these equations to compute the effect of fluctuations on the main flow. The procedure is firstly building the total velocity field as a sum of two parcels, one is the average velocity and the second one is the floating velocity, as it is shown in Equation 14 (SILVEIRA-

NETO, 2020). Replacing equation 13 with the equation 14 and making the necessary changes, it is possible to obtain the Equation 15.

$$u_i = \langle u_i \rangle + u_i{}' \tag{14}$$

$$\frac{\partial}{\partial x_j}(\langle u_i \rangle \langle u_j \rangle + \langle u'_i u'_j \rangle) = -\frac{1}{\rho_0}\frac{\partial \langle p \rangle}{\partial x_i} + \frac{\partial}{\partial x_j}[\nu(\frac{\partial \langle u_i \rangle}{\partial x_j} + \frac{\partial \langle u_j \rangle}{\partial x_i})] + \frac{\langle f_i \rangle}{\rho_0} \tag{15}$$

The term $\langle u'_i u'_j \rangle$ is known as Boussinesq-Reynolds Tensor and represents all the momentum changed between the averaged parcel and the floating parcel of the turbulent flow (SILVEIRA-NETO, 2020), that means, the representation of the non-linear process of transference of the turbulent-advective information. In the end, this term will represent a net flux of momentum changing between the eddy structures. This term is then transported to the left side of equation 13, resulting in Equation 16.

$$\frac{\partial}{\partial x_j}(\langle u_i \rangle \langle u_j \rangle) = -\frac{1}{\rho_0}\frac{\partial \langle p \rangle}{\partial x_i} + \frac{\partial}{\partial x_j}[\nu(\frac{\partial \langle u_i \rangle}{\partial x_j} + \frac{\partial \langle u_j \rangle}{\partial x_i} - \langle u'_i u'_j \rangle)] + \frac{\langle f_i \rangle}{\rho_0} \tag{16}$$

When placed together with the energy equation, this equation is called Averaged Boussinesq-Reynolds Equations or Reynolds Averaged Navier-Stokes Equations (RANS). These equations, together with the continuity equation, compose the model for the averaged behavior of a turbulent flow (SILVEIRA-NETO, 2020).

The averaged equations do not yet solve the transient behavior of the flows, which usually present fluid flow problems with great concern for engineering. Given an information of fluid, $\phi(\vec{x},t)$, obtained from the real fluid flow, for example obtained by a Direct Numerical Simulation (DNS), as proposed by Silveira-Neto (2020), it will be possible to verify the complete signal, $\phi(\vec{x},t)$, and the filtered signal $\bar{\phi}(\vec{x},t)$ in Equation 17.

$$\phi(\vec{x},t) = \bar{\phi}(\vec{x},t) + \phi'(\vec{x},t) \tag{17}$$

The difference between the complete signal and the filtered one gives the fluctuation of the information. The spectrum of the information $\phi(\vec{x},t)$ covers all the frequency band possible. This can be computationally costly to calculate, being possible to attest when running a DNS simulation. Usually, a cut frequency, fc, is used to separate the band of the bigger structure from the smaller ones. Then the bigger structures are modeled, and the smaller ones are calculated. This concept is the base for the Large Eddy Simulation (LES). For the Unsteady RANS (URANS), the period for the temporal filtering is taken as the total period of the flow sampling, which means all the structures are modeled. Usually, this last approach is common when just the averaged results are interesting for the specific problem analysis. The filtering procedure is first performed over the DNS base model, directly over the continuity equation, and over the momentum balance equation, it is possible to obtain Equations 18 and 19.

$$\frac{\partial \overline{u_j}}{\partial x_j} = 0 \tag{18}$$

$$\frac{\partial \overline{u_i}}{\partial t} = -\frac{\partial}{\partial x_j}\overline{u_i}.\overline{u_j} - \frac{1}{\rho}\frac{\partial \overline{p}}{\partial x_i} + \frac{\partial}{\partial x_j}[\nu(\frac{\partial \overline{u_i}}{\partial x_j} + \frac{\partial \overline{u_j}}{\partial x_i} - \tau_{ij})] + \frac{\overline{f_i}}{\rho_0} \tag{19}$$

Further analyzing Equations 18 and 19 (SILVEIRA-NETO, 2020), some important terms arise and need to be simplified or solved. The sub-grid Boussinesq-Reynolds tensor ($\overline{(u'_i u'_j)}$)and the crossed sub-grid tensor ($\left(\overline{\overline{u'_i}.u'_j}\right) + \left(\overline{u'_i.\overline{u'_j}}\right)$). These two statistical moments need to be modeled. Different approaches were proposed, and on this present work, it will be presented the Germano (1996) solution, where it is defined as the global sub-grid tensor as presented in Equation 20.

$$\tau_{ij} = \overline{\left(u_i u'_j\right)} - \overline{u'_i}.\overline{u'_j} \tag{20}$$

Applying Equation 20 above on the equation 3.19, it is possible to obtain the Navier-Stokes equations filtered, as it is shown in Equations 21 and 22.

$$\frac{\partial \overline{u_j}}{\partial x_j} = 0 \tag{21}$$

$$\frac{\partial \overline{u_i}}{\partial t} = -\frac{\partial}{\partial x_j}\overline{u_i}.\overline{u_j} - \frac{1}{\rho}\frac{\partial \overline{p}}{\partial x_i} + \frac{\partial}{\partial x_j}[\nu(\frac{\partial \overline{u_i}}{\partial x_j} + \frac{\partial \overline{u_j}}{\partial x_i} - \tau_{ij})] + \frac{\overline{f_i}}{\rho_0} \tag{22}$$

2.2.3.2. URANS Methodology, Turbulent Viscosity and SST-kω Closure Model

The URANS methodology, as described by Silveira-Neto (2020), is based on Equations 21 and 22. The main goal of this type of model is to simulate the low frequencies transient behavior of turbulent flows. Most of the non-linear interactions between large and small eddies (Kolmogorov time length and spatial length) are modeled, and the result is coupled with the low-frequency analysis. For this type of solution, there is no need for a highly refined model, and usually, the computational cost is not so high compared to an LES or DNS simulation. To solve Equation 21 and 22, one way proposed by Boussinesq (1897) is to close this opened problem and stagger this tensor in the function of the velocity field gradients (SILVEIRA-NETO, 2020) as it ispresented in Equation 23.

$$\tau_{ij} = f(\overline{u_i}, \overline{u_j}) \tag{23}$$

Based on the Stokes model for the viscous molecular stress, Boussinesq proposed the following closure model for the Boussinesq-Reynolds tensor, as it is presented in Equations 24 and 25.

$$-\tau_{ij} = \nu_t(\frac{\partial \overline{u_i}}{\partial x_j} + \frac{\partial \overline{u_j}}{\partial x_i}) - \frac{2}{3}k\delta_{ij} \tag{24}$$

$$k = \frac{1}{2}\tau_{ij} = \frac{1}{2}(\tau_{11} + \tau_{22} + \tau_{33}) \tag{25}$$

It is essential to verify that the turbulent kinematic viscosity is a flow property, not a fluid property, like molecular viscosity. The turbulent viscosity will depend on space and time also. Modeling the closure problem with the information from the Equations 24 and 25, it is possible to obtain the Equation 26.

$$\frac{\partial \overline{u_i}}{\partial t} = -\frac{\partial}{\partial x_j}\overline{u_i}.\overline{u_j} - \frac{1}{\rho_o}\frac{\partial \overline{p}}{\partial x_i} + \frac{\partial}{\partial x_j}[(\nu + \nu_t)(\frac{\partial \overline{u_i}}{\partial x_j} + \frac{\partial \overline{u_j}}{\partial x_i} - \tau_{ij}) - \frac{2}{3}k\delta_{ij}] \tag{26}$$

Where vef = (ν + ν_t). The closure problem is, then, to solve by algebraic equations or additional balance equations to calculate the turbulent viscosity and diffusivity or to, alternatively, close the filtered equations for turbulence. Multiple models depend directly or indirectly on turbulent viscosity. Models at zero equation (majority of sub-grid models, Prandtl Mix-Layer Hypothesis, PRANDTL, 1925), models at one equation (PRANDTL, 1945;

SPALLART;ALLMARAS, 1992; BARTH;BALDWIN, 1990). The two-equation models are also famous. Kolmogorov (1941) proposed the first two-equation model, based on the Turbulent Kinetic Energy (k) and based on the Kolmogorov Frequency (ω), also known as Specific Power of Viscous Transformation of Turbulent Kinetic Energy. Wilcox (1998) worked on Kolmogorov's (1941) model and adapted the model for low Reynolds numbers and near-wall regions. Prandtl and Kolmogorov also proposed a model based on the Turbulent Kinetic Energy (k) and Viscous Transformation Power of Turbulent Kinetic Energy (ϵ).

Another important model is the Shear Stress Tensor model, proposed by Menter (1994). This model aimed to overcome problems by applying the k- ϵ or the k-ω models, creating a hybrid format based on these two models. In summary, the k- ϵ usually needs better modeling of the dumping for the turbulent viscosity near the walls. The k-ω usually solves well near the wall but has problems solving regions with high sensitivity to free borders (SILVEIRA-NETO,2020; WILCOX, 1988; MENTER, 1994; DAVIDSON, 2014). Menter (1994) proposed the fusion of the models, taking advantage of both of them. A better explanation is found in Silveira-Neto (2020). The equations of this model can be verified in Equations 27, 28, 29 and 30.

$$\frac{\partial(\rho k)}{\partial t} + \frac{\partial(\rho u_j k)}{\partial x_j} = P - \beta^* \rho \omega k + \frac{\partial}{\partial x_j}[(\mu + \sigma_k \mu_t)\frac{\partial k}{\partial x_j}] \tag{27}$$

$$\frac{\partial(\rho \omega)}{\partial t} + \frac{\partial(\rho u_j \omega)}{\partial x_j} = \frac{\gamma}{\nu_t} P - \beta \rho \omega^2 + \frac{\partial}{\partial x_j}[(\mu + \sigma_\omega \mu_t)\frac{\partial \omega}{\partial x_j}] + 2(1 - F_1)\frac{\rho \sigma_{\omega 2}}{\omega}\frac{\partial k}{\partial x_j}\frac{\partial \omega}{\partial x_j} \tag{28}$$

$$\gamma_1 = \frac{\beta_1}{\beta^*} - \frac{\sigma_{\omega 2}\kappa^2}{\sqrt{\beta^*}} \tag{29}$$

$$\gamma_2 = \frac{\beta_2}{\beta^*} - \frac{\sigma_{\omega 2}\kappa^2}{\sqrt{\beta^*}} \tag{30}$$

With the coefficients being: σk1 = 0.85, σk2 = 1.0 " σω1 = 0.5, σω2 = 0.856, β1 = 0.075, β2 = 0.0828, β∗=0.09, κ = 0.41, and a1 = 0.31. For this reason, the SST-k-ω model was chosen to be the turbulence model used to simulate the deposition nozzle, considering the duplicity of the flow behavior at the beginning inside the nozzle walls and after a free shear flow (jet in spatial development).

2.2.4. Multiphase Modeling

According to Brennen (2005), multiphase flows can be defined as all fluid flows consisting of more than one phase or component. There is a giant spectrum of different fluid flows, considering the combination between liquids and solids, liquids and gases, gases and solids, or gases and particles. It is possible to divide the multiphase flows into two categories: disperse flows (usually containing particles, drops, or bubbles) and separated flows, usually two different fluids in two or more different streams separated by interfaces (BRENNEN, 2005). The complexity of multiphase flows requires a robust methodology to study their behavior. Usually, there are three different ways to develop different models to study them (BRENNEN, 2005): experimentally, with laboratory-sized equipment to perform a material experiment, theoretically, using the well-known mathematical equations e models and computationally, using the equations in a discretized way and the computer power to iterate over these equations and solve them with a given error. As pointed out by Brennen (2005), the predictive capability to understand the physical behavior of the multiphase flows heavily relies on the modeling and computational capacity.

According to Brennen (2005), multiphase flows can be defined as all fluid flows consisting of more than one phase or component. There is a giant spectrum of different fluid flows, considering the combination between liquids and solids, liquids and gases, gases and solids, or gases and particles. It is possible to divide the multiphase flows into two categories: disperse flows (usually containing particles, drops, or bubbles) and separated flows, usually two different fluids in two or more different streams separated by interfaces (BRENNEN, 2005). The complexity of multiphase flows requires a robust methodology to study their behavior. Usually, there are three different ways to develop different models to study them (BRENNEN, 2005): experimentally, with laboratory-sized equipment to perform a material experiment, theoretically, using the well-known mathematical equations e models and computationally, using the equations in a discretized way and the computer power to iterate over these equations and solve them with a given error. As pointed out by Brennen (2005), the predictive capability to understand the physical behavior of the multiphase flows heavily relies on the modeling and computational capacity.

The interactions between the phases should be another concerning point because it is the core of the fluid particle coupling. The way that the fluids and their turbulence interact with the particles and the way that the particles interact with the fluid and its turbulence and Other particles is crucial for correctly modeling the system. All these interactions are always present; however, they are more or less important according to the multiphase flow characteristics and should be considered. This relation between these two phases is better described by how dense or dilute the discrete phase is inside the continuous phase. Considering specifically a gas-particle system, when the system is dilute usually, the following characteristics are present:

1) High gas velocities;
2) Low solid concentration;
3) Low solid transfer rate;
4) Particle more individualized;

Considering the dense system, the following characteristics are present:

1) Low gas velocities;
2) High solid concentration;
3) High solid transfer rate;
4) Particle beavering as clouds (particle agglomeration inside the fluid flow);

Based on these two descriptions, the phase coupling can be divided as shown :

a. **One-way coupling**: the fluid phase influences the particulate phase through the aerodynamic drag and turbulence, but the particulate phase does not influence the fluid phase.
b. **Two-way coupling**: the fluid phase influences the particulate phase through the aerodynamic drag and turbulence, and the particulate phase reduces mean momentum and turbulence kinetic energy in the fluid phase.
c. **Four-way coupling**: this type of coupling includes all two-way coupling behaviors and the particle-particle collision, accounting for particle pressure and viscous effects.

Based on these classifications, Elghobashi (1994) proposed a classification map to verify where the multiphasic flow is placed, according to the volume fraction and the relation between τp is the particle response time and the τ_e the turnover time of large eddy ($\frac{\tau_p}{\tau_e}$). The diagram is shown in Figure 2.31.

The interaction with turbulence usually is in two main points (GORE; CROWE, 1989; BRENNEN, 2005): (1) the transference of turbulence behavior from the fluid to the particles generates complex unsteady motions of the particles and then results in a non-uniform spatial distribution of them or even particle segregation and (2) the transference from the particles to the fluid turbulence. This can be well seen in Figure 2.32, which shows the influence of the particle diameter on the energy transference from the particle to the flow (two-way coupling characteristic).

Figure 2.31 – It is presented the Elghobashi map, which contains each coupling scheme for a specific combination of a given volume fraction and ($\frac{\tau_p}{\tau_e}$) relation.

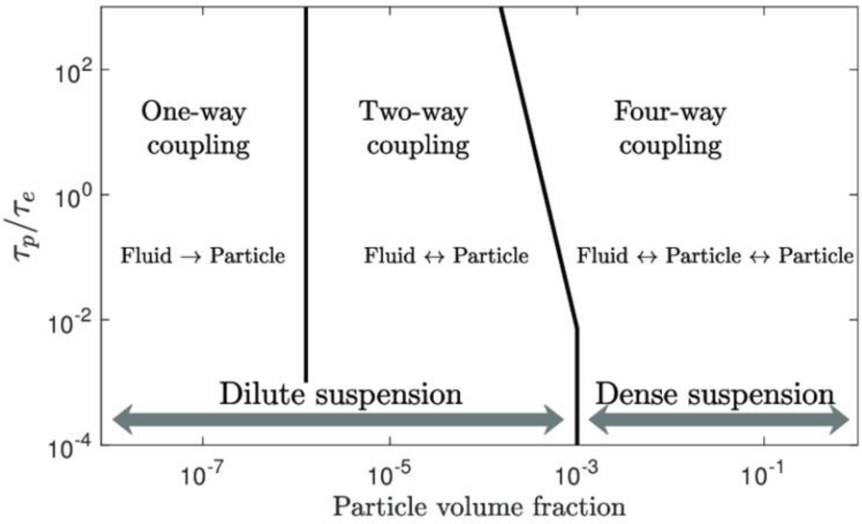

Source: Elghobashi, 1994.

It is essential, then, to observe the characteristics of the fluid flow and verify which type of configuration will be applied. The Lagrangian discrete phase model in Ansys Fluent® follows the EL approach described.

Figure 2.32 – Percentual change in turbulence intensity in function of particle diameter and turbulent length scale.

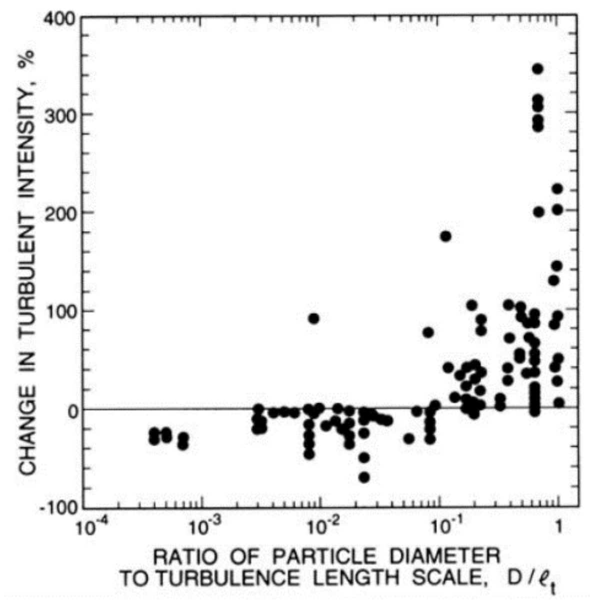

Source: Gore and Crowe, 1989; Brennen, 2005.

2.2.4.1. Particle Motion Equations: Discrete Particle Model (DPM)

The equations behind the particle motion are well described in the Ansys Fluent® theory guide 15.0 (ANSYS FLUENT®, 2013). The particles (disperse phase) are tracked through the calculated flow field. This approach is much simpler when the particle-particle interactions can be neglected, and the dispersed phase occupies a low volume fraction, even with a high mass load (ANSYS FLUENT®, 2013).

The particle force balance is how the solver performs the particle trajectory prediction (DUARTE, 2017). This prediction is made by integrating the force balance on the particle, placed on a Lagrangian framework, as it is presented in Equation 31.

$$m_p \frac{d\vec{u}_p}{dt} = \vec{F}_D + m_p \frac{\vec{g}(\rho_p - \rho)}{\rho_p} + \vec{F} \tag{31}$$

It is possible to verify that the equation above computes the drag force ($\overrightarrow{F_D}$), the gravity, directly activated on the solution, and other forces, computed by the term $\vec{F}$, that can include different effects like lift forces or virtual mass forces. The drag force ($\overrightarrow{F_D}$), modulus can be written as shown in Equation 32.

$$F_D = \frac{18\mu C_D Re}{\rho_p d_p^2 24} \tag{32}$$

And then, it is possible to confirm the C_D coefficient, the drag coefficient, which can be calculated differently. The difference between the fluid velocity ($\vec{u}$) and the particle velocity ($\overrightarrow{u_p}$) will be responsible for the particle movement. The Reynolds number used is presented in Equation 33:

$$Re = \frac{\rho d_p \vec{u}_p - \vec{u}}{\mu} \tag{33}$$

The Saffman lift force, or as pointed by the Ansys Fluent® theory guide 15.0 (ANSYS FLUENT®, 2013), the lift caused by the shear is a parcel that can be included on the $\vec{F}$ term shown before. The Saffman lift force equation is shown in Equation 34. The drag law used in this current work is the Spherical Drag Law, based on the constants (a_1, a_2, a_3) range given by Morsi and Alexander (1972), as shown in Equation 35.

$$\vec{F} = \frac{2K\nu^2{}_{ij}}{\rho_p d_p (d_{lk} d_{kl})^{1/4}} (\vec{u} - \vec{u}_p) \tag{34}$$

$$C_D = a_1 + \frac{a_2}{Re} + \frac{a_3}{Re^2} \tag{35}$$

An important non-dimensional parameter related to the multiphase flows is the Stokes Number (St). The Stokes number is a way to measure how the fluid flow will influence the particle. The particle response time is described in Equation 36. The characteristic flow time is described in Equation 37. The ratio between the τ_p and τ_f is the definition of the Stokes Number (St) as described in Equation 38.

$$\tau_p = \frac{\rho_p D_p^2}{18\mu_f} \tag{36}$$

$$\tau_f = \frac{D_h}{v_f} \tag{37}$$

$$St = \frac{v_f \rho_p d p_p^2}{18\mu_f D_h} \tag{38}$$

When the St << 1, the particle response time is very slow, and the particle usually takes a short time to change its motion and is very sensitive to fluid flow. On the other hand, when St >> 1, the particle response time is very high, and the particle usually is not sensitive to the fluid flow, and do not change its path easily.

2.2.4.2. Particle Dispersion by Flow Turbulence

The particle dispersion caused by flow turbulence can be computed using the stochastic tracking (random walk) model. This model includes the velocity fluctuations on the particle trajectories using stochastic methods. The solver uses the mean fluid phase velocity, $\bar{u}$, and the solver can equally use the velocity fluctuation, u', to compute the particle dispersion. The solver will then predicts the turbulent particle dispersion by integrating the individual particle trajectory equations using the instantaneous fluid velocity, $\bar{u}$ + u' , along the particle path during the integration (ANSYS FLUENT®, 2013). The prediction of particle dispersion holds on the integral time scale concept, T, as presented in Equation 39.

$$T = \int_0^\infty \frac{u_p{'}(t) u_p{'}(t-\tau)}{\bar{u}_p{'}^2}\, dt \tag{39}$$

This time is proportional to the particle dispersion rate, with more significant values showing a flow behavior more turbulent. If the condition of small tracer particles is analyzed, then it is possible to use the Lagrangian integral time, T_L, already written with $k - \omega$ variables, as shown in Equation 40.

$$T_L = C_L \frac{1}{\omega} \tag{40}$$

The Discrete Random Walk model, also known as the eddy lifetime model (ANSYS FLUENT®, 2013), calculates the interaction of a particle with a succession of discrete fluid phase turbulent structures. A Gaussian will characterize each structure distributed random velocity fluctuation (u’,v’,and w’) and a time scale τe. Using the concept that the kinetic energy of turbulence is known at each point in the flow and also assuming isotropic turbulence, it is possible to write the gaussian velocity fluctuations as a function of the kinetic energy, as presented in Equation 41.

$$\zeta\sqrt{\overline{u'^2}} = \zeta\sqrt{\overline{v'^2}} = \zeta\sqrt{\overline{w'^2}} = \sqrt{2k/3} \tag{41}$$

2.2.4.3. One-way Coupling

The solver uses the concept of parcels. Parcels are a group of particles with similar properties (diameter, velocity, or density.). With this concept is possible to reduce computational time. This concept is analogous to seeding particles in flow measurements. On the one-way coupling, the particle pattern is predicted based on the continuous phase flow field (ANSYS FLUENT®, 2013). Usually, as described before, this calculation is correct for dilute phases.

Continuously, as the particle trajectory is computed, the solver keeps track of the particle stream’s thermal energy, mass, and liner momentum gained or lost. It is shown in Figure 2.33 this flux works. It is essential to verify that once the particle receives the more linear momentum from the fluid flow, usually by the Drag Force, its acceleration will change, changing the position. Therefore the particle movement represents a transient behavior, each interacting with the fluid flow in int own way. Turbulence, as well, will significantly change the drag force injecting perturbations in the particle velocity.

Figure 2.33 – Transfer between discrete and continuous phase during the particle movement inside the control volume.

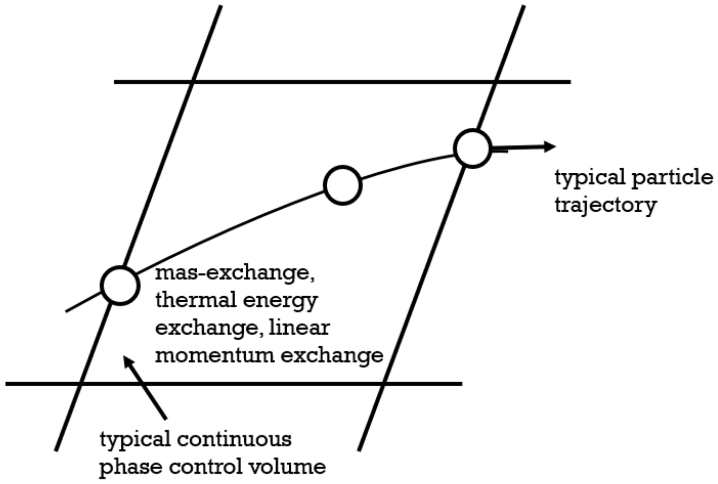

Source: Ansys Fluent®, 2013.

The momentum transfer from the fluid flow to the particles occurs by the solver as it passes through each control volume (ANSYS FLUENT®, 2013). This change is shown in equation 42.

$$F = \sum \left(\frac{18\mu C_D Re}{\rho_p d_p^2 24}(u_p - u) + F_{other}\right)\dot{m}_p \Delta t \tag{42}$$

Where μ = viscosity of the fluid, ρ_p = density of the particle, d_p = diameter of the particle, Re = relative Reynolds number, u_p = velocity of the particle, u = velocity of the fluid, C_D = drag coefficient, $\dot{m}_p$= mass flow rate of the particles, Δ_t= time step, and F_{other} = other interactions forces. Considering a one-way coupling, this momentum exchange will just be computed on the particles. The fluid flow is not affected by the particles.

2.2.5. Differential Model

It isdescribed in Section 2.2.5 the computational procedures to obtain the discretized equations of fluid flow and particle motion for both gas and particle pahses.

2.2.5.1. Gas Phase

For the current study, Ansys Fluent® is used. Like others with the same purpose, this solver uses the Finite Volume Method (FVM) to solve the flow field placed on a given geometry. The solution based on this approach is obtained by discretizing the previous equations in space and time (DUARTE, 2017). The FVM is a way to perform the partial differential equation (PDE) calculation and solution, transforming these equations into a group of algebraic equations (LEVEQUE et al., 2002; TORO, 2009). The FVM is similar to the finite element or finite difference method when it calculates the values on discrete places over a previously meshed geometry. In the FVM, the volume integrals in a partial differential equation containing a divergence term are converted to surface integrals using the divergence theorem (DUARTE, 2017). The terms are then evaluated as fluxes at the surfaces of each finite volume. The FVM method is conservative because the flux entering a cell volume is identical to the one leaving the same cell volume. The method also is better and quickly evaluated for unstructured meshes, as pointed out by Versteeg and Malalaskera (2007).

Ansys Fluent® uses two numerical approaches to perform the solution of a given flow configuration: the pressure-based solver and the density-based solver. The pressure-based solver was developed for low-speed incompressible flows and is the one chosen for the current work. The pressure field is extracted for this numerical approach by manipulating the momentum and continuity equations by solving a pressure or a pressure correction equation (ANSYS FLUENT®, 2013). Three different main points support the control-volume approach: the use of a grid, dividing the domain into discrete control volumes, the integration of the differential mathematical model for each control volume to obtain algebraic equations for the discrete dependent variables and the liinearization of the discretized equations, resulting in a linear equation system that will be further solved.

The used method of pressure-based solver belongs to a general class of methods called the projection method. This method achieves mass conservation by solving a pressure equation or correction (ANSYS FLUENT®, 2013). This pressure equation is derived from the continuity and momentum equations. All the equations in this solution are non-linear and coupled to one other, requiring multiple iterations until a convergence criterion is reached (ANSYS FLUENT®, 2013). It is presented in Figure 2.34 the pressure-based method diagram.

Figure 2.34 - Workflow of the pressure-based method used in the current work.

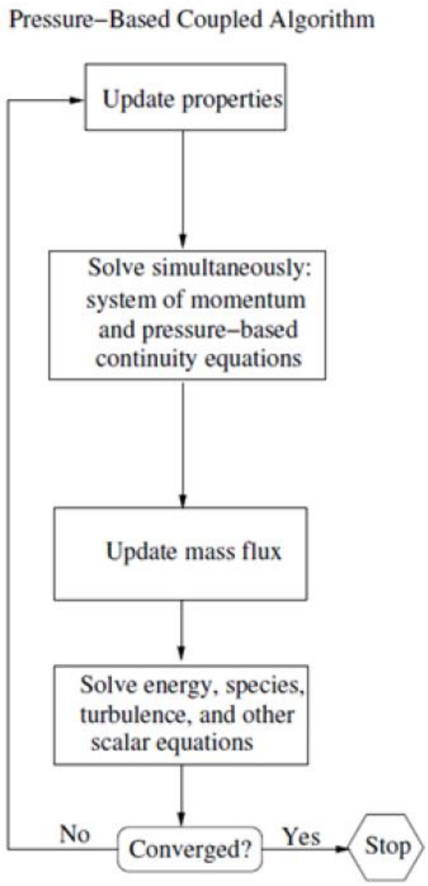

Source: Ansys Fluent®, 2013.

2.2.5.1.1 Equation Discretization and Solution

The solver uses a control-volume-based technique to transform a general scalar balance equation into an algebraic equation that will input the numerical solution. This technique integrates the balance equation about each control volume, yielding an equation that expresses the conservation law. Considering the unsteady general scalar balance equation shown in Equation 43.

$$\int_V \frac{\partial \rho\phi}{\partial t} dV + \oint \rho\phi\vec{v}.d\vec{A} = \oint \Gamma_\phi \nabla\phi.d\vec{A} + \int_V S_\phi dV \tag{43}$$

Where: ρ = density, $\vec{v}$ = velocity vector, $\vec{A}$ = surface are vector, Γ_ϕ = diffusion coefficient for ϕ, $\nabla\phi$ = gradient of ϕ, and S_ϕ = source of ϕ per unit volume. The discretization of this equation is shown in Equation 44.

$$\frac{\partial \rho \phi}{\partial t}V + \sum_{f}^{Nfaces} \rho_f \phi_f \vec{v}_f . \vec{A}_f = \sum_{f}^{Nfaces} \Gamma_\phi \nabla \phi_f . \vec{A}_f + S_\phi V \quad (44)$$

Where: N_{faces} = number of faces enclosing cell, ϕ_f = value of ϕ convected through face, $\rho_f \phi_f \vec{v}_f$ = mass flux through the face, $\vec{A}_f$ = area of face f, | A |, $\nabla \phi_f$ = gradient of ϕ at face f, and V = cell volume. This general discretized form is used for any desired variable over unstructured meshes. An illustration of a typical control volume was the discretization will be performed is shown in Figure 2.35.

Figure 2.35 - Discretization procedure over a control volume.

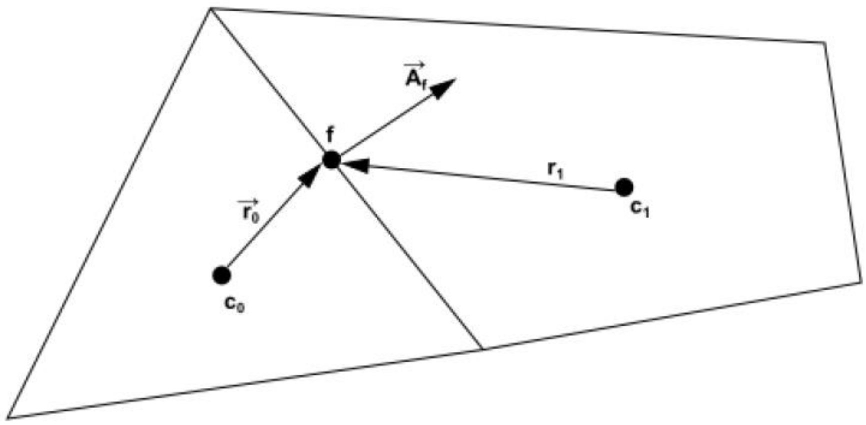

Source: Ansys Fluent®, 2013.

Usually the above equation will not be linear considering the unknown values shown in the figure above. A possible linearized form of the mentioned equation is shown in Equation 45.

$$a_p \phi = \sum_{nb} a_{nb} \phi_{nb} + b \quad (45)$$

N_b is the neighbors cells, and ap and anb are the linearized coefficients for φ. In the discretization procedure, usually, the solver stores discrete values of the scalar φ placed on the cell centers. Usually, face values, φ_f, are required for the convection terms and should be interpolated from the center values, the task accomplished by an upwind scheme (the face values are obtained from the quantities in the cell upstream of the face, relative to the normal velocity direction, ANSYS FLUENT®, 2013). One possible way to solve an upwind scheme is using the First-Order Upwind Scheme. As explained by Ansys Fluent® (2013), using a first-order upwind scheme, the cell-center values of any desired field variable are a cell-average value, and then this value is the same for the entire cell, including the value of this variable on the cell faces, φ_f, that will be equal to the center value of this variable, φ, in the upstream cell.

The pressure-velocity coupled system can be solved in different ways inside the Ansys Fluent® solver: SIMPLE method, SIMPLEC method, PISO method, Coupled and Fractional Step (FSM). According to Ansys Fluent® (2013), the Coupled method is more robust and efficient for single-phase implementation and steady-state flows, and it is superior considering non-segregating approaches. Usually, for steady-state calculations, under-relaxation factors are used, mainly because it is necessary to control the change of the considered variable on the non-linear equations to allow the solver to be more stable and not generate a convergence that can crash the solution. A selective amount of the desired variable is selected in the system of the discretized equations (ANSYS FLUENT®, 2013). This selection is performed over the discretized system as shown in Equation 46. α can be written in function of the Courant Number (CFL) proposed by Courant et al. (1928) shown in Equation 47.

$$\frac{a_p \phi}{\alpha} = \sum_{nb} a_{nb} \phi_{nb} + b + \frac{1-\alpha}{\alpha} a_p \phi_{old} \tag{46}$$

$$\frac{1-\alpha}{\alpha} = \frac{1}{CFL} \tag{47}$$

2.2.5.2. Particle Equation of Motion

The coupling between the gas phase and the particles is obtained as described by Duarte (2017) and Lain and Sommerfeld (2013), where first is solved the steady-state gas flow without the particles. In sequence, the particles are injected for each time step and tracked inside the domain. It is possible to control the particle time-step and fluid time-step (or pseudo-time-step, when it is a steady-state flow). Also, the number of time steps are required to perform the calculation. Ultimately, it will be necessary to observe if the statistics are representative, mainly when the problem is essentially transient. It is shown in Figure 2.36 the workflow of a one-way particle-gas coupling calculation, based on the work of Lain and Sommerfeld (2013).

Figure 2.36 - Calculation pipeline for the one-way gas-particle coupling.

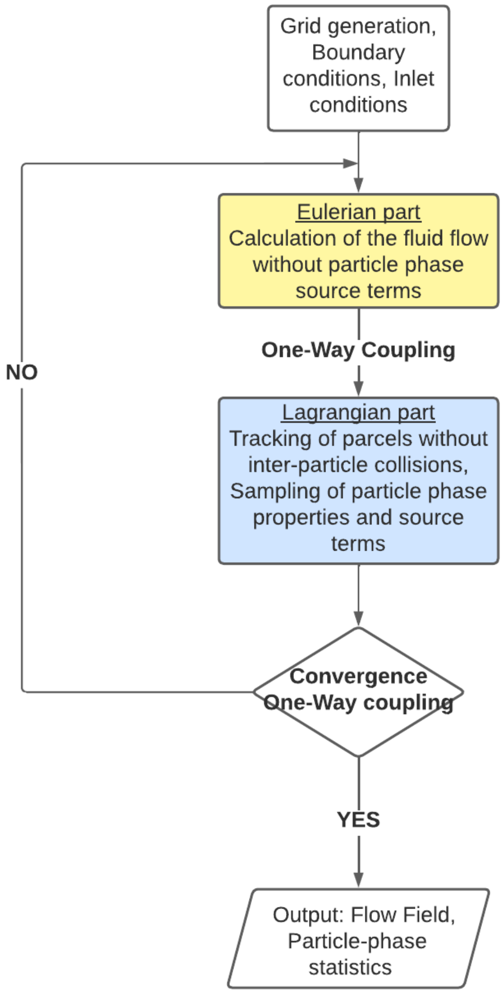

Source: adaptaded from Lain and Sommerfeld, 2013.

According to Ansys Fluent® (2013), the trajectory equations are stepwise integrated over a discrete number of time steps, yielding the particle's velocity at each point along the trajectory. The trajectory prediction is shown in Equation 48. Combining Equation 48 with the Equation 31 is possible to obtain the algebraic differential mathematic model for particle movement, described in Equation 49.

$$\frac{dx}{dt} = u_p \tag{48}$$

$$\frac{du_p}{dt} = \frac{1}{\tau_p}(u - u_p) + a \tag{49}$$

This general form represents the set of previous mentioned equations, and can be solved on the form presented in Equations 50 and 51, for u, a and τ_p.

$$u_p^{n+1} = u^n + e^{-\frac{\Delta_t}{\tau_p}}(u_p^n - u^n) - a\tau_p(e^{-\frac{\Delta_t}{\tau_p}} - 1) \tag{50}$$

$$x_p^{n+1} = x_p^n + \Delta_t(u^n + a_p) +_p \tau_p(1 - e^{-\frac{\Delta_t}{\tau_p}})(u_p^n - u^n - a\tau_p) \tag{51}$$

There are different methods to solve the equations 50 and 51 . The one used by the solver to verify the particle position is the discretization scheme, where the new particle location is always given by a trapezoidal discretization as shown in Equation 52.

$$x_p^{n+1} = x_p^n + \frac{1}{2}\Delta_t(u_p^n + u_p^{n+1}) \tag{52}$$

2.2.6. Computational Model

The solver used in all analyses proposed in the current work is Ansys Fluent®. This solver already has good capabilities and solutions procedures, and considering the nature of the problem being studied in this current work, the heavily extensive Ansys Fluent® documentation can help make more accessible the project discovery process. Ansys Fluent® has already been passed by scientific justification and validation, considering that the solver code has been on the market since 2006. The solver also has a solid Discrete Particle Model (DPM) model with multiple approaches tested for different multiphase flow applications.

CHAPTER III

MATERIALS AND METHODS

The methodology applied in this current work has the main objective to create simulations to validate some hypotheses previously formulated about a low-cost computational model to simulate the particle deposition fluid dynamics using a coaxial nozzle. A 2D axisymmetric model integrated with a RANS turbulence model (SST-kω) was developed. Usually, with 2D models, some flow characteristics are lost, mainly when considering the turbulence effects. However, this work aims to obtain the multiphase flow global behavior with the central mean values. Bosioc *et al.* (2009) show that the 2D axisymmetric results are in good agreement with the 3D ones for decelerated swirling flows, and this approach provides valuable information without a high computational cost. Susan-Resiga *et al.* (2009) compared a 2D axisymmetric model with a 3D one and the related experimental data and obtained a correct estimation regarding the control of the vortex rope when using an axial jet to eliminate the problematic stagnation region. The current study has no significant stagnation region, and the flow is close to a jet flow. Then is expected that the 2D axisymmetric model can be sufficient to obtain the desired values proposed in this current work.

3.1 Validation Methodology of the Gas Flow Computational Model based in the work of Sebastian *et al.* (2021)

3.1.1 Study Developed by Sebastian et al. (2021)

Sebastian *et al.* (2021) created a CFD model to simulate a three-channel (internal gas channel, carrier gas channel, and shield gas channel) coaxial nozzle presented in Figure 3.1.

Figure 3.1 - 3D drawing used for the gas flow study developed by the author. It is important verify the use of the half domain with the symmetry boundary condation applied.

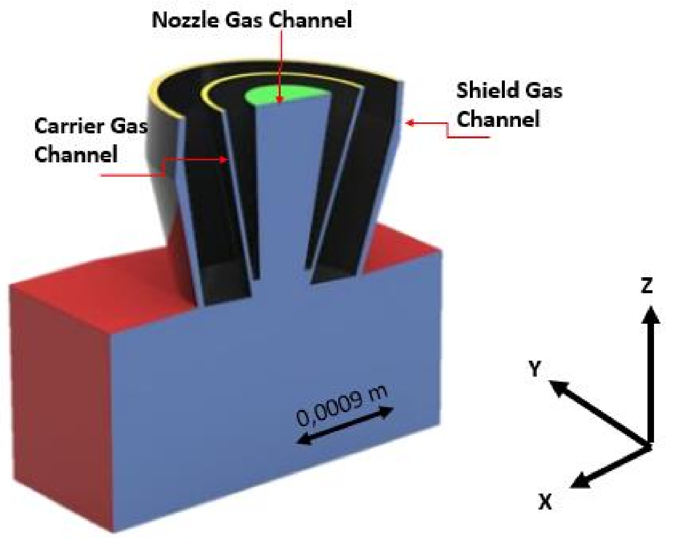

Source: Sebastian *et al.,* 2021.

To evaluate the gas flow behavior on six different inlet volume rate conditions according to the nozzle manufacturer of reference. The conditions are presented in Table 3.1. For this first analysis, the idea was to test and validate a monophasic model, just considering a nozzle and the inert gas dynamics. The model was based on a material experiment developed with the same conditions presented in Table 3.1. The material experiment configuration is shown in Figure 3.2.

The gas flow is treated as steady-state turbulent flow, modeling constant gas density and no-slip conditions at walls. It used the polyhedral mesh, and the final geometry contained the total of 2 433 130 elements, refined at gas inlets, walls, symmetry plane, and bottom outlet. It was set for the turbulence model, the k-ε Reynolds-Average Navier Stokes (RANS) model. The material experiment was set up as shown in Figure 3.2. The pitot tube was placed aligned with the fluid flow center and used a micromanometer TSI8705® to obtain the fluid flow velocity. The pitot tube was fixed in a three-jaw chuck positioned at the origin of the coordinate machine system. The chuck center was found using a RENISHAW® OMP 60 OPTICAL probe. Flow velocities were measured at 1 mm radially (X and Y) and at every 2 mm in the Z direction, from 0 mm to 10 mm below the nozzle.

The experiment was set variating the position of the pitot tube position to capture the gas flow patterns in different radial regions of the wok table. However, the three-chuck is not presented in the computational model and a horizontal solid plate is placed at the bottom of the nozzle.

Table 3.1 - Experiment configuration used for the study, including the flow rate for each channel (SEBASTIAN *et al.*, 2021).

Conditions	**Nozzle - m^3/s**	**Carrier - m^3/s**	**Shield - m^3/s**
A	0,0001002	0,0000668	0,000167
B	0,0000334	0,0000668	0,000167
C	0,0000668	0,0000835	0,0001336
D	0,0000501	0,0001002	0,0001503
E	0,0000835	0,0001169	0,0001002
F	0,0000668	0,0000668	0,0001336

Figure 3.2 - Experiment setup used for the study.

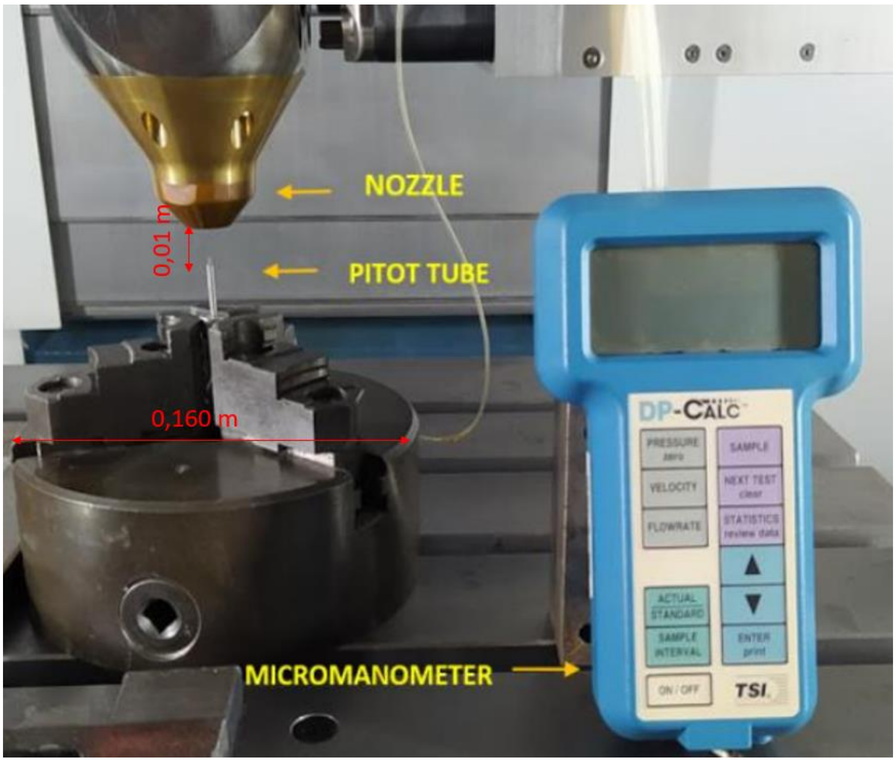

Source: Sebastian *et al.,* 2021.

3.1.2 Simulation workflow and Geometry Setup

Condition E was selected for the current study, presented in the work of Sebastian et al. (2021). The analysis was performed at 10 mm below the nozzle.It is presented in Figure 3.2 the procedure used in this current work. The goal is to develop a new model based on the Sebastian et al. (2021) model using a 2D geometry with the axisymmetric condition. The model geometry dimensions were obtained from the drawing presented in the study developed by the reference author, using CAD software to get all the needed dimensions measurements

Figure 3.3 – Simulation workflow. The geometry obtained from the Sebastian *et al.* (2021) is used to create the model used for the study. The validation is performed using the author's results and then the 2D multiphase model is created.

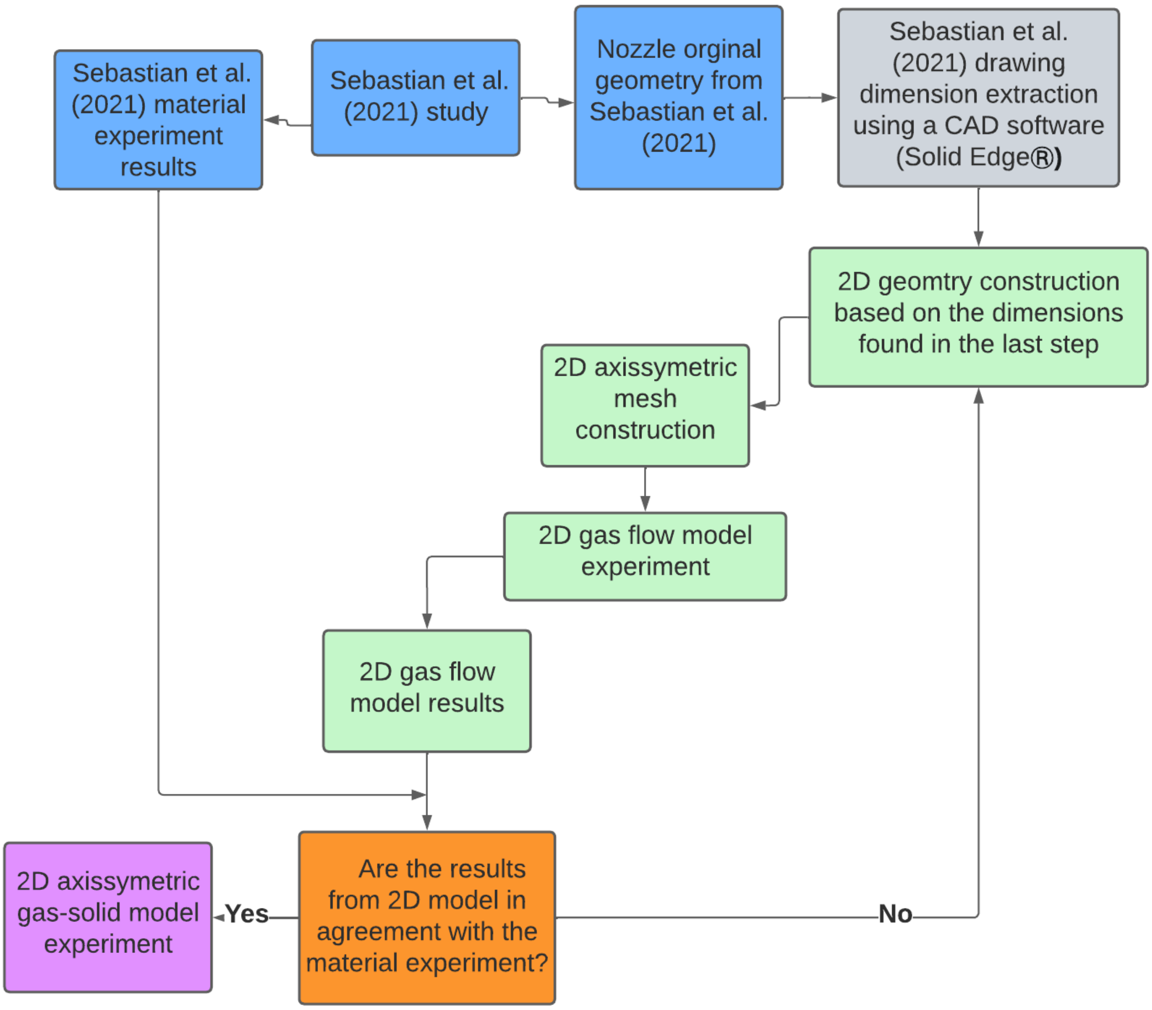

From the study setup image, Figure 3.3, the dimension from the three-jaw chuck was obtained using the same procedure described, inputting the image in scale in CAD software and performing all the needed measurements. Based on the above measurements it was constructed the 2D-axisymmetric geometry with the 3-jaw chucks. In this specific case, the jaws were represented in a planar way.

After the geometry construction, the mesh building procedure was started. The mesh was initially generated with an overall cell number. Usually, this first mesh generation produces a very coarse mesh. Different mesh refinement procedures were then performed, including an overall mesh refinement based on a face refinement.

Each of these refinements included several divisions that controlled the mesh refinement. Three probe points were selected, and the velocity on these points was evaluated separately. Then they were plotted in function of the different number of cells used, and this graph was used to select the minimum number of cells to guarantee mesh convergence. The position of these probe points is seen in Figure 3.4.

Figure 3.4 - Probe points position on the geometry. These probes were placed in the positions to capture the velocities in the regions with higher gradients.

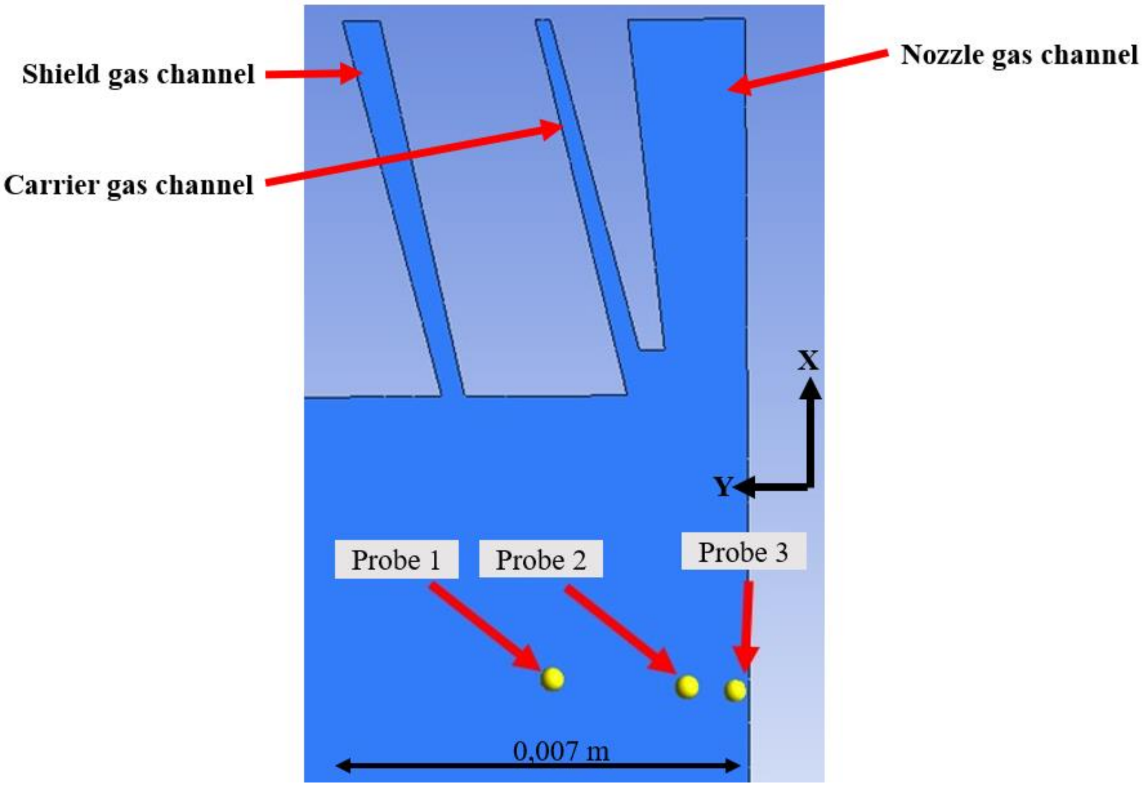

3.1.3 Boundary Conditions and Simulation Configuration Applied

After the mesh convergence evaluation, the selected mesh is input into the Fluent Solver, and the boundary conditions are set up. The condition used is the condition E from the Sebastian *et al.* (2021) experiment, with 0,00008385 m^3/s for the nozzle gas inlet, 0,0001169 m^3/s for the carrier gas inlet, and 0,0001002 m^3/s for the shield gas inlet. For this current study the gas used was argon, with the density being ρ = 1,6228 kg/m^3 and kinematic viscosity being ν = $2{,}125.10^{-5}$ Ns/m^2 .

The inlet boundary conditions were set for the inlets, the wall boundary conditions were set for the nozzle walls, for the 3-jaw chucks, and the outlet (atmosphere) boundary condition was selected for the lateral and between the carrier gas channel and the shield gas channel. Finally, the center axis was defined as an axis boundary condition. It is possible to check the mesh used in Figure 3.5.

Figure 3.5 - Boundary Conditions used on the current study 1, including the Axisymmetric axis used to replicate the cylindrical condition.

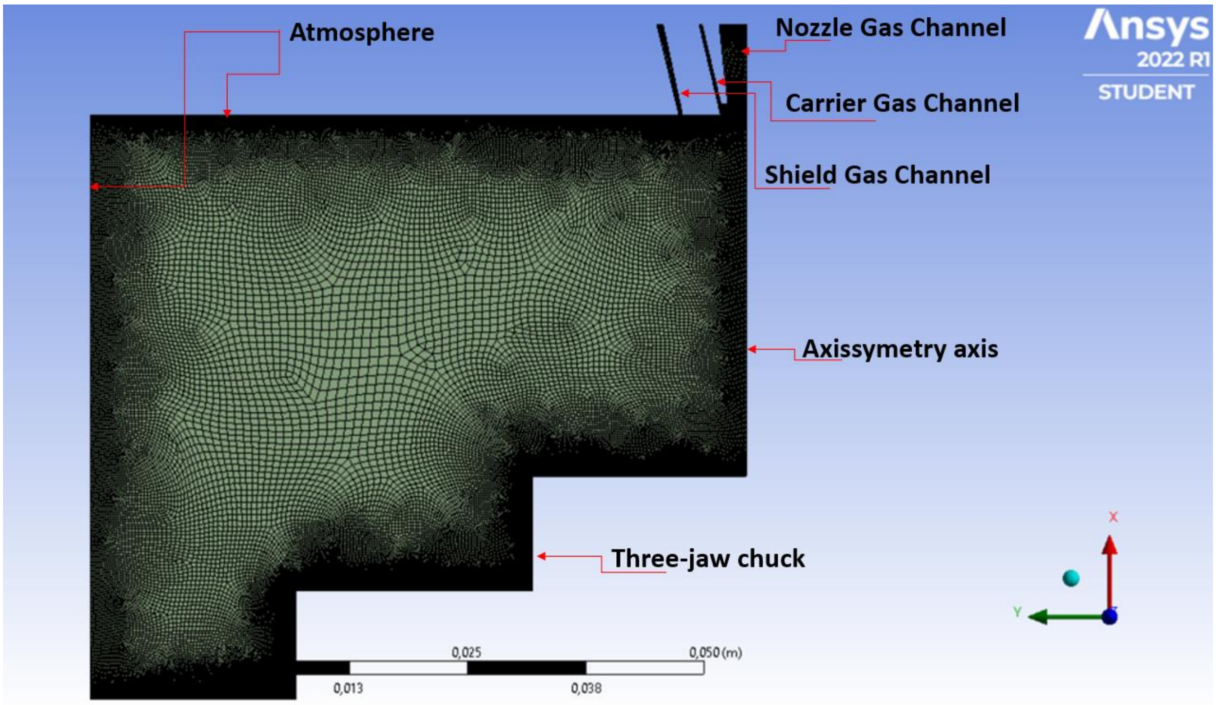

3.1.4 Results Evaluation

A comparison was developed based on the values of Figure 3.6 (SEBASTIAN *et al.*, 2021). The values to perform the comparison were taken from the same position as the one used by Sebastian *et al.* (2021), with the same boundary and initial conditions. It is observable that the material experiment results diverge from the simulation results. This difference occurred because the numerical model does not present the three-jaw chuck.

The effect of this part is essential for the fluid flow behavior and significantly impacts the gas velocity curve, as presented in the results. Then a measurement was taken from 10 mm below the nozzle, vertically. It is necessary to observe that the nozzle at Sebastian *et al.* (2021) has some inclination concerning the vertical line that is not considered in the current work. Then observing the graph taken from their work is possible to see the difference between the two peaks that will not be present in this current work. However, the peak intensity and shape should be similar to the material experiment observed by Sebastian *et al.* (2021). The curve obtained in this current work was compared with the curves obtained from the computational and material experiment by Sebastian *et al.* (2021).

Figure 3.6 - Gas velocity comparison curves in condition E and measured 10 mm below the nozzle.

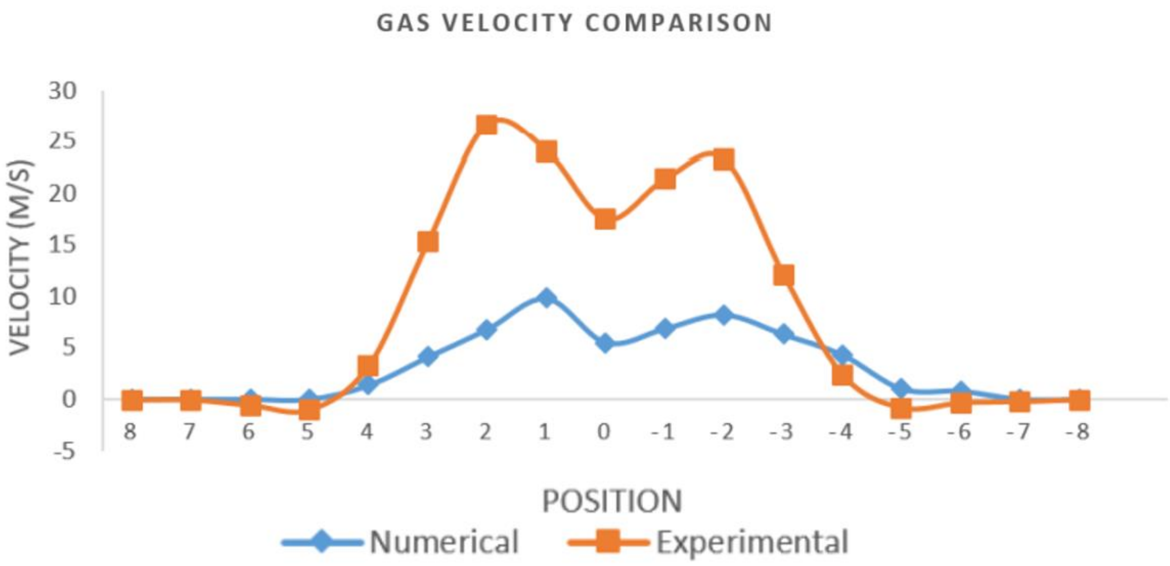

Source: Sebastian *et al.*, 2021.

3.2 Simulation of the two-phase argon-particles flow inside the nozzle

The second part of the current study proposes a multiphase analysis applied to the same geometry evaluated in study 1 of this current work, based on the work of Sebastian et al. (2021). This study proposes a more straightforward method to evaluate particle deposition and nozzle efficiency based on more general and dimensionless variables (Reynolds Number and Stokes Number). This data can help the machine operators, researchers, and engineers work with operation curves and select multiple machinery arrangements to perform the deposition task.

For this simulation, the geometry and mesh from first study are used. Both were already validated and can be directly used as input for the model. The three-jaw chuck was taken off, and a horizontal plate was put in place to simulate a planar deposition, making the model more uncomplicated and performing a planar deposition study that could be replicated easier. Therefore, the mesh without the three-jaw chunk is more refined and keeps the mesh convergence. The 2D axisymmetric model mesh used in the second analysis is shown in Figure 3.7.

Figure 3.7 - 2D axisymmetric mesh used for the multiphase analysis. It is possible to verify that a flat plate is used instead of the three-chuck jaw. The position of the flat plate is set 10 mm below the nozzle exit, to capture the nozzle focal position.

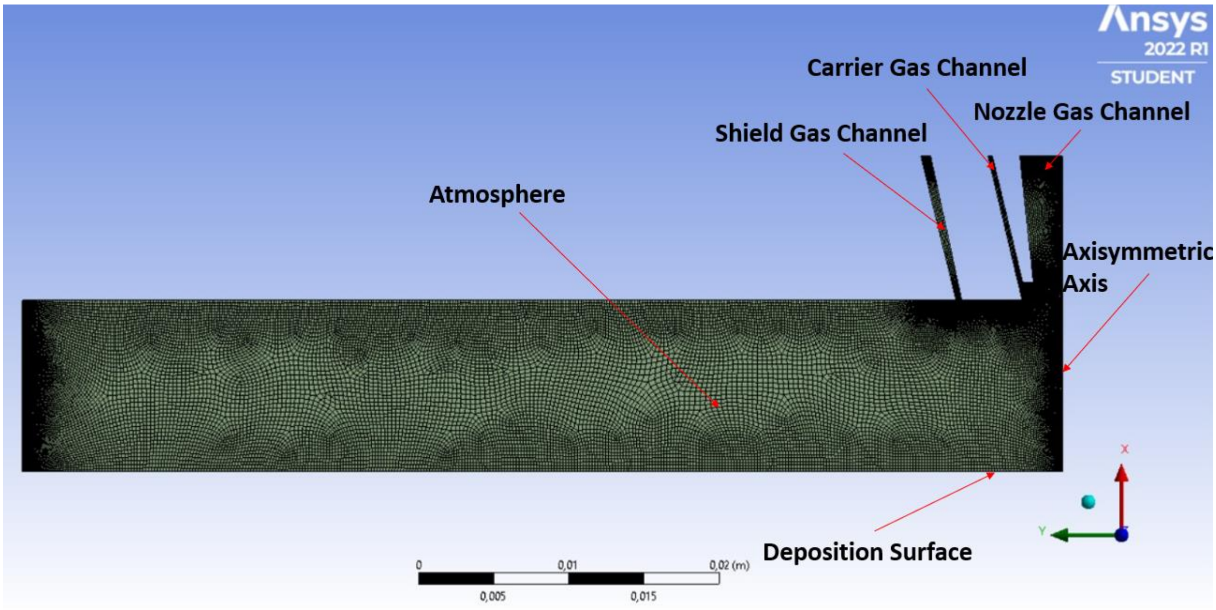

The gas boundary conditions from the study presented in Section 3.1 are also replicated fin the study proposed in Section 3.2, considering argon as the gas used and all the gas properties. It used the Discrete Particle Model (DPM) present on the Ansys Fluent®. This module allows the user to configure all the main multiphase flow characteristics like the particle diameter, particle flow rate, the Drag model used, and other forces that can eventually be present on the flow. Also, it is possible to configure the particle density, velocity on the entrance, and the multiphase operation regime, which means one-way coupling, two-coupling, or four-way coupling.

3.2.1 Variables Used on the Problem Study

For the current study, the following variables were used to perform the calculations and better understand the problem analyzed: Hydraulic Diameter (D_h), Reynolds Number (Re),Stokes Number (St), Particle Concentration (C), particle mass flow rate ($\dot{m}_p$) and particle density (ρ_p).

The D_h is used when a non-circular duct is used. Using this concept, it was possible to use the same equations with the equivalent D_h. Its definition is presented in Equation 53.

$$D_h = \frac{4A}{P} \tag{53}$$

For the current study, conical ducts with an area reduction simultaneously exist. Considering the internal area and perimeter, the D_h was calculated at the carrier channel exit. After performing the simplification, the D_h can be re-written as presented in Equation 54.

$$D_h = 2(r_{ext} - r_{int}) \tag{54}$$

The r_{ext} is the external radius of the carrier channel exit, and r_{int} is the internal radius of the carrier channel exit. This procedure was also used in Petters and Pozzetti (2020) and Guan and Zhao (2020). The calculated value for the D_h was 0,00046 m.

The C measures how much particle mass is inside each cell's volume. Considering that the particle is traveling with a given mass flow rate ($\dot{m}_p$) and has a given residence time (t_p), then the product between this two will give the particle mass at a given instant. The ratio between this value and the cell volume (v_c). The cell volume is a projection based on the 2D mesh and axisymmetry. The formula presented in Equation 55 demonstrates how the Particle Concentration is calculated:

$$Particle_{Concentration} = DPM_{Concentration(namefromFluent)} = \frac{t_p \dot{m}_p}{v_c} \tag{55}$$

Both non-dimensional numbers, Reynolds Number and Stokes Number, use flow and particle characteristics already mentioned here. The goal is to perform an experiment setup variating these numbers to check how they influence the C value.

3.2.2 Bibliographic Research to Particle Data

A study was performed to check the main particle characteristics and flow regimes configured. It was used in eleven previous studies, and the maximum diameter, minimum diameter, mass flow rate, and particle density were considered. Then the particle mean diameter and the particle mean flow rate were calculated, and these values were kept for the study proposed here. The data is presented in Table 3.2.

Based on the analysis described above, the mean particle diameter value calculated was dp = 84,38 µm and the powder mass flow rate calculated was 0,00011409 kg/s . This current study will consider the influence of the fluid flow in the particle (one-way coupling), and the drag law used is spherical. The current study also considered gravity (the acceleration vector was in the same direction as the x-axis but in the opposite sense). This study used the concept of non-dimensional variables named Reynolds Number (Re) and Stokes Number (St). The next section will give a different notion about how both variables were used in work.

Table 3.2 - Bibliographic research for particle properties configuration.

Authors	D_h - m	$\dot{m}_p$ - kg/s	ρ_p - kg/m^3
Takemura *et al.* (2019)	0,00000790	0,00030000	8440
Ferreira *et al.* (2020)	0,00000800	-	8200
Lin and Steen (1998)	0,00001050	0,00003000	8000
Arrezubieta *et al.* (2014)	0,00000725	-	8200
Ferreira *et al.* (2018)	0,00000750	0,00006667	8190
Ibarra-Medina, Vogel and Pinkerton (2011)	-	0,00000280	-
Lee (2008)	0,00000600	0,00022000	7850
Vetter, Engel and Fontaine (1994)	0,00001000	-	8690
Li, Zhang and Liou (2018)	0,00000905	-	-
Nalam *et al*. (2021)	-	0,00002667	7730
Yao *et al.* (2021)	0,00000975	0,00015250	-

3.2.3 Properties and Boundary Conditions

The experiment plan consists of variating the Reynolds Number and the Stokes Number and verifying how this influences the C value. To perform this the particle diameter (d_p), the fluid viscosity (μ_f), the D_h and the fluid density (ρ_f) are kept constant equal to: $d_p = 50\ \mu m$, $\mu_f = 0{,}00002125\ Pa.s$, $D_h = 0{,}00046\ m$, $\rho_f = 1{,}6228$ kg/m³. It is presented in Table 3.3 how Reynolds and Stokes Numbers were evaluated.

Table 3.3 - Re and St variation plan to verify the influence in the particle concentration.

Re	250				
St	200	400	800	1 200	1 600
Re	500				
St	200	400	800	1 200	1 600
Re	1 000				
St	-	400	800	1 200	1 600
Re	1 250				
St	-	400	800	1 200	1 600

The argon gas velocity is calculated for each Re and the particle density for each Re and St proposed. It was selected the SST-kω turbulence model and the DRW model for particle turbulence dispersion with one-way gas-particle coupling. The particle injection was set up on the carrier gas channel inlet face. The particle density and particle mass flow rate were set up according to the bibliographic research performed previously. The diameter was considered constant and equal to the mean diameter found in the bibliographic research performed previously. The DPM was set as a transient calculation with a time step first set equal to 0,01

s. This value allows a fast simulation to verify if the process goes to a steady state or goes a transient state. To perform particle visualization the time step was reduced to 0,0001 s, following the same calculation sequence. And then following simulation iterations were run to collect the particle tracking visualization.

An important point to be confirmed is the data post-processing if the process is transient. It needs a temporal mean of the desired variable over different time samples, and then it is necessary to check when this mean starts to be constant over time. The results are good when the difference is at least one decimal place. This procedure should be applied if the transition behavior is verified.

3.2.4 Analysis Procedure

The analysis procedure is important to correct capture the effects desired in the study. It is shown in Figure 3.8 the probe position on the center of the deposition area.

Figure 3.8 - Probe position on the evaluated geometry.

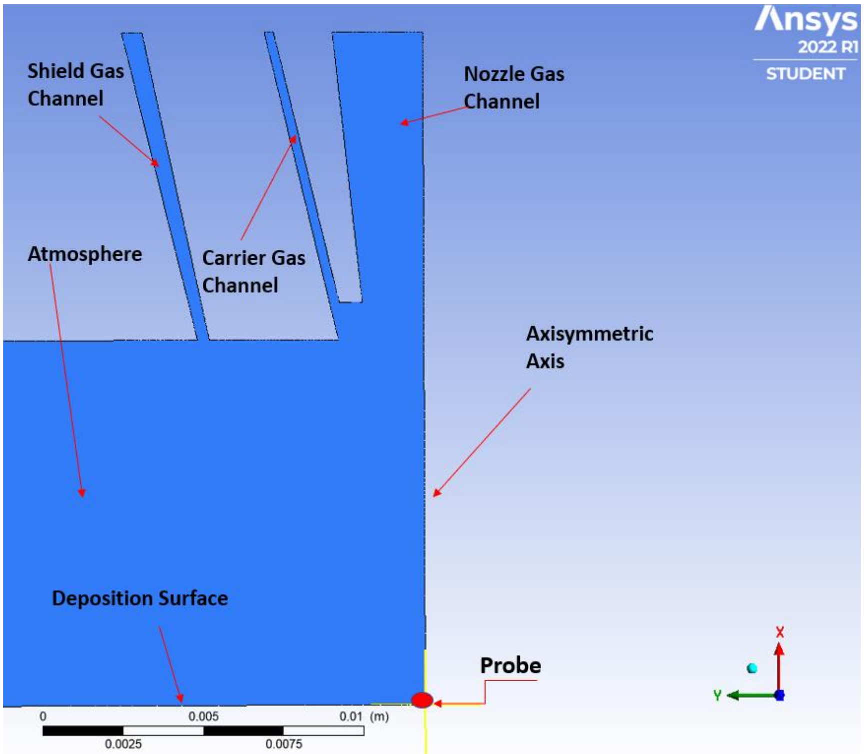

The variable analyzed on the post-processing tool was the C value (in Ansys Fluent® is the DPM Concentration value, in kg/m³). This variable was analyzed on the position shown in Figure 3.8. The results were stored for all time steps, calculated, and then processed to verify the transient behavior. Also, it was verified that the influence of the St and Re on the particle concentration.

CHAPTER IV

RESULTS AND DISCUSSIONS

4.1 Validation Methodology of the Gas Flow Computational Model based in the work of Sebastian *et al.* (2021)

The results obtained from the two experiments will be presented in this section. The sequence will follow the previous chapter order, including the results of the first experiment and the results of the second experiment.

4.1.1 Mesh Analysis Results

The mesh analysis results are presented in Table 4.1, considering the velocity magnitude evaluated on the three described probes in Figure 3.4.

Table 4.1 - Mesh analysis results, V_1, the gas flow velocity obtained from probe 1 of Figure 3.4, V_2, the gas flow velocity obtained from probe 2 of Figure 3.4, and V_3, the gas flow velocity obtained from the probe 3 of Figure 3.4.

Number of elements	V_1 **- m/s**	V_2 **- m/s**	V_3 **- m/s**
55 662	3,97822	13,9625	6,84917
64 775	4,1376	14,7165	6,74145
84 449	4,15144	15,3866	6,87975
113 022	4,19293	15,9555	7,07798
143 797	4,58161	15,7655	7,14719
222 632	4,05745	15,9396	7,06915

Based on Table 4.1, it is possible to examine that for the velocities collected on the probes 2 and 3 shown in Figure 3.4, the values started to converge for a constant value. The velocity collected on the probe 1 shows a divergence around 150 000 cells, that should be further investigated. Considering the results obtained from probes 2 and 3, it is possible to verify that after 100 000 the mesh does not have too much influence over the velocity value, which means the results are independent of the mesh. Therefore, increasing the number of cells in this value will increase the computational cost without any further benefits. However, considering this current study is a validation study, the mesh with the most extensive cell number was selected for precaution.

Figure 4.1 - Mesh analysis results based on three different probe positions.

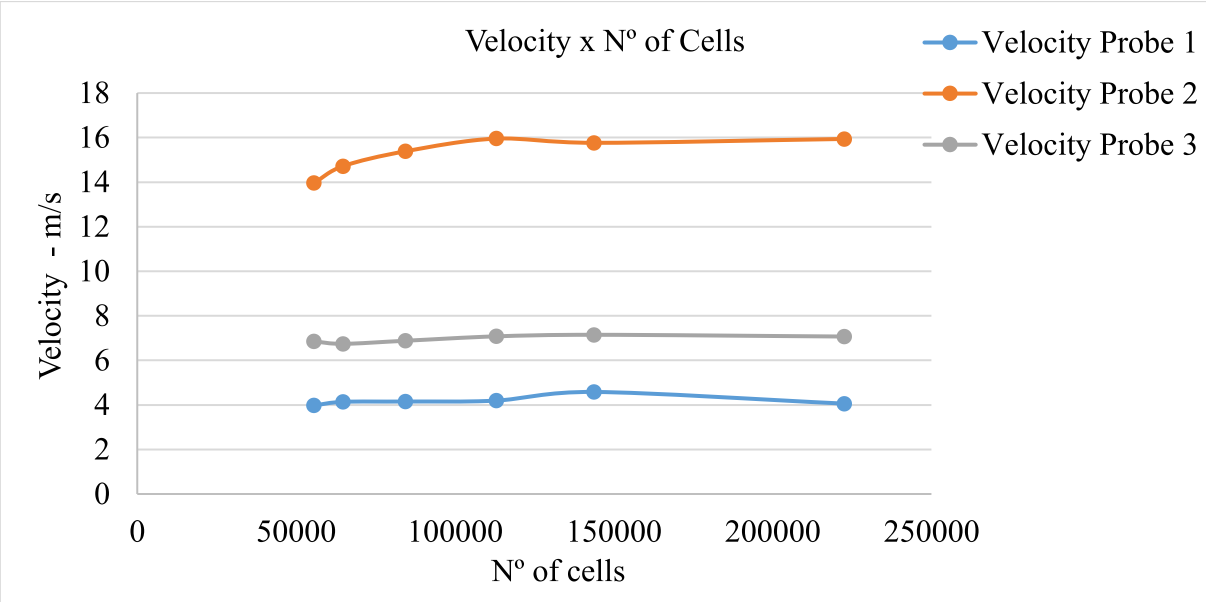

4.1.2 Velocity Profile Comparison Results

In the selected mesh, with 208 thousand cells, the simulation with condition E, described in Table 4.1 from Sebastian *et al.* (2021), was then performed. The values of the velocity modulus from the line 10 mm below the nozzle, presented in Figure 3.6, were compared with the reference study. The velocity comparison graph is presented in the Figure 4.2 and the isovalues of argon velocity modulus are shown in the Figure 4.3. It is observed in Figure 4.2 that the numerical model developed in this current study is closer to the material experiment proposed by Sebastian *et al.* (2021) and represents better the problem physics than the computational experiment proposed by Sebastian *et al.* (2021). The presence of the three-chuck jaw probably is the most significant reason behind this better result, mainly due to the fluid flow effects and the pressure rise due to the jaws, even with the jaw being represented here as a two-dimensional part.

Figure 4.2 - Velocity modulus results comparison, including the reference author results and the simulation developed in the present study. It is possible to verify that the velocity profile in the radial direction obtained from the computational model proposed in the section 3.2 is closer to the material experiment results proposed by the reference author.

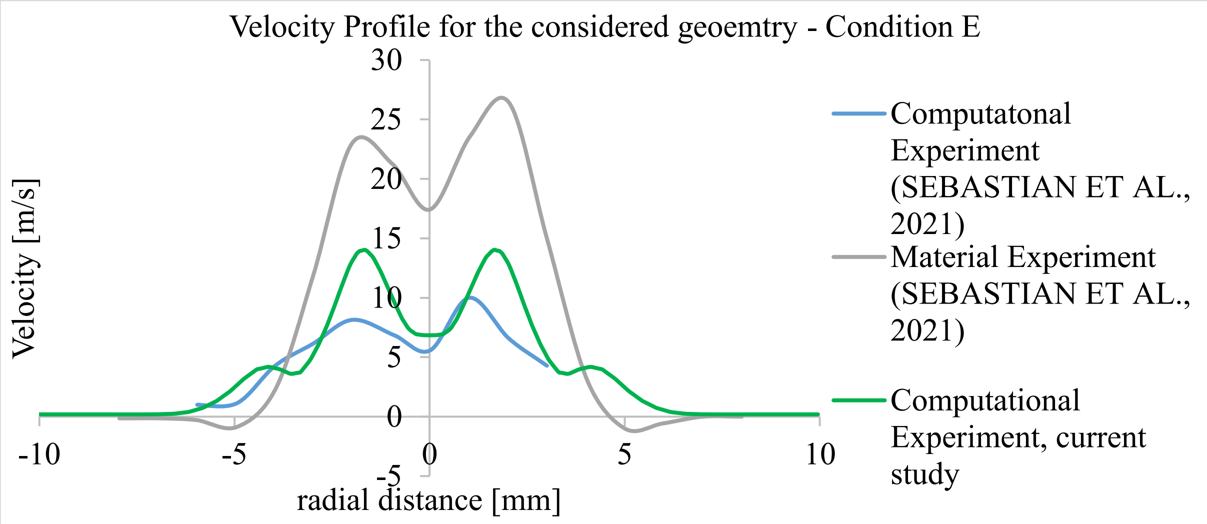

Figure 4.3 - Isovalues for the argon velocity modulus under condition E, described in Table 3.1, considering the proposed model in the current work.

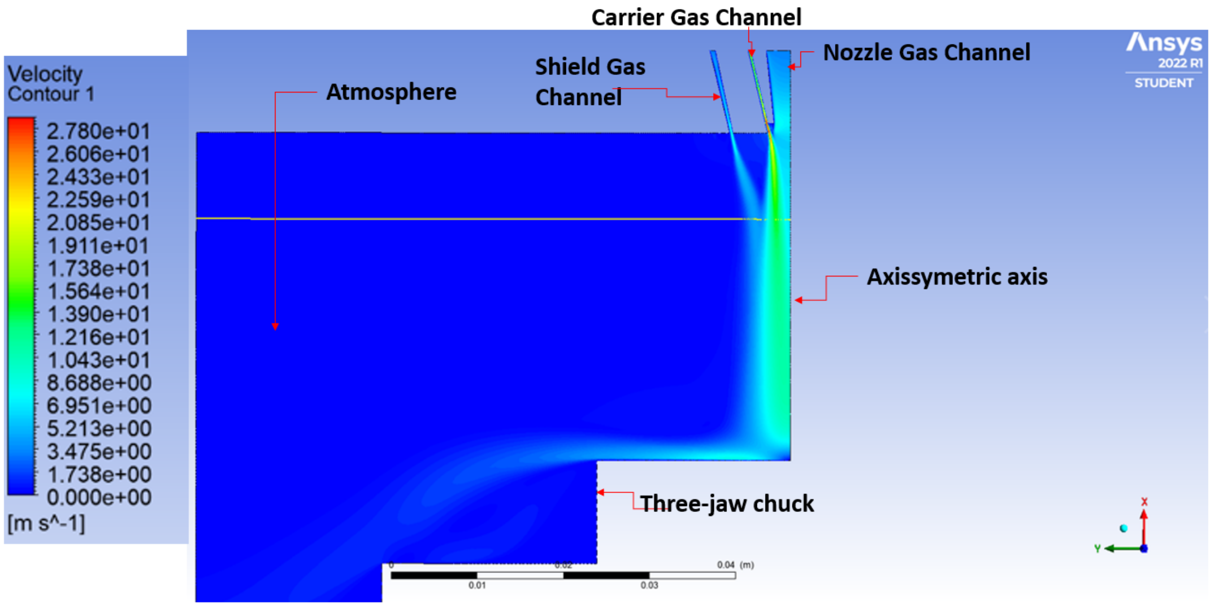

4.2 Simulation of the two-phase argon-particles flow inside the nozzle

The results obtained from the 18 experiments, described in Table 3.3, are presented in this section. First is presented in Section 4.2.1 the time averaged results obtained from time sampling procedure and is presented in Section 4.2.2 the particle tracking visualization. It is as well presented the time step size study performed to check the impact in particle agglomeration.

4.2.1 C Averaged Results

It is necessary to calculate the values of the temporal averages according to each case analyzed and ensure that, for consecutive samples, the differences between these values go to a number smaller than unity, the lowest possible. The following sequence presents this procedure. C is analyzed on the central point shown in Figure 3.8.

4.2.1.1 C Averaging for Reynolds Number (Re, described in Subsection 3.2.1) = 250

It is possible to verify the time averaging procedure by observing Tables 4.2 to 4.6. The time-averaged C and the difference between consecutive time-averaged C values are calculated. Once this difference value is below the unity, the respective time-averaged C value is used. The results verified in Tables 4.2 to 4.6 show that for all the Stokes Number studied, the difference between consecutive time-averaged C is below the unity, as required. It is possible to review also that for the different Stokes Number (St, explained in Subsection 3.2.1), the sample size needed to perform the time average procedure is different. It is possible to observe by comparing Tables 4.2 to 4.6 that increasing the St the C value increases. For St = 1 600, Table 4.6, the C have an expressive value. For this specific combination of Reynolds Number = 250 and Stokes Number = 1600, the particle has low influence from the fluid flow and, hence, higher is the volume of particle arriving in the deposition surface shown in Figure 3.8.

Table 4.2 - Time-averaged C calculation for Re = 250 and St = 200.

Sample	C	Diference [(Mean n)-(Mean n-1)]	Sample Elements Number
1	113,0785	0	100
2	112,0571	1,021337476	200
3	112,6643	0,607137176	300
4	113,1853	0,521053328	400
5	113,5738	0,388526142	500
6	113,7119	0,138047203	600

Table 4.3 - Time-averaged C calculation for Re = 250 and St = 400.

Sample	C	Diference [(Mean n)-(Mean n-1)]	Sample Elements Number
1	125,9711	0	100
2	131,9944	6,023324271	200
3	131,8826	0,111862996	300
4	132,4506	0,568011804	400
5	131,657	0,793622855	500
6	131,6748	0,017824577	600

Table 4.4 - Time-averaged C calculation for Re = 250 and St = 800.

Sample	Mean	Diference [(Mean n)-(Mean n-1)]	Sample Elements Number
1	195,6938	0	100
2	169,0468	26,6470272	200
3	160,7774	8,269400159	300
4	157,6534	3,123975608	400
5	154,0921	3,561329801	500
6	151,8528	2,239310994	600
7	150,5424	1,310361111	700
8	149,7548	0,787640708	800

Table 4.5 - Time-averaged C calculation for Re = 250 and St = 1 200.

Sample	Mean	Diference [(Mean n)-(Mean n-1)]	Sample Elements Number
1	195,9302	0	100
2	187,3741	8,556159	200
3	182,3545	5,019522483	300
4	181,5621	0,792451384	400
5	179,9017	1,660350998	500
6	178,5168	1,384930149	600
7	177,0974	1,419365769	700
8	176,6958	0,401653579	800

Table 4.6 - Time-averaged C calculation for Re = 250 and St = 1 600.

Sample	Mean	Diference [(Mean n)-(Mean n-1)]	Sample Elements Number
1	363,9416	0	100
2	371,2748	7,333239715	200
3	369,3554	1,91942826	300
4	372,2092	2,85378349	400
5	365,7127	6,496410892	500
6	365,3713	0,341466863	600

4.2.1.2 C Averaging for Re = 500

It is possible to verify the time averaging procedure by observing Tables 4.7 to 4.11. The sample elements number indicates the number of elements used for the average calculation. Then time-averaged C and the difference between consecutive time-averaged C values are calculated. Once this difference is below the unity, the respective time-averaged C value is used. The Stokes Number influences the transient behavior of C value analyzed. The results verified in Tables 4.7 to 4.11 show that for all the Stokes Numbers studied, the difference between consecutive time-averaged C values is below the unity, as required. It is possible to verify as well, for different Stokes Numbers, that the sample size needed to perform the time average procedure is different. It is possible to observe also the increase in the C value by increasing the St, as it is possible to analyse comparing Table 4.7 with Table 4.8 or with 4.9.

Table 4.7 - Time-averaged C calculation for Re = 500 and St = 200.

Sample	Mean	Diference [(Mean n)-(Mean n-1)]	Sample Elements Number
1	111,3799	0	100
2	108,8019	2,5779984	200
3	107,2844	1,517546944	300
4	106,8212	0,463109842	400
5	106,4224	0,398858552	500

Table 4.8 - Time-averaged C calculation for Re = 500 and St = 400.

Sample	Mean	Diference [(Mean n)-(Mean n-1)]	Sample Elements Number
1	116,5822	0	100
2	113,6644	2,91785323	200
3	111,8004	1,864018526	300
4	111,9654	0,165002561	400
5	111,8736	0,091710182	500

Table 4.9 - Time-averaged C calculation for Re = 500 and St = 800.

Sample	Mean	Diference [(Mean n)-(Mean n-1)]	Sample Elements Number
1	142,404	0	100
2	133,2791	9,124967502	200
3	130,8444	2,434634052	300
4	128,2789	2,565539855	400
5	127,5185	0,760344581	500

Table 4.10 - Time-averaged C calculation for Re = 500 and St = 1 200.

Sample	Mean	Diference [(Mean n)-(Mean n-1)]	Sample Elements Number
1	147,8812	0	100
2	137,7334	10,14779038	200
3	134,3944	3,338988289	300
4	133,7038	0,690647897	400
5	132,2512	1,452574916	500
6	131,957	0,294171099	600

Table 4.11 - Time-averaged C calculation for Re = 500 and St = 1 600.

Sample	Mean	Diference [(Mean n)-(Mean n-1)]	Sample Elements Number
1	159,4583	0	100
2	143,3575	16,10085565	200
3	139,7232	3,634238945	300
4	138,7546	0,968632967	400
5	137,2973	1,457287454	500
6	136,6472	0,650109417	600
7	135,8407	0,806489629	700

4.2.1.3 C Averaging for Re = 1 000

It is possible to verify the time averaging procedure by observing Tables 4.12 to 4.15. For this specific Reynolds Number, the configuration with the Stokes Number equal to 200 again presented high divergence on the calculation and, therefore, is not considered in the present study. The Stokes Number influences the transient behavior of C value analyzed. The results verified in Tables 4.12 to 4.15 show that for all the Stokes Numbers studied, the difference between consecutive time-averaged C values is below the unity, as required. Verifying Tables 4.12 to 4.15 it is possible observe a different behavior when increasing the Stokes Number. Increasing the St from St = 400 (Table 4.12) to St = 800 (Table 4.13) the C reduces. Then, the C value increases when increasing the St from 800 (Table 4.13) to 1 200 (Table 4.14).

The C reduces again when increasing Stokes Number from 1 200 (Table 4.14) to Stokes Number equals to 1 600 (Table 4.15). This behavior differs from those found for Reynolds Number equal to 250 and Reynolds Number equal to 500 when for all Stokes Number tested, increasing the St implied in a C value increase. It is possible to validate, comparing Tables 4.12 to 4.15, that high Reynolds Number implies in a uncertain pattern for the C value, which indicates that the operation regime with Re above 500 is not an optimal choice.

Table 4.12 - Time-averaged C calculation for Re = 1 000 and St = 400.

Sample	**Mean**	**Diference [(Mean n)-(Mean n-1)]**	**Sample Elements Number**
1	128,9831	0	100
2	127,2843	1,698853973	200
3	126,7202	0,564105154	300
4	125,9121	0,808061635	400
5	125,3869	0,525169559	500
6	125,0529	0,334061623	600
7	125,0478	0,005079713	700

Table 4.13 - Time-averaged C calculation for Re = 1 000 and St = 800.

Sample	**Mean**	**Diference [(Mean n)-(Mean n-1)]**	**Sample Elements Number**
1	122,4907	0	100
2	119,6492	2,841546461	200
3	119,0631	0,586064953	300
4	118,7547	0,308417151	400
5	118,4777	0,276938536	500
6	118,6592	0,181455411	600
7	118,4257	0,23350599	700

Table 4.14 - Time-averaged C calculation for Re = 1 000 and St = 1 200.

Sample	**Mean**	**Diference [(Mean n)-(Mean n-1)]**	**Sample Elements Number**
1	127,4211	0	100
2	123,4351	3,986002631	200
3	121,6188	1,816309956	300
4	121,0596	0,559229811	400
5	121,0319	0,02774381	500
6	120,8982	0,133610157	600
7	120,6155	0,282727817	700

Table 4.15 - Time-averaged C calculation for Re = 1 000 and St = 1 600.

Sample	Mean	Diference [(Mean n)-(Mean n-1)]	Sample Elements Number
1	127,663	0	100
2	121,3118	6,35115508	200
3	119,3197	1,992063846	300
4	117,8698	1,449919387	400
5	117,2618	0,608065914	500
6	116,7578	0,503949229	600
7	116,258	0,499798831	700

4.2.1.4 C Averaging for Re = 1 250

It is possible to verify the time averaging procedure by observing Tables 4.16 to 4.19. The sample elements number indicates the number of elements used for the average calculation. Then time-averaged C and the difference between consecutive time-averaged C values are calculated. Once the value is below the unity, the respective time-averaged C value is used. Similar to the case for Reynolds Number equal to 1 000, the configuration with the Stokes Number equal to 200 presented high divergence on the calculation and, therefore, is not considered in the present study. The Stokes Number influences the transient behavior of C value analyzed. The results verified in 4.16 to 4.19 show that for all the Stokes Numbers studied, the difference between consecutive time-averaged C is below the unity, as required. It is possible to examine likewise that for the different Stokes Numbers, the sample size needed to perform the time average procedure is different. Verifying Tables 4.16 to 4.19 it is possible observe again a different behavior, with no clear pattern between Stokes Number and C. Increasing the Stokes Number from St = 400 (Table 4.16) to St = 800 (Table 4.17) the C value reduces.

Table 4.16 - Time-averaged C calculation for Re = 1 250 and St = 400.

Sample	Mean	Diference [(Mean n)-(Mean n-1)]	Sample Elements Number
1	105,7557	0	100
2	103,1594	2,596363958	200
3	102,681	0,478379081	300
4	102,5305	0,150449633	400
5	102,1187	0,411873055	500
6	101,9548	0,163838864	600
7	101,8787	0,076067657	700

When increasing the St from 800 (Table 4.17) to 1 200 (Table 4.18) the C value increases and remains stable when increasing Stokes Number from 1 200 (Table 4.18) to 1 600 (Table 4.19). Unlike all other Reynolds Numbers, there seems to be no link between Stokes Number and C for this Re = 1 250

Table 4.17 - Time-averaged C calculation for Re = 1 250 and St = 800.

Sample	Mean	Diference [(Mean n)-(Mean n-1)]	Sample Elements Number
1	97,25412	0	100
2	92,74283	4,511288616	200
3	91,1816	1,561234163	300
4	90,49972	0,68187965	400
5	90,41263	0,087085708	500
6	90,35417	0,058461331	600
7	90,32625	0,027925193	700

Table 4.18 - Time-averaged C calculation for Re = 1 250 and St = 1 000.

Sample	Mean	Diference [(Mean n)-(Mean n-1)]	Sample Elements Number
1	111,6711	0	100
2	106,5464	5,124623538	200
3	104,5441	2,002341524	300
4	103,9946	0,549505406	400
5	103,1464	0,848174638	500
6	102,9827	0,163693336	600
7	102,701	0,281734033	700

Table 4.19 - Time-averaged C calculation for Re = 1 250 and St = 1 600.

Sample	Mean	Diference [(Mean n)-(Mean n-1)]	Sample Elements Number
1	104,0914	0	100
2	102,8013	1,290110997	200
3	102,5959	0,205392362	300
4	101,9374	0,658552951	400
5	102,0403	0,102953589	500
6	102,0506	0,010259303	600

The results presented from the Table 4.12 to Table 4.19 show the already verified transient behavior of this multiphase flow. It was also investigated the difference below the unity for all tested cases, ensuring that the data had statistical significance. Comparing all the results, it is evident that for low Reynolds Number, the increase in the Stokes Number increases C. For higher Reynolds Number, this behavior is not apparent. The particle tracking visualization can help to understand this better. It is presented in the following section.

4.2.2 C Graphs and Particle Tracking Visualization

The results will be presented here for different St Numbers, including the C Variation as a function of the Re Number and the respective particle tracking Figures. Hence, it is possible to validate the previously supposed hypothesis about the influence of the Reynolds Number on C.

4.2.2.1 Particle Behavior for St = 200

For this specific case it was possible just to run two cases, Re = 250 and Re = 500. For higher Re Number, the calculation diverged and had high instability. For these two values of Re, the C as function of the Re Number is presented in the Figure 4.4. It is shown in Figure 4.4 that the increase in the Reynolds Number leads to a reduction in C value. However, the low number of tested configurations (only two) require more data analysis. The particle tracking visualization allows a better understanding of the phenomena. This two case simulated are presented on the Figure 4.5.

Observing Figure 4.5, it is possible to view the overall deposition configuration for the St Number equal to 200. First, the gas flow for Figure 4.5a is less intense than the flow visualized in Figure 4.5b. This difference makes sense once the Re Number is bigger in Figure 4.5b. Considering the gas flow interaction with the particles due to the drag force, once the gas flow has a higher velocity, the influence of the flow over the particles is stronger.

Figure 4.4 - C vs. Re, for St = 200. The C reduces with the increase in Re.

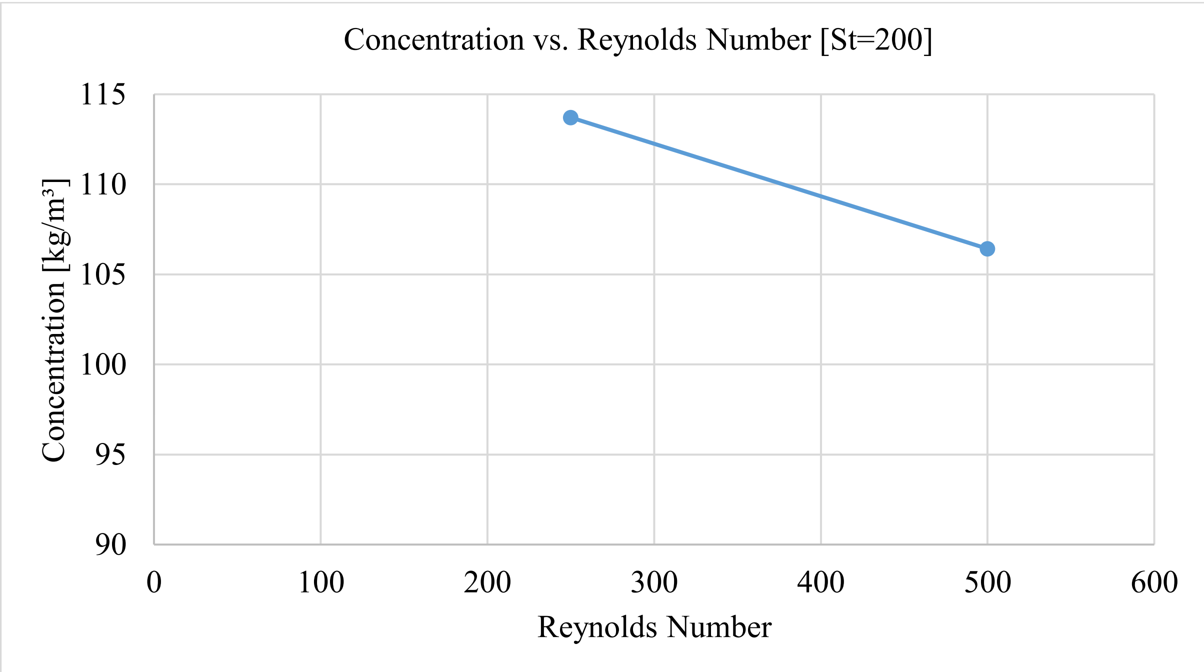

It is shown in Figure 4.6 the carrier channel. Visualizing how particles behave in this part of the geometry is a way to understand the deposition pattern near the plate. Comparing Figure 4.6a with Figure 4.6b, it is possible to conclude that the particles start to agglomerate slightly by increasing the Re Number. Particle agglomeration can be explained when the flow velocity is high enough to accumulate particles, transforming the spherical particle shape into another solid body, changing the drag force, and, consequently, the particle path. This behavior is more accentuated with higher Re as it will be examined for the higher Re presented further in the text.

Figure 4.5 - Particle tracking visualization, view 1, frontal view, St = 200, (a) Re = 250, (b) Re = 500.

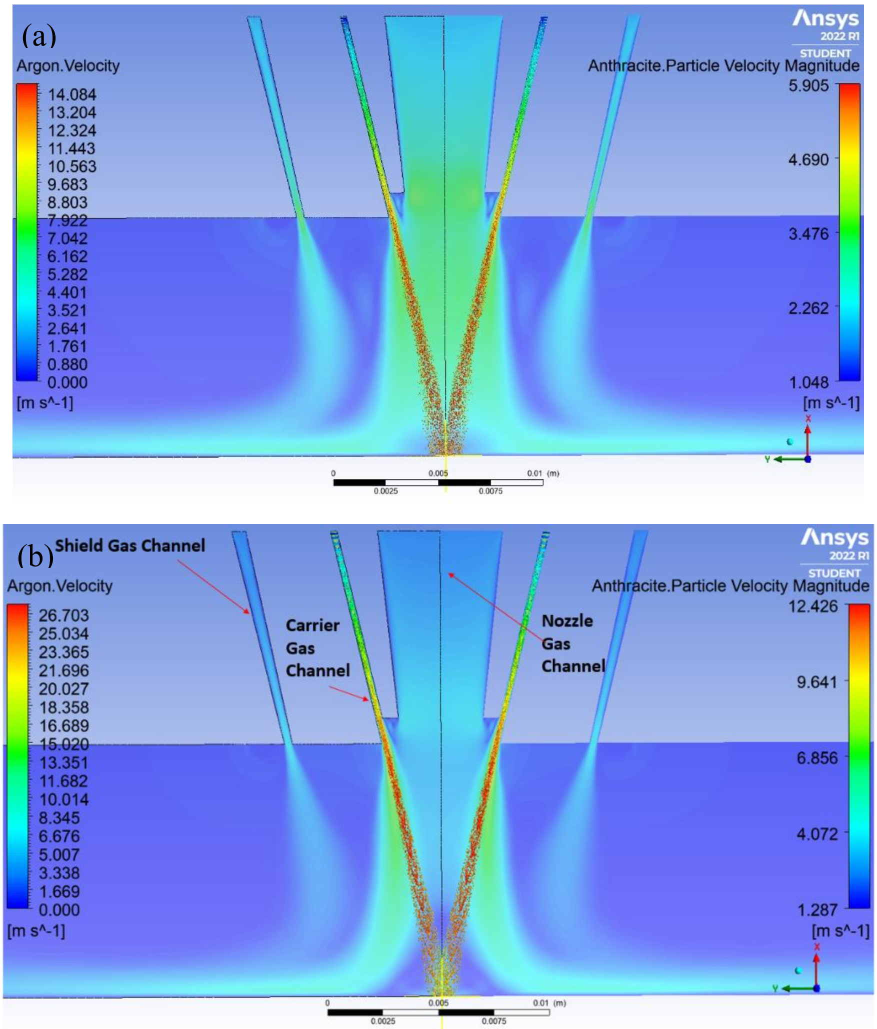

It is verified in Figure 4.7 the particle deposition pattern over the horizontal plate on the deposition area. It is possible to observe as well in Figure 4.7b that the deposition focus is smaller than the one in Figure 4.7a. It is verified in Figure 4.7 the particle tracking visualization in the deposition area.

Figure 4.6 - Particle tracking visualization, view 2, carrier channel, St = 200, (a) Re = 250, (b) Re = 500.

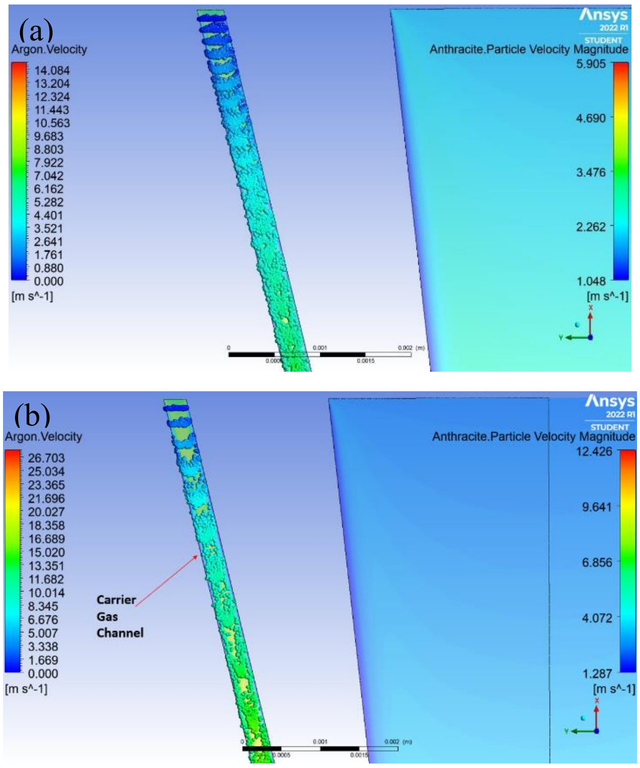

Figure 4.7 - Particle tracking visualization, view 3, deposition area, St = 200, (a) Re = 250, (b) Re = 500.

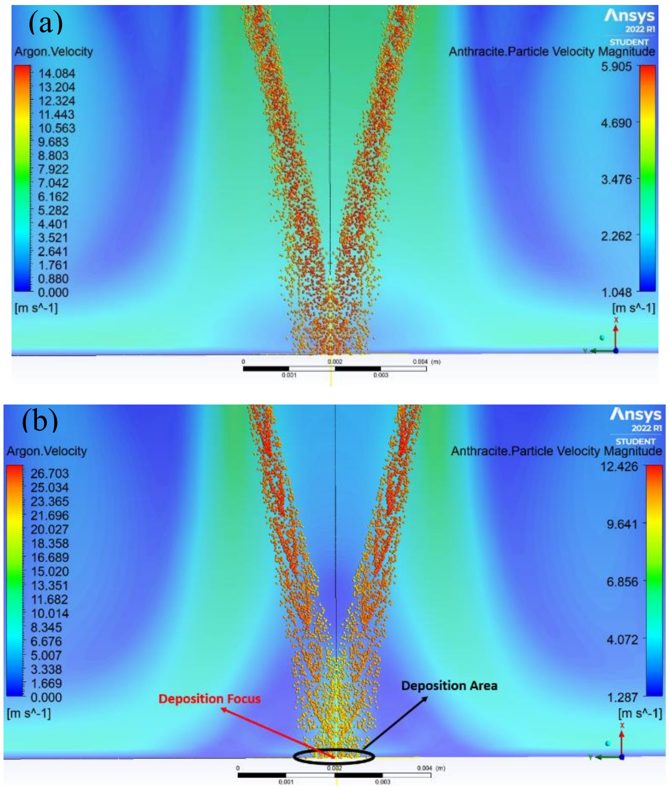

4.2.2.2 Particle Behavior for St = 400

For this configuration it was tested four different Re (Re = 250, Re = 500, Re = 1 000 and Re = 1 250) considering the St Number equal to 400. It is observed in Figure 4.8 the C in function of the Re Number. It is confirmed in Figure 4.8 that up to Re Number equal 500, the behavior still the same described for St Number similar to 200, with C increasing with the decrease of the Re Number. However, this pattern does not follow an apparent behavior for higher Re Number (Re = 1 000 and Re = 1 250). For Re Number equal to 1 000, C increase, and in sequence, for Re Number equal to 1 250, it decreases again.The particle visualization helps the better understanding of this complex behavior indicated in Fiugre 4.8.

It is shown in Figure 4.9 the particle tracking visualization considering the overall view. Observing Figure 4.9, it is possible to inspect the overall gas flow pattern for the different Re Number configurations. The gas velocity in the carrier channel increases with the increase in the Re Number, which is expected. The increase in the Reynolds Number also increases the influence on the particle pattern due to the higher drag force effect. The clustering formation (agglomeration effect) is confirmed again for the higher Re Number.

It is represented in Figure 4.10 a closer view at the carrier channel for the four Re tested. Comparing Figures 4.10a, 4.10b, 4.10c, and 4.10d, it is possible to observe that the particles start to agglomerate by increasing the Reynolds Number. Analyzing the Reynolds Number equal to 1 000 and Reynolds Number similar to 1 250, it is possible to observe a strong agglomeration still in the first part of the carrier channel. The influence of the flow Reynolds Number on the clustering formation is visible. The solid shape built for the higher Reynolds Number indicates that this type of flow differs from the conventional gas-particle flow. This agglomeration pattern can better explain C anomalous behavior for high Re, as shown in Figure 4.8.

Comparing Figures 4.11a, 4.11b, 4.11c and 4.11d it is possible tDa mesma formao verify that increasing the Re the agglomeration phenomena appears again near the deposition point. Figure 4.11d, with Re = 1 250, presents huge clustering with the formation of a new solid body that changes the interaction with the fluid flow. However, for 4.11c, Re = 1 000, the clustering effect is lower, and the deposition focus appears to be the most concentrated. For higher Re, both particle movement and C have no recognizable pattern. For the lowest Re (Re = 250, Figure 4.11a), the configuration has the higher C. It is also possible to observe a more homogenous deposition pattern for the case presented in Figures 4.11a and 4.11b. Therefore, these two Re Numbers can be set as a usable configuration for a higher C deposition configuration. Comparing the results found in Figure 7.11a and Figure 7.11b with the results presented in Figure 1.6, developed by Ferreira *et al.* (2020), it is possible to observe a particle behavior similar to the one presented by the Nozzle C, with a more closed deposition area.

Figure 4.8 - C vs. Re, for St = 400. There is a non usual pattern between Re = 500 and Re = 1000, with the C increasing with the increase of the Re.

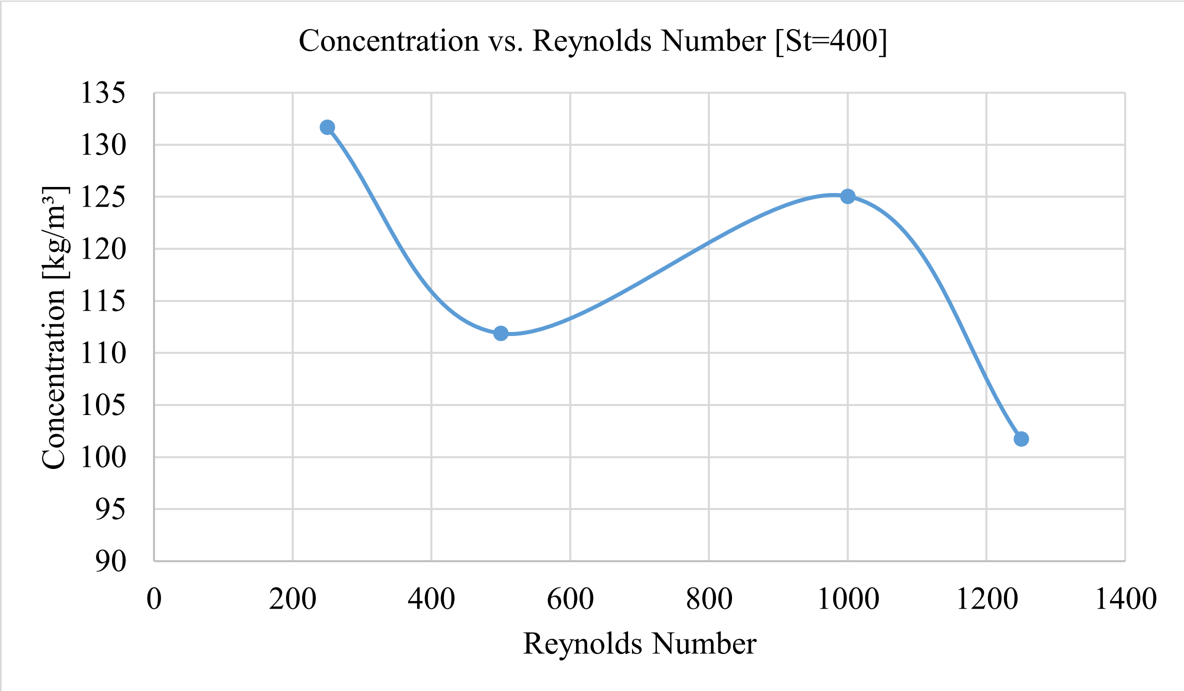

4.2.2.3 Particle Behavior for St = 800

For this configuration it was tested four different Re (Re = 250, Re = 500, Re = 1 000 and Re = 1 250) considering the St Number equal to 800. It can be observed in Figure 4.12 the C as a function of the Re. It is possible to presume in Figure 4.12 C value reducing with the Re increase. However, there is almost a plateau between Re = 500 and Re = 1 000, and the C value for Re = 1 000 is slightly lower than the C value for Re = 500. For Re = 1 250, the C value starts again to reduce.

Observing Figure 4.13, it is possible to vindicate the fluid flow velocity increasing again with the increase of Re. The shield gas fluid flow is almost irrelevant for Re = 1 000 and Re = 1 250, Figures 4.13c and 4.13d respectively, indicating the predominance of the carrier gas fluid flow. This higher effect of the carrier gas flow implies particle agglomeration for higher Re again. However, for this St = 800, the result seems less prominent than for the lower Re presented. A closer look at the carrier channel in Figure 4.14 can bring better insights into this particle agglomeration formation for Re = 800.

Figure 4.9 - Particle tracking visualization, view 1, frontal view, St = 400, (a) Re = 250, (b) Re = 500, (c) Re = 1 000, (d) Re = 1 250.

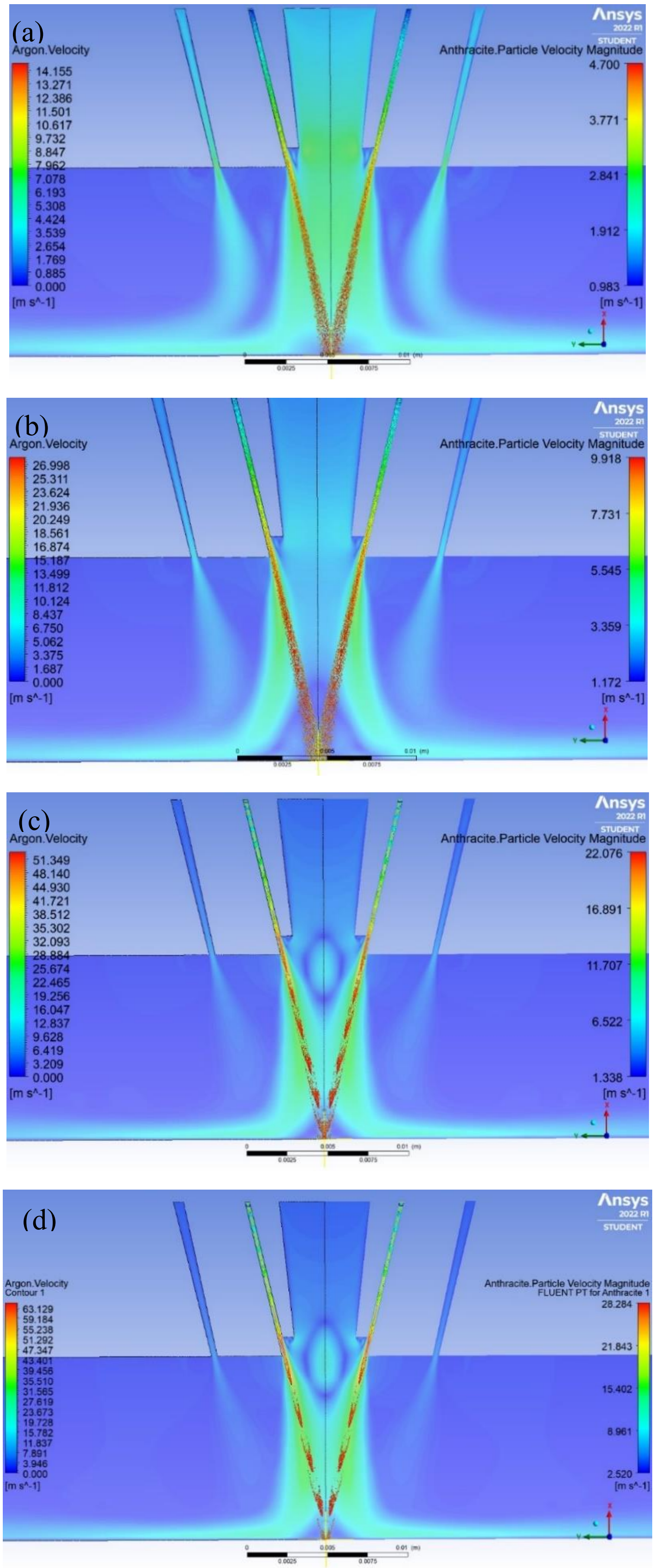

Figure 4.10 - Particle tracking visualization, view 2, carrier channel, St = 400, (a) Re = 250, (b) Re = 500, (c) Re = 1 000, (d) Re = 1 250.

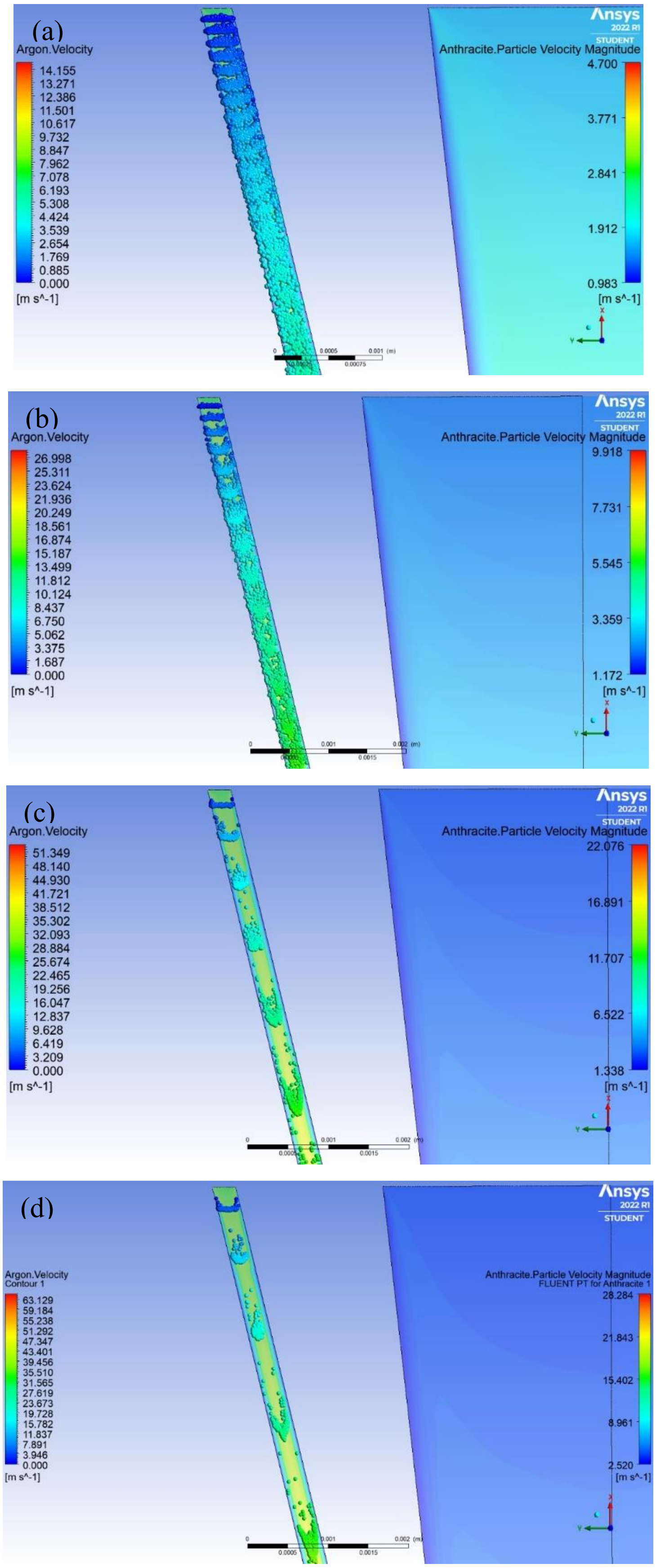

Figure 4.11 - Particle tracking visualization, view 3, deposition area, St = 400, (a) Re = 250, (b) Re = 500, (c) Re = 1 000, (d) Re = 1 250.

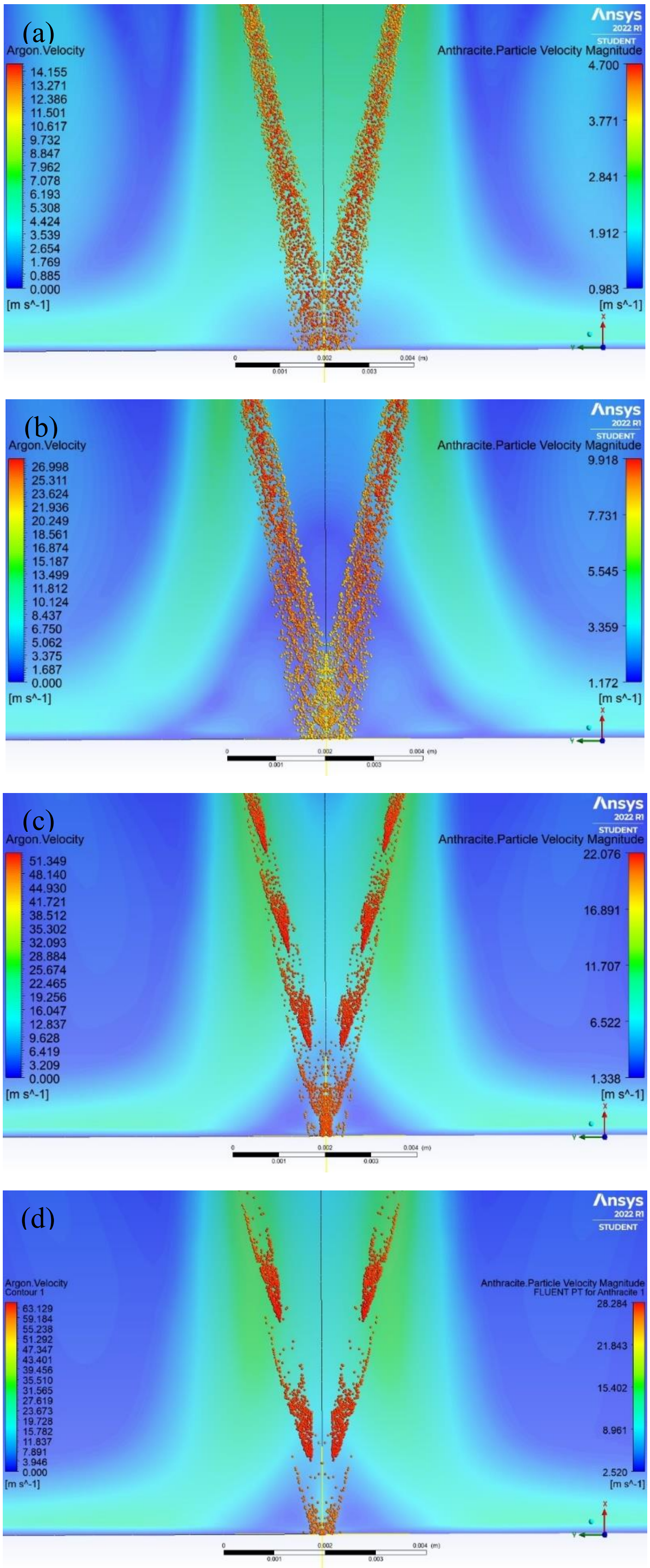

Observing Figure 4.14 showing the carrier channels for the four different Re, it is possible to corroborate the agglomeration pattern for the higher Re. However, comparing to Figure 4.10, the agglomeration for St = 800 is less noticeable. With a higher St Number, the particles are less influenced by the fluid flow and will not be dragged easily to form big piles like the ones in Figure 4.10. It can be demonstrated in Figure 4.15 the deposition area for the four different Re, considering St = 800.

Figure 4.12 - C vs. Re, for St = 800. The particle C decreases continuously with the increase of the Re, with no abnormal behavior for intermediate Re.

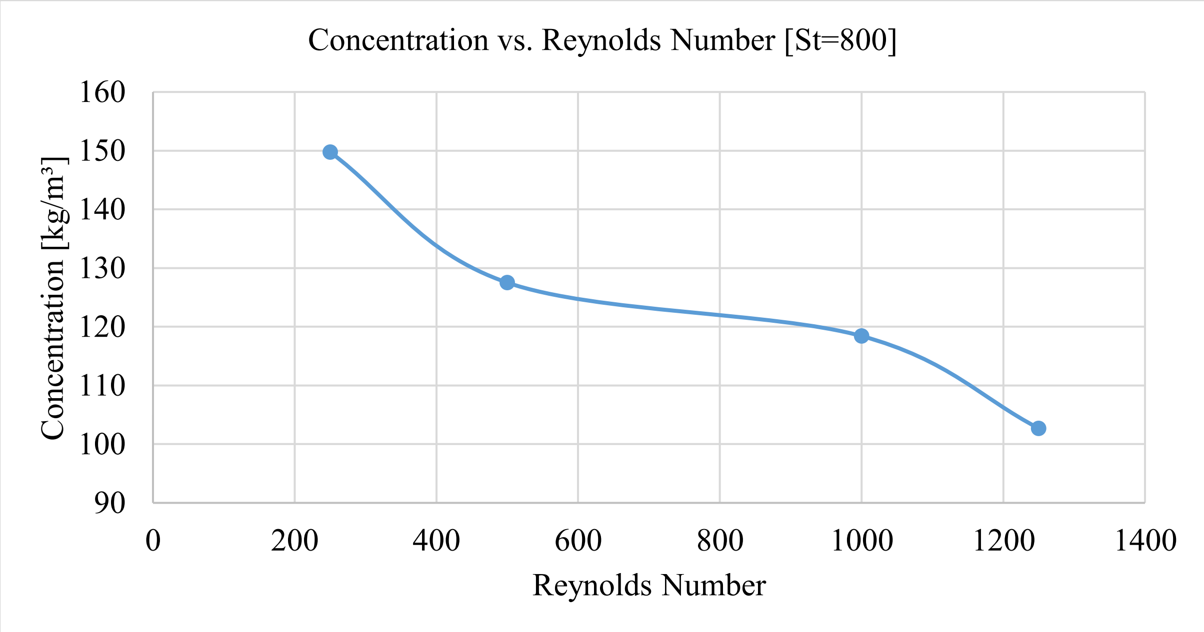

It is possible again to verify with Figure 4.15 the particle accumulation for higher Re. However, as mentioned in Figure 4.14, this agglomeration effect is less well-defined than the one verified for St = 400. The Re increase gradually reduces the focal area, as observed comparing Figures 4.15a, 4.15b, 4.15c and 4.15d. It is important notice that the increase in the Stokes Number makes the particles less susceptible to the fluid flow. Therefore, the agglomeration effect appears to be less evident as it is possible to observe when comparing Figure 4.14d with Figure 4.10.

Figure 4.13 - Particle tracking visualization, view 1, frontal view, deposition area, St = 800 (a) Re = 250, (b) Re = 500, (c) Re = 1 000, (d) Re = 1 250.

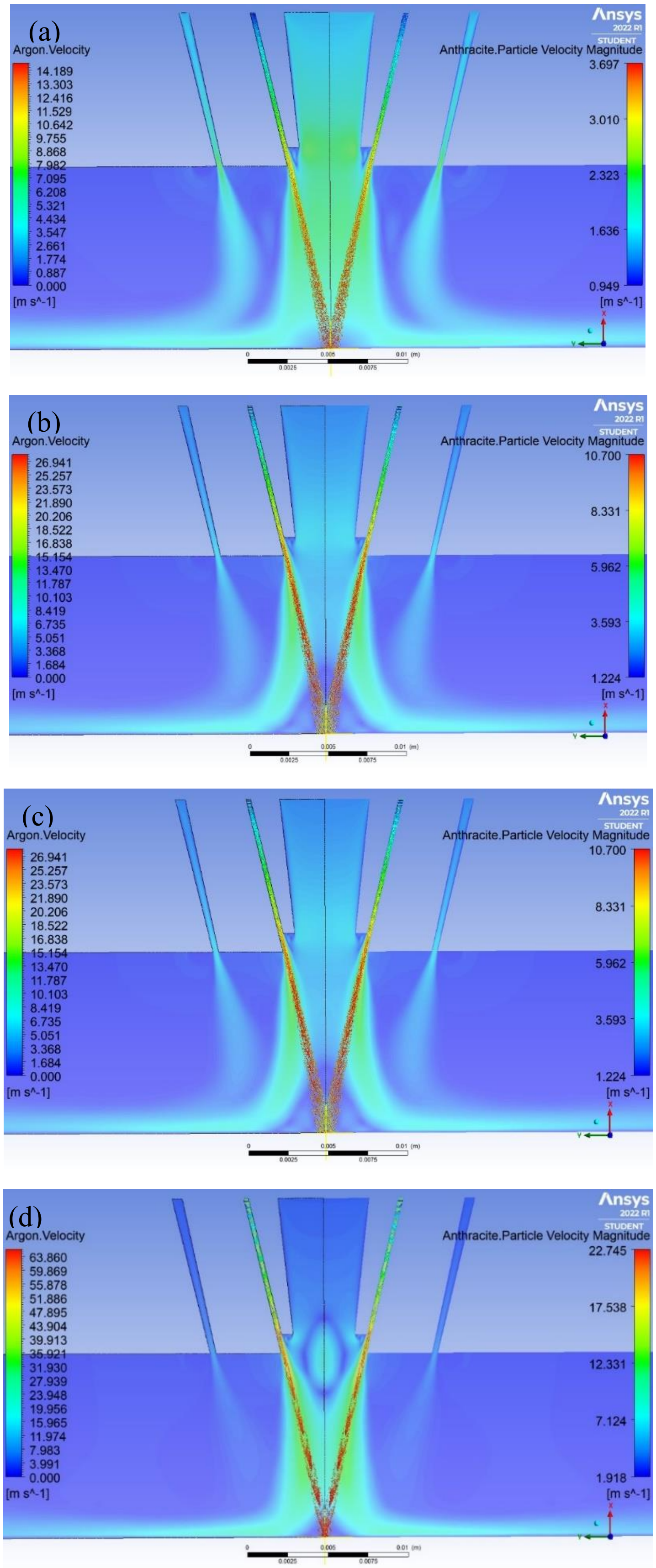

Figure 4.14 - Particle tracking visualization, view 2, carrier channel, St = 800 (a) Re = 250, (b) Re = 500, (c) Re = 1 000, (d) Re = 1 250.

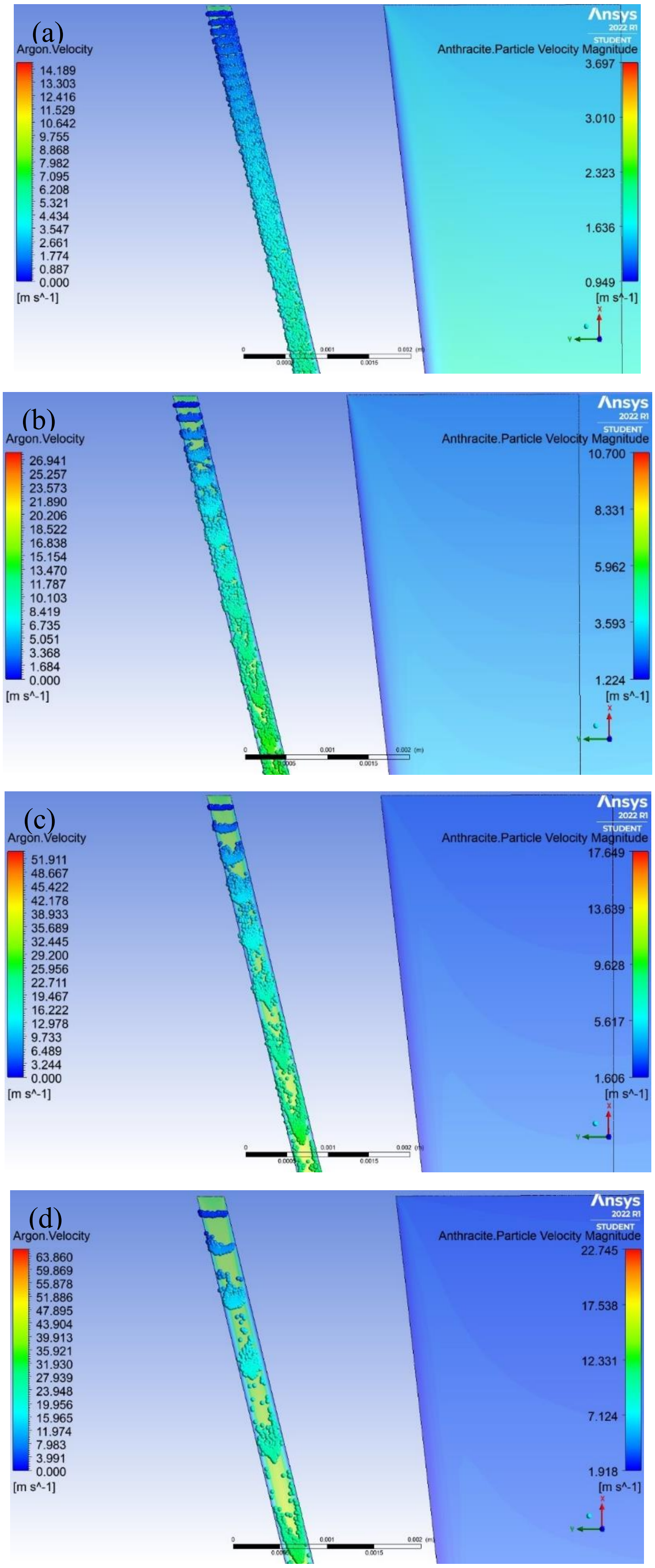

Figure 4.15 - Particle tracking visualization, view 3, deposition area, St = 800 (a) Re = 250, (b) Re = 500, (c) Re = 1 000, (d) Re = 1 250.

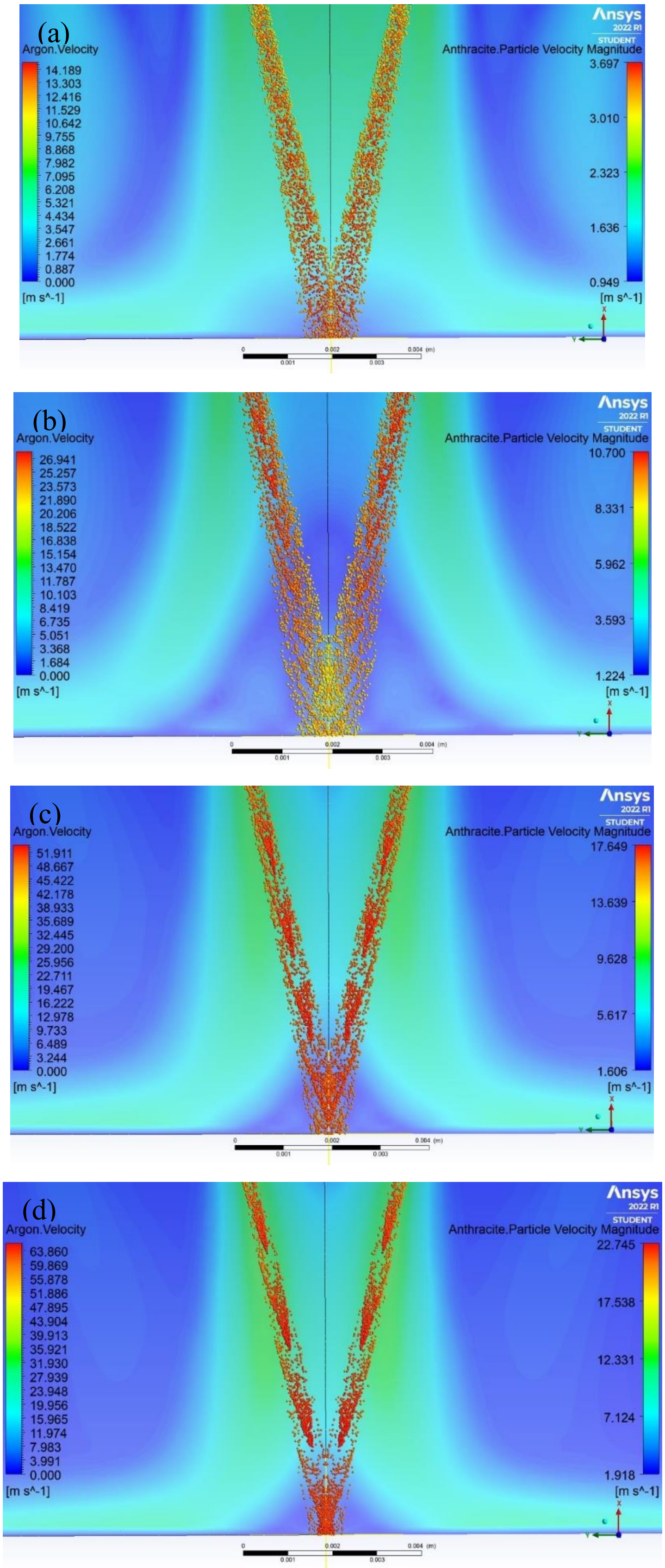

4.2.2.4 Particle Behavior for St = 1 200

For this configuration it was tested four different Re (Re = 250, Re = 500, Re = 1 000 and Re = 1 250) considering the St Number equal to 1 200. It is verified in Figure 4.16 the C as a function of the Re. It is presented in Figure 4.16 the same behavior verified in Figure 4.12, the C reduction with the increase in Re. The C values for Re = 500 and Re = 1 000 are similar. For Re = 1 250, the C value drops considerably. It is presented in Figure 4.17 the frontal view for the four different Re.

Figure 4.17 has a similar particle behavior compared to Figure 4.13, with a slightly particle solid formation for higher Re. However, the effect is even less significant when compared with the St = 400. It seems noticeable that the increase in St Number reduces the agglomeration effect. The focal point is, again, reduced by the increase in Re. The carrier channel is shown in Figure 4.18, where it is observable that even with the agglomeration for cases 4.18c and 4.18d, both cases represent a smaller clustering formation compared to the ones verified for St = 400 (Figure 4.10) and for St = 800 (Figure 4.14). Figure 4.19 represents the deposition area for St = 1 200.

The agglomeration formation in Figure 4.19 is less visible than for the other cases for St = 400 and St = 800. The deposition focus reduces with the increase in Re, having the smaller focal point in Figure 4.19d. The behavior established in the carrier channel shown in Figure 4.18 is amplified by the fluid flow and once the particles compose a single solid body it is transported up to the deposition area, as it is possible to verify in Figure 4.19.

Figure 4.16 - C vs. Re, for St = 1 200. The particle C decreases continuously with the increase of the Re.

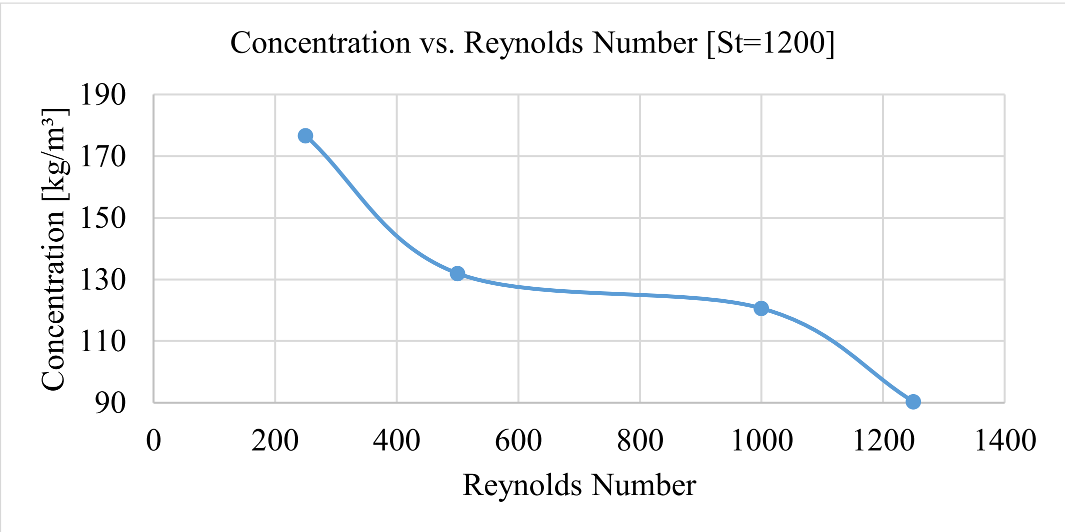

Figure 4.17 - Particle tracking visualization, view 1, frontal view, deposition area, St = 1 200 (a) Re = 250, (b) Re = 500, (c) Re = 1 000, (d) Re = 1 250.

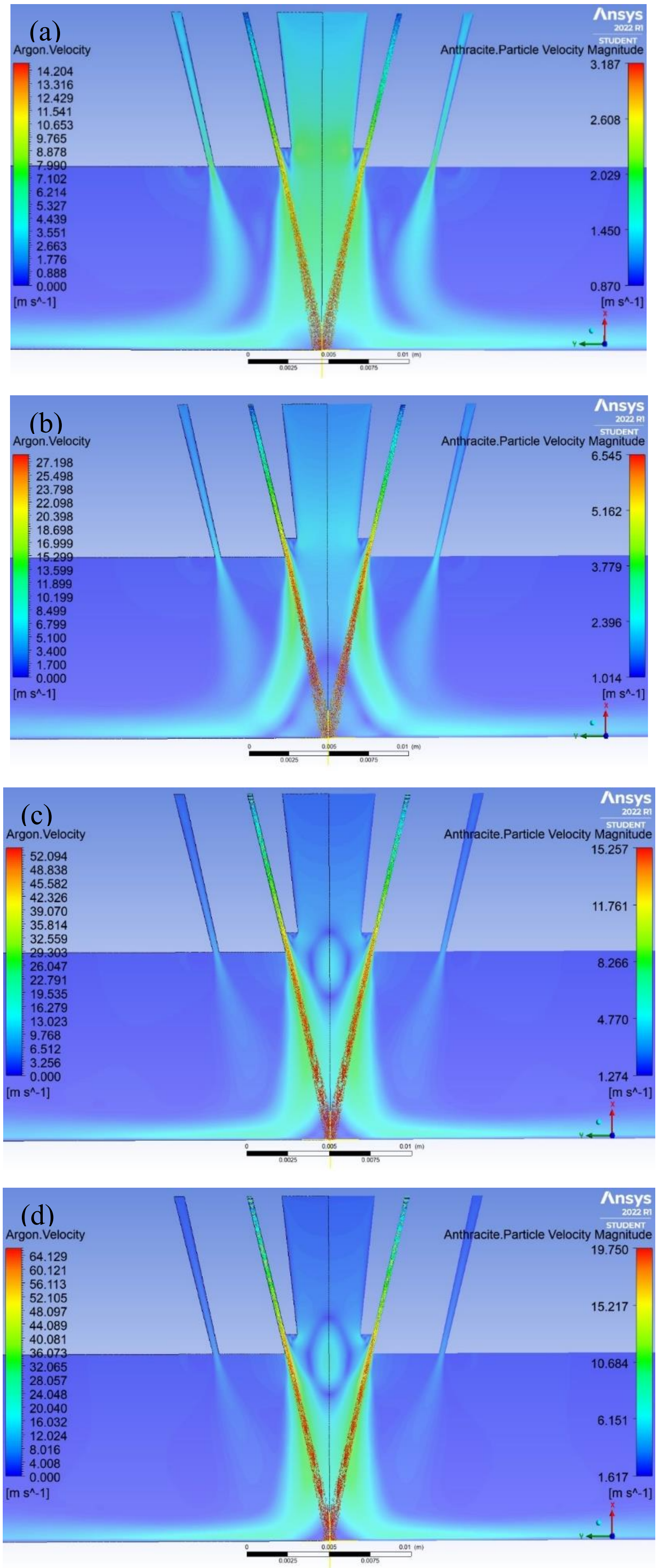

Figure 4.18 - Particle tracking visualization, view 2, frontal view, deposition area, St = 1 200 (a) Re = 250, (b) Re = 500, (c) Re = 1 000, (d) Re = 1 250.

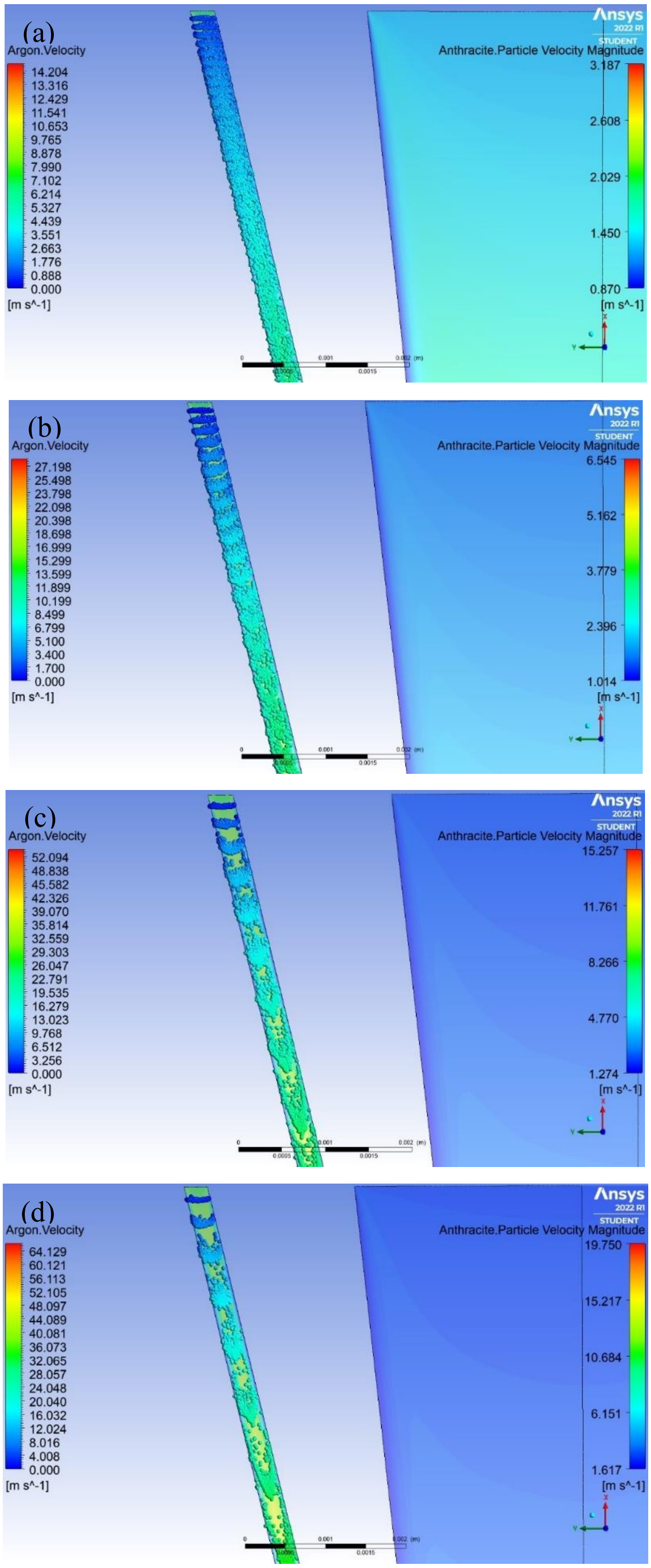

Figure 4.19 - Particle tracking visualization, view 3, frontal view, deposition area, St = 1 200 (a) Re = 250, (b) Re = 500, (c) Re = 1 000, (d) Re = 1 250.

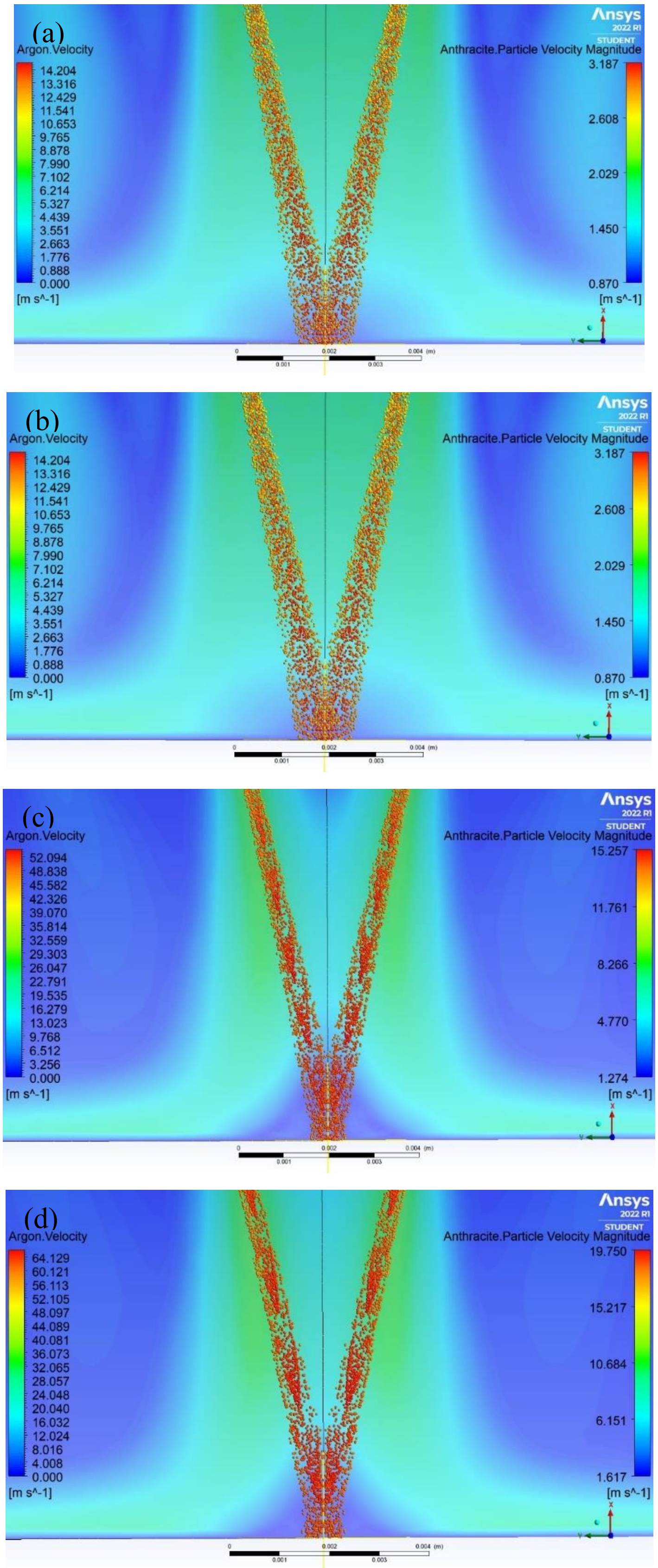

4.2.2.5 Particle Behavior for St = 1 600

For this configuration it was tested four different Re (Re = 250, Re = 500, Re = 1 000 and Re = 1 250) considering the St Number equal to 1 200. It is viewed in Figure 4.20 the C in function of the Re. Analyzing Figure 4.20, it is possible to verify a considerable discrepancy between the C value for Re = 250 and for the other Re values, explained by the combination of a low Re Number with a high St Number. The particles suffer a slight influence from the fluid compared with the other Re and St combinations. Further analyzing Figure 4.20 it is possible to conclude that increasing Re leads to a decrease in C, similar to the other St Number analyzed, with similar values for Re = 500 and Re = 1 000. The figure 4.21 gives an overall visualization of the particle movement for the four St Numbers cases.

For the configurations presented in Figures 4.21a, 4.21b, 4.21c and 4.21d the behavior is similar to the ones for the St = 400, St = 800 and St = 1 200. Increasing the Re, the particles tend to agglomerate. Still, for this St Number, this effect is even lower than for the other St Number. Increasing the St Number, the agglomeration effect is less explicit. It is shown in Figure 4.22 the carrier channel for the St = 1 600.

Figure 4.20 - C vs. Re, for St = 1 600. For the lowest Re, it is possible verify a strong C peak, indicating that for this specific configuration (highest St with smallest Re) the C reaches the highest value.

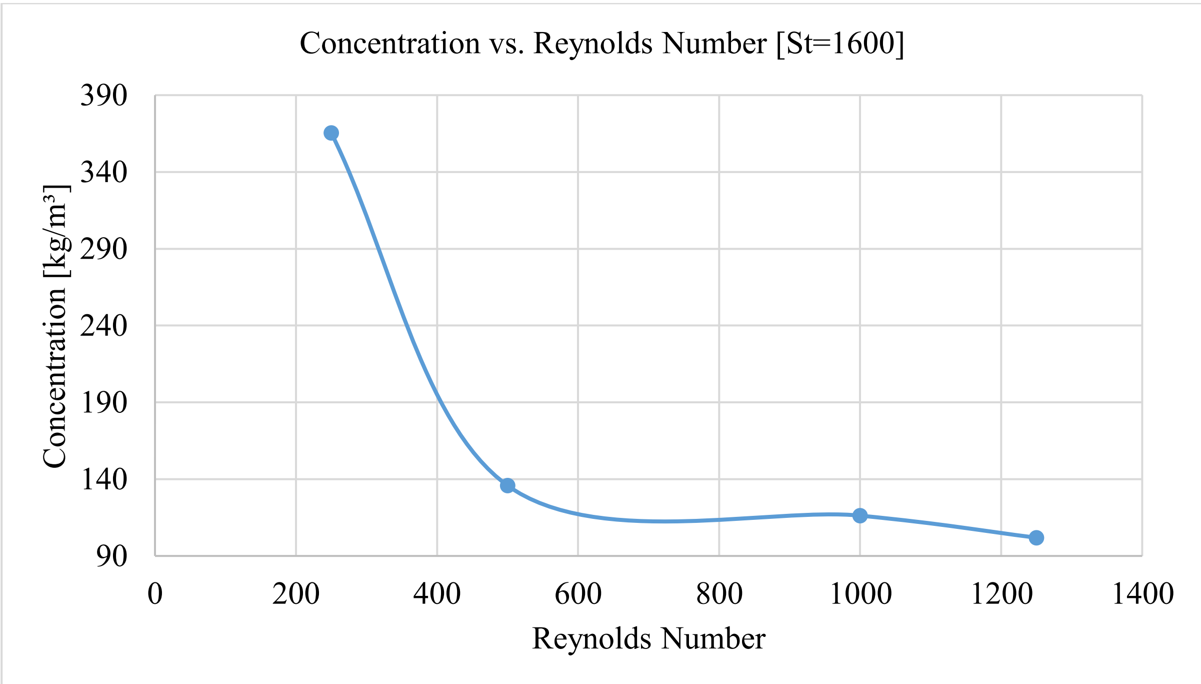

Figure 4.21 - Particle tracking visualization, view 1, frontal view, deposition area, St = 1 600 (a) Re = 250, (b) Re = 500, (c) Re = 1 000, (d) Re = 1 250.

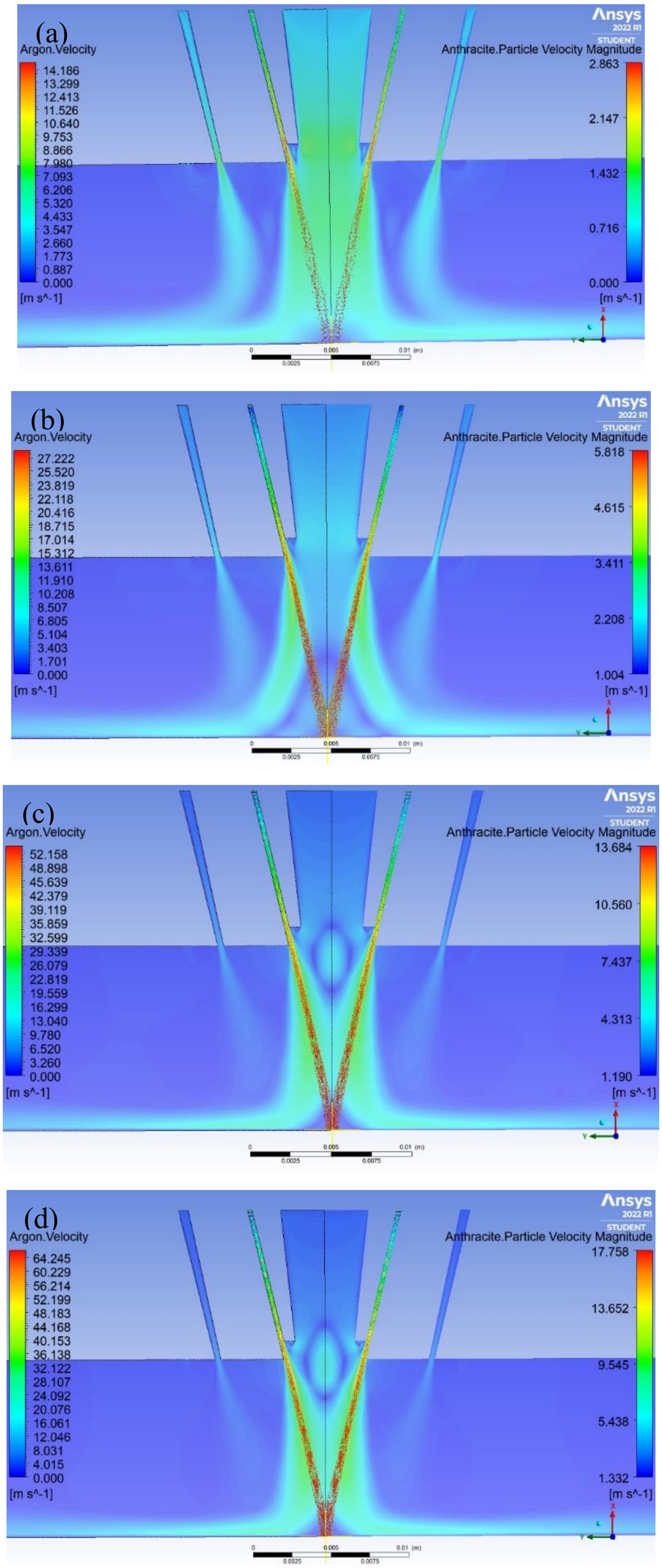

Figure 4.22 - Particle tracking visualization, view 2, frontal view, deposition area, St = 1 600 (a) Re = 250, (b) Re = 500, (c) Re = 1 000, (d) Re = 1 250.

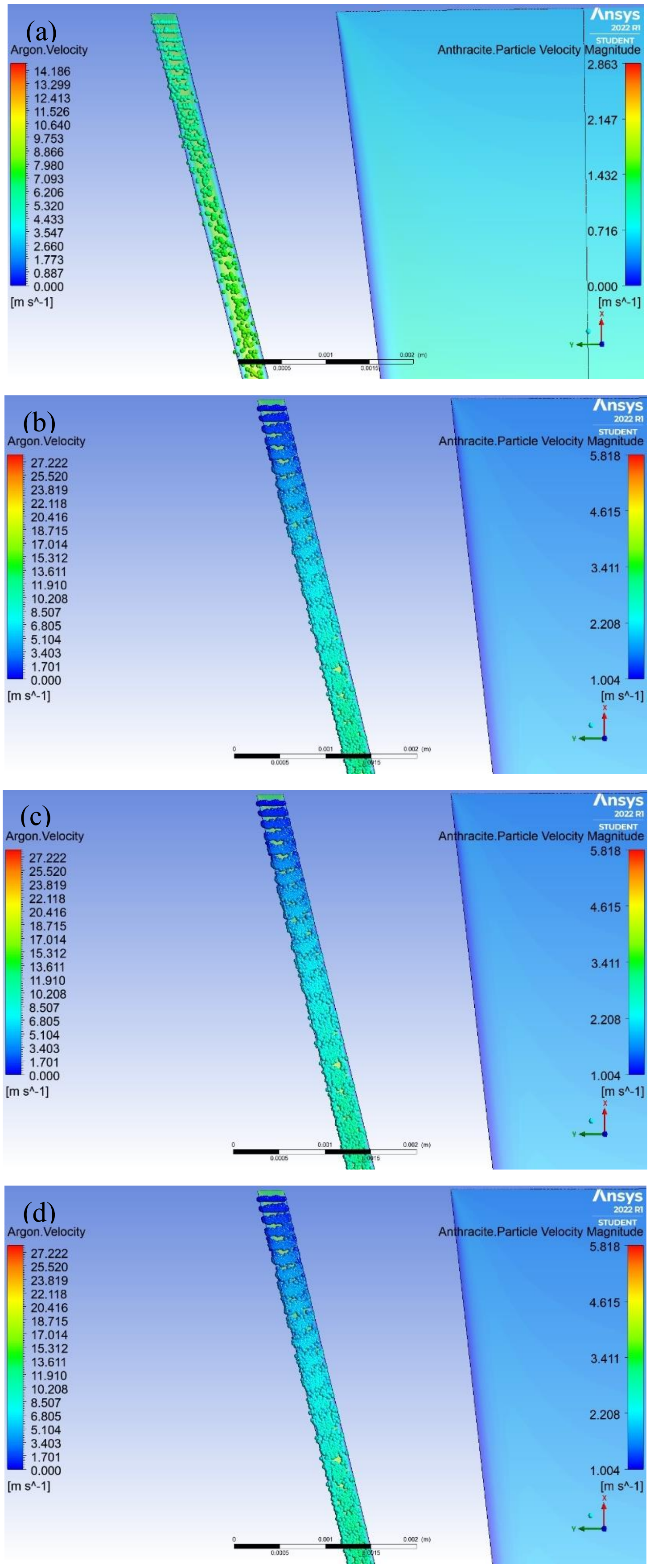

Figure 4.23 - Particle tracking visualization, view 3, frontal view, deposition area, St = 1 600 (a) Re = 250, (b) Re = 500, (c) Re = 1 000, (d) Re = 1 250.

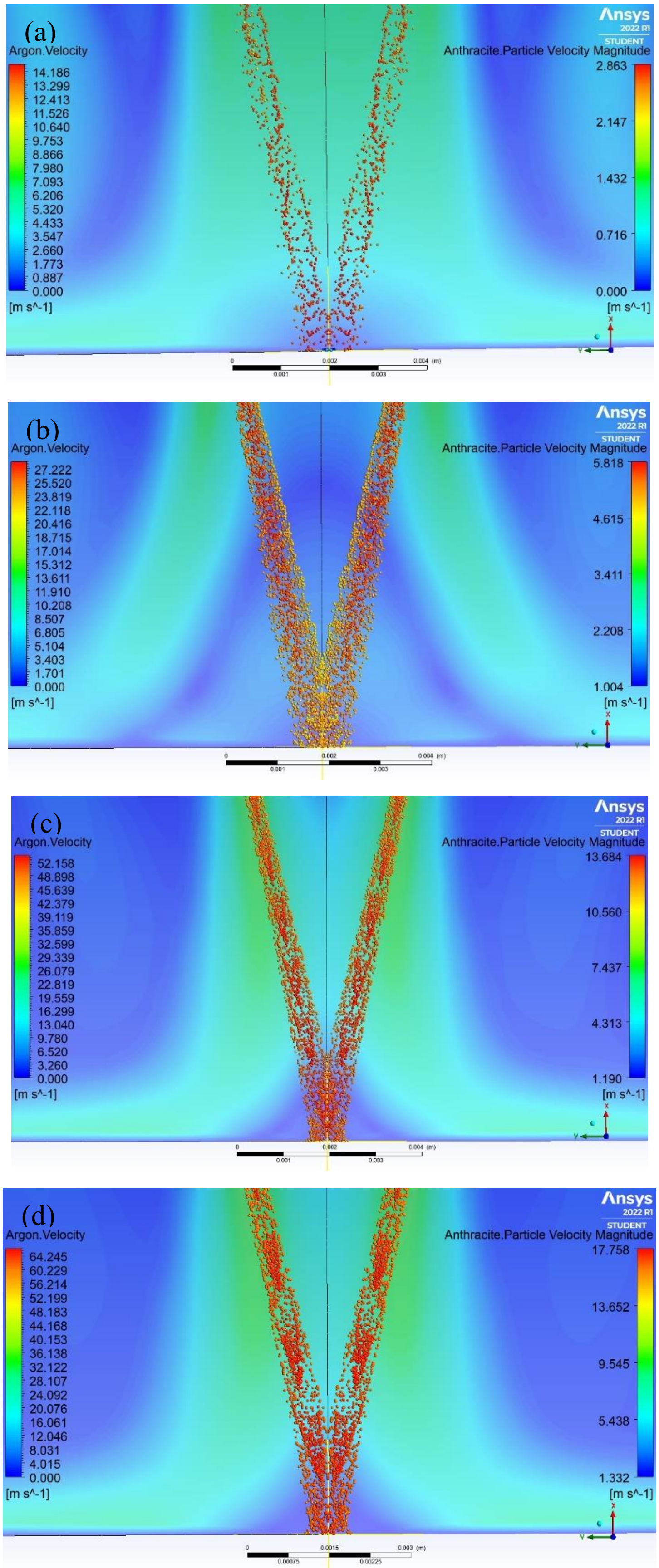

The lower Number of particles for Re = 250 is confirmed in the carrier channel visualization presented in Figure 4.22. For the other Re, it is possible to validate that, similar to the St = 400, St = 800, and St = 1 200, the particle aggregation appears for higher Re. However, the increase in St Number reduces the clustering effect. The deposition area for this St = 1 600 is presented in Figure 4.23.

Comparing Figures 4.23a, 4.23b, 4.23c and 4.23d, it is possible to observe the clustering formation, but in a lower intensity compared with the other St Numbers cases, as it is possible to view comparing Figure 4.23d with Figure 4.19d.

4.2.3 C Evolution in Function of the St Number

The C value in function of the St Number for Re = 250 is presented in Figure 4.24.

Figure 4.24 - C vs. St, for Re = 250. It is possible to verify the increase in the particle C with the increase in the Stokes Number, due to the fact that once the particles are less susceptible to the fluid flow, they reach directly the central point analyzed.

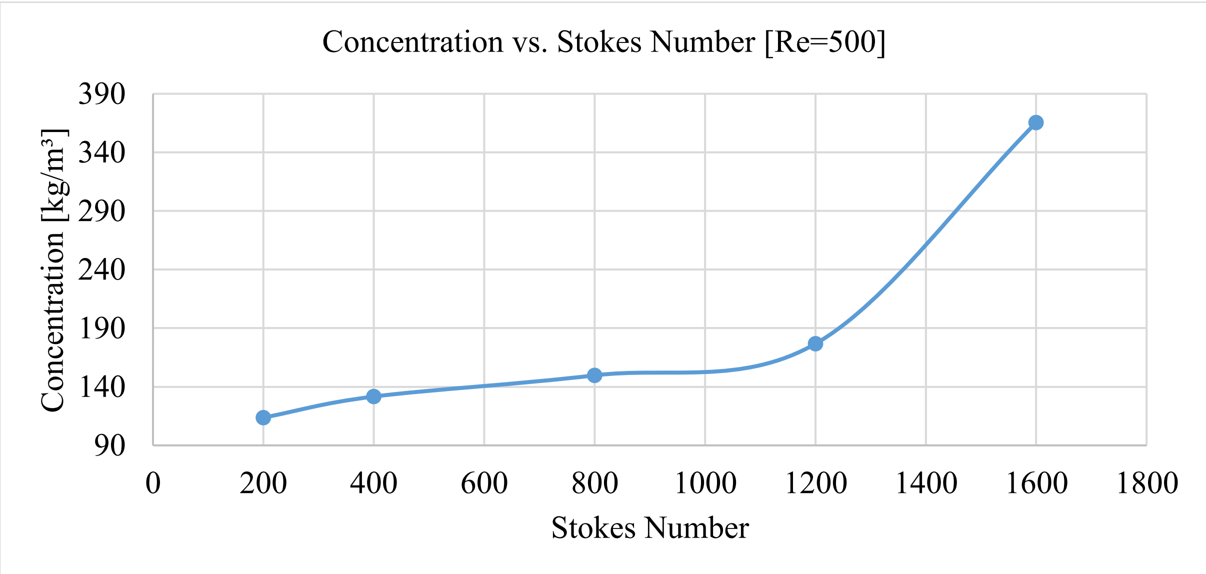

Observing Figure 4.24, it is possible to verify that by increasing the St Number, the C value rises. Re = 250and St = 1 600 have higher C than all other configurations, mainly due to the high density applied. The St Number seems to positively impact C, as it is possible to observe. The Figure 4.25 show the C in function of St Number Number, for Re = 500.

Observing Figure 4.25, it is possible to the same pattern: increasing the St Number, the C value rises, nevertheless with a lower rate, as it is possible to verify in Figure 4.24. The next two figures, Figure 4.26 represents the effect of St Number in C for higher Re (Re = 1 000).

Below Re = 1 000, there is an apparent C behavior, with C rising by the increase of the St Number. In the region above Re = 1 000, this pattern is lost for low St Number. It is observable the higher agglomeration pattern for the area with higher Re and low St Number.

Figure 4.25 - C vs. St, for Re = 500. It is possible to verify the increase in the particle C with the increase in the Stokes Number. However less accentuated than the behavior presented in Figure 4.24.

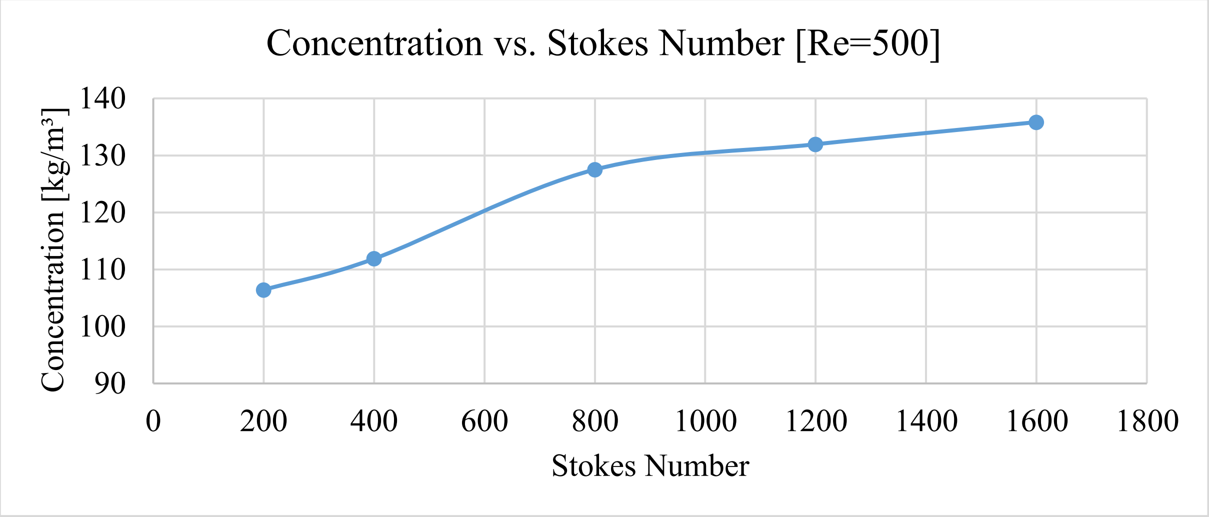

Figure 4.26 - C vs. St, for Re = 1 000. For this Reynolds Number there is no observable pattern considering the variation of the C as a function of the Stokes Number, mainly due the agglomeration of the particles.

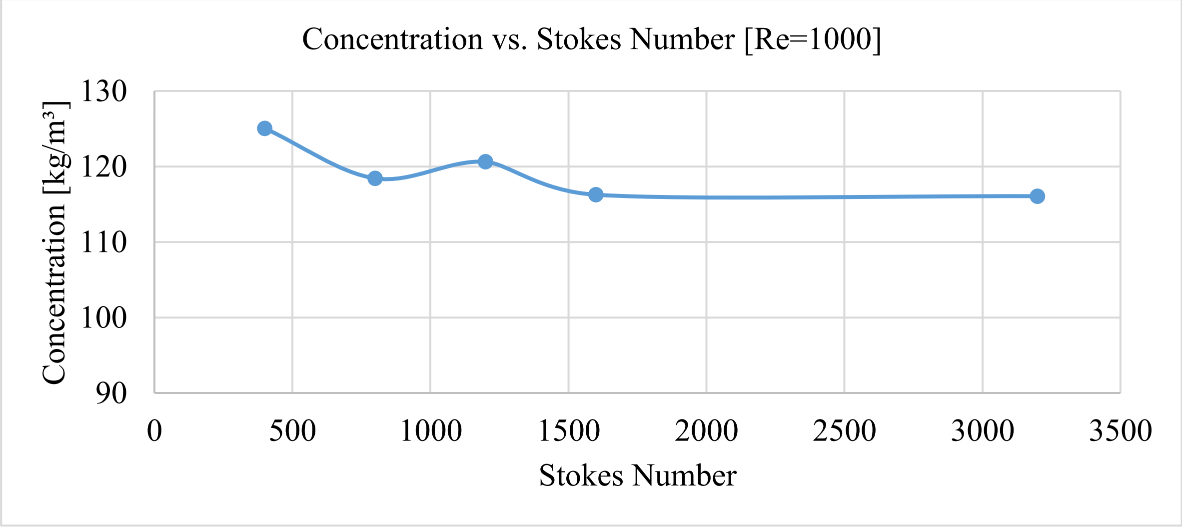

Then the C behavior starts to be not predictable. A way to compare different C values as a function of Re is by taking the C average as a function of the St Number. The C as a function of the St Number for Re = 1 250 is not presented in the current work because the values obtained show a significative discrepancy and do not bring any other inception about the problem. It can be verified in Table 7.20 the respective averaged values obtained for each Re.

Table 4.20 - C in function of Re. The increase in the Re culminates in a reduction in the particle C value.

Re	C – kg/m³
1 250	100,23
1 000	119,28
500	122,72
250	187,44

Analyzing the mean C values in the function of Re Number present in Table 4.20, it is possible to support that by decreasing the Re Number values, the C value rises. This rising is expected due to the reduction in Re Number, reducing the influence of the gas flow over the particles. Therefore, the particles are directed to the deposition area and increase the C value measured on the probe placed on the center point indicated in Figure 3.8.

4.2.4 Time Step Size Investigation

It is also important to confirm how the time step influences particle behavior and visualization. It is known that the reduction in time step size is costly considering the computational constraints to save all the needed data. However, for future work, it is important to proceed this analysis. The time step was reduced by a factor of 10, considering the time step took to generate the particle tracking visualization. That means that it was used δt = $10^{-4}$and for the comparison it was set up δt = 10^{-5}. The simulation configuration for this comparison is Re = 1 250 and St = 400. An overall visualization comparing both time steps is presented in Figure 4.27.

It is observable in Figure 4.27 that when the time step size is reduced, the particle agglomeration is small. The particle injection is a discrete procedure based on the time step. Reducing the time step size will increase the frequency of injection. And once the agglomeration effect occurs because of the particle relation with the fluid flow, the particles that are injected with a smaller time step avoids the agglomeration effect, and it will be closer to the actual case scenario of continuous injection. It is presented in Figure 4.28 takes a closer look at the carrier channel for both time steps. It is possible to substantiate in Figure 4.28, the significant difference between the particle behavior using a smaller time step. For Figure 4.28b, the multiphase gas-solid flow is continuous and is closer to the real injection case.

Figure 4.27 - Overall deposition area visualization comparing both timesteps. It is possible to verify the agglomeration effect reducing significantly with a time step smaller.

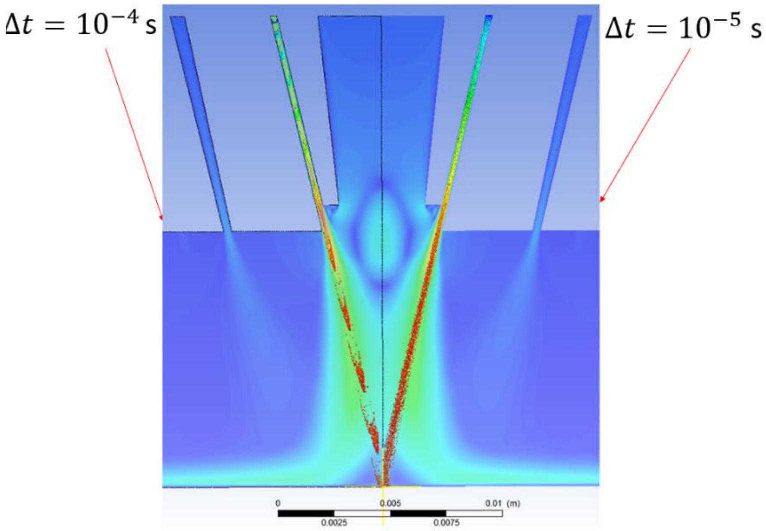

Figure 4.28 - Carrier channel visualization, (a) $\delta t = 10^{-4}$, (b) $\delta t = 10^{-5}$. Observing closer the carrier channel for both time steps, it is clear the agglomeration pattern with a bigger time step. Once using a smaller time step, the agglomeration basically disappears.

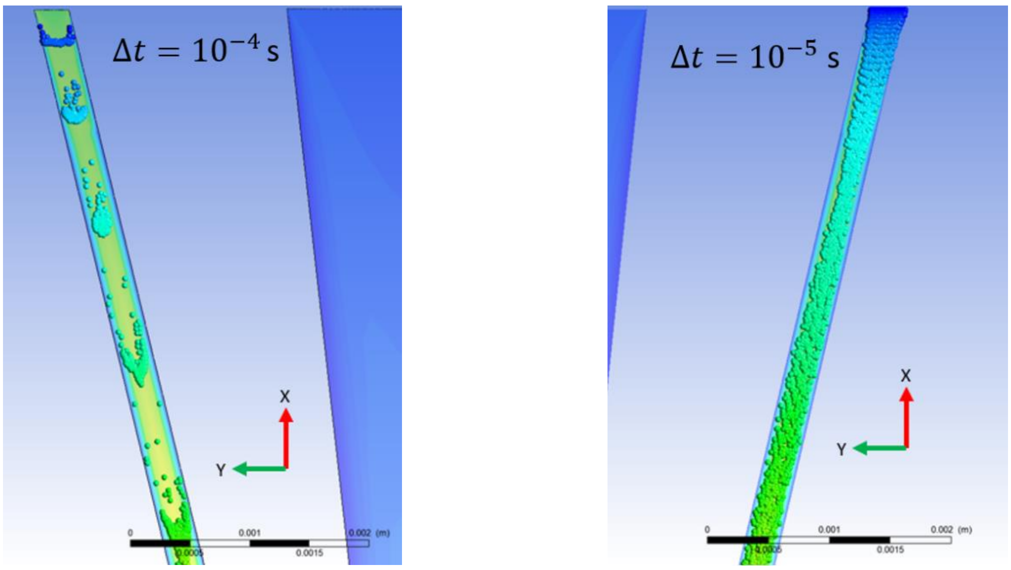

It is observed in Figure 4.29 the deposition area. It is essential to observe that all the simulations were performed with a time step equal to 10^{-4} , and the agglomeration effect was observed due to the use of this time step. In future works, simulations with smaller time steps will be performed to investigate the effect on the particle's behavior.

Figure 4.29 - Particle tracking visualization. It is possible to verify the deposition pattern difference for the different time steps used. Smaller the time step used, more homogeneous is the particle flux.

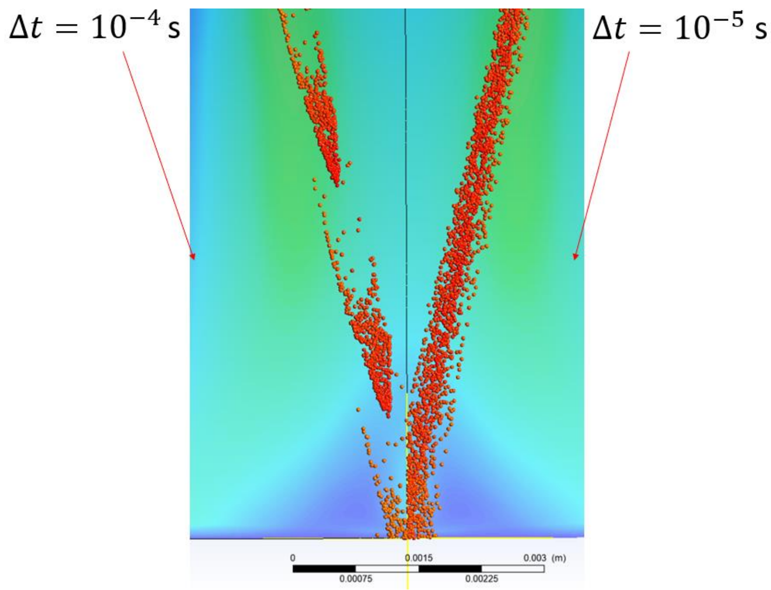

The knowledge obtained with this present work serves as a step toward new developments that were not possible in this current work. The use of smaller time steps to perform the simulation induces an injection frequency higher, which is closer to the real application scenario with a constant powder mass flux. The agglomeration effect occurs mainly due to the use of the higher time steps, inducing lower injection frequencies. Once the particle injection is not constant, this increases the agglomeration effect because the particles are dragged by the fluid flow and agglomerate. This agglomeration culminates into a solid body shape that changes the interaction due to the drag and other multiphase forces, changing the deposition pattern.

CHAPTER V

CONCLUSIONS

The conclusions obtained from the simulations are presented in this section with the main insights, the overall hypothesis tested, and finally, all the essential key points that came with the development of this work.

- The results presented show no variation for the velocities evaluated the for meshes with more than 100 000 cells, considering the results from probes 2 and 3. However, the velocity results presented by the probe indicates a inflection point that should be further investigated.
- With the selected mesh considering the results obtained from the procedure presented in this current work, it was possible to develop a 2D model with an axial symmetry allowing closer proximity to the results of the analysed material experiment. The system operates in a transient regime, with C variating over time. Therefore, C needed to be time-averaged. For this task, a time step sampling included all necessary values to ensure that the difference between the consecutive means, for all studied Re and St, is below one. It is verified that the Re and St values seem to impact how many samples are needed to guarantee the correct mean value. Therefore the St and Re values are directly linked to how the flow is more or less transient.
- It is seen from the results that considering low Re numbers (below 500), this behavior was obtained. For higher Re (Re = 1000 and Re = 1250), it was concluded that there is no pattern for the Particle Concentration. This happens mainly because increasing the Re will make the particle more susceptible to the fluid flow, and then they will not follow the fluid flow pattern, decreasing the Particle Concentration Value on the analyzed point.
- The leading cause behind this pattern loss is the agglomeration of the particles, which occurred for these high Re. This agglomeration changes the shape of the particles, building a new solid body with a new shape and changing the interaction with the fluid flow due to the drag force. This change modifies the particle deposition behavior.
- It is possible to check that for this high agglomeration formation, the focal area is reduced, which can lead to a reduction in particle volume need to perform a given material deposition process. Nevertheless, this should be further investigated in a future work.

- The experiments also showed a clear pattern for low Re, with the increasing of Re, decreasing the Particle Concentration. However, this pattern is lost for high Re again, mainly because of the clustering formation.
- After performing a Particle Concentration average as a function of the St Number it is clear that decreasing the Re will increase the Particle Concentration value. The increase in Re makes the particles more influenced by the fluid flow and less by gravity, bringing the axis crossing point up, and changing the deposition area in the horizontal plate. The higher the Re, the lower the deposition area and the higher the deposition focus.

According to the current study, the gas-particle regime indicated for a deposition machine application is to operate with low Re(below 500) and bigger St. This study presented the presence of clustering for these specific cases, mainly due to the time step used. The clustering presence is another attention point and can be eventually discussed better by analyzing the results. It is possible to check that the particle cluster is reducing the focal point area, which can be better for deposition precision. However, this should be better investigated.

CHAPTER VI

FUTURE WORK AND PERSPECTIVES

Some points still need to be clarified. However, the knowledge brought by the experiments performed here was of great value for all researchers involved and will allow the continuation of the research with new and important perspectives.

- It is demonstrated that it is necessary to reduce the time step size. Considering the study time restriction and computer storage capacity for this current dissertation work, the use of smaller time steps was necessary to perform all the calculations and conclusions. However, despite the use of a more simple approach, the results generated great learning and allowed these discoveries that will drive the continuation of the work for future and more precise conclusions.
- One central perspective for a possible future work is exploring the effects of this particle agglomeration, mainly trying to check the use of the particle clustering to increase C and reduce the focal area, expending less particles to perform the same deposition task. Moreover, verify how it is possible to synchronize the particle pulsing (simulated with bigger time step sizes) frequency with the laser frequency.
- It will be necessary for a better approach to model the gas-particle interaction, mainly because for this current work, it was used a one-way coupling model, which is not the better approach considering the clustering formation. This approach can be achieved by working directly with the solver. Therefore an in-house code can be used for this task, giving more extensive freedom to adapt the solution system to the proposed deposition situation.
- A material experiment of this deposition model is necessary to validate the computational model and, in the future, also computational results to modify the material experiment.

CHAPTER VII

BIBLIOGRAPHIC REFERENCES

ARRIZUBIETA, J. I. et al. Continuous coaxial nozzle design for LMD based on numerical simulation. **Physics Procedia**, v. 56, p. 429-438, 2014. https://doi.org/10.1016/j.phpro.2014.08.146

ARRIZUBIETA, Jon Inaki et al. Instantaneous powder flux regulation system for Laser Metal Deposition. **Journal of Manufacturing Processes**, v. 29, p. 242-251, 2017. https://doi.org/10.1016/j.jmapro.2017.07.018

ASTM International Committee F42 on Additive Manufacturing Technologies, **ASTM F279210 Standard Terminology for Additive Manufacturing Technologies**, ASTM, West Conshohocken, PA, 2009.

BALU, Prabu; LEGGETT, Perry; KOVACEVIC, Radovan. Parametric study on a coaxial multimaterial powder flow in laser-based powder deposition process. **Journal of Materials Processing Technology**, v. 212, n. 7, p. 1598-1610, 2012. https://doi.org/10.1016/j.jmatprotec.2012.02.020

BARTH, Timothy J.; BALDWIN, Barrett S. A one-equation turbulence transport model for high Reynolds number wall-bounded flows. 1990. https://doi.org/10.2514/6.1991-610

BENDEICH, Phil et al. Residual stress measurements in laser clad repaired low pressure turbine blades for the power industry. **Materials Science and Engineering: A**, v. 437, n. 1, p. 70-74, 2006. https://doi.org/10.1016/j.msea.2006.04.065

BOSIOC, A. et al. 2D LDV measurements and comparison with axisymmetric flow analysis of swirling flow in a simplified draft tube. In: **Proceedings of the 3rd IAHR International Meeting of Workgroup on Cavitation and Dynamic Problems in Hydraulic Machinery and Systems, Brno, Czech Republic**. 2009. p. 551-560.

BOUSSINESQ, Joseph. **Théorie de l'écoulement tourbillonnant et tumultueux des liquides dans les lits rectilignes a grande section**. Gauthier-Villars, 1897.

BRENNEN, Christopher Earls; BRENNEN, Christopher E. Fundamentals of multiphase flow. 2005. https://doi.org/10.1017/CBO9780511807169

CAMPBELL, Ian et al. Wohlers report 2019: 3D printing and additive manufacturing state of the industry: annual worldwide progress report. 2020.

CAMARGO, Italo Leite; LOVO, J. F. P.; ERBERELI, R.; COELHO, R. T.; SILVA, I. B. D.; FORTULAN, C. A. An Overview of Laser Engineered Net Shaping of Ceramics. **Matéria (Rio de Janeiro)**, v. 25, n. 1, 2020. https://doi.org/10.1590/S1517-707620200001.0916

CHOUHAN, A., Aggarwal, A., Kumar, A. (2018). Model Development in OpenFOAM for Laser Metal Deposition-based Additive Manufacturing Process. **Transactions of the Indian Institute of Metals**, 71(11), 2833-2838. https://doi.org/10.1007/s12666-018-1440-7

COURANT, Richard; FRIEDRICHS, Kurt; LEWY, Hans. Uber die partiellen Differenzengleichungen der mathematischen Physik**. Mathematische annalen**, v. 100, n. 1, p. 32-74, 1928. https://doi.org/10.1007/BF01448839

CROWE, C. T. Review Numerical models for dilute gas-particles flows. **Trans. of ASME J. of Fluid Eng**, v. 104, p. 297-303, 1982. https://doi.org/10.1115/1.3241835

DAVIDSON, L. Fluid mechanics, turbulent flow and turbulence modeling. eBook, Division of Fluid Dynamics, Dept. of Applied Mechanics, Chalmers University of Technology, Gothenburg. 2014.

DE SOUZA, Francisco José; DE VASCONCELOS SALVO, Ricardo; DE MORO MARTINS, Diego Alves. Large Eddy Simulation of the gasparticle flow in cyclone separators. **Separation and Purification Technology**, v. 94, p. 61-70, 2012. https://doi.org/10.1016/j.seppur.2012.04.006

DRAZIN, P. G.; REID, W. H. Hydrodynamic stability. **NASA STI/Recon Technical Report A**, v. 82, p. 17950, 1981.

DU, Min et al. A modified DSMC method for simulating gasparticle two-phase impinging streams. **Chemical Engineering Science**, v. 66, n. 20, p. 4922-4931, 2011. https://doi.org/10.1016/j.ces.2011.06.061

DUARTE, Carlos Antonio Ribeiro et al. Simulation of a new pipe design for erosion reduction in curves. 2017. Tese de Doutorado, Universidade Federal de Uberlândia, Uberlândia.

ELGHOBASHI, Said. On predicting particle-laden turbulent flows. **Applied scientific research**, v. 52, n. 4, p. 309-329, 1994. https://doi.org/10.1007/BF00936835

FERREIRA, E. et al. Numerical and experimental investigation of gas powder flow from coaxial nozzles in Laser Metal Deposition.2018

FERREIRA, Elise et al. Experimental and numerical analysis of gas/powder flow for different LMD nozzles. **Metals**, v. 10, n. 5, p. 667, 2020. https://doi.org/10.3390/met10050667

FERZIGER, Joel H.; PERIC, Milovan; STREET, Robert L. **Computational methods for fluid dynamics**. Berlin: springer, 2002. https://doi.org/10.1007/978-3-642-56026-2

FJORTOFT, Ragnar. **Application of integral theorems in deriving criteria of stability for laminar flows and for the baroclinic circular vortex**. Grondahl sons boktr., I kommisjon hos Cammermeyers boghandel, 1950.

FLUENT, ANSYS. ANSYS fluent theory guide 15.0. **ANSYS, Canonsburg, PA**, v. 33, 2013.

GERMANO, Massimo. A proposal for a redefinition of the turbulent stresses in the filtered Navier Stokes equations. **The Physics of fluids**, v. 29, n. 7, p. 2323-2324, 1986. https://doi.org/10.1063/1.865568

GIBSON, Ian; ROSEN, David; STUCKER, Brent. Directed energy deposition processes. In: **Additive Manufacturing Technologies**. Springer, New York, NY, 2015. p. 245-268. https://doi.org/10.1007/978-1-4939-2113-3_10

GIMENES, Giordhanne Bruno Carpaneda et al. Development of a Methodology for Toxic and Flammable Gases Sensors Positioning in Oil Platforms. **In: The 2008 Spring National Meeting**. 2008.

GLAZE, David J.; FRANKEL, Steven H. Stochastic inlet conditions for large-eddy simulation of a fully turbulent jet. **AIAA journal**, v. 41, n. 6, p. 1064-1073, 2003. https://doi.org/10.2514/2.2073

GORE, R. A.; CROWE, Clayton T. Effect of particle size on modulating turbulent intensity. **International Journal of Multiphase Flow**, v. 15, n. 2, p. 279-285, 1989. https://doi.org/10.1016/0301-9322(89)90076-1

GRAF, Benjamin et al. Design of experiments for laser metal deposition in maintenance, repair and overhaul applications. **Procedia Cirp**, v. 11, p. 245-248, 2013. https://doi.org/10.1016/j.procir.2013.07.031

GRAF, Benjamin et al. Additive process chain using selective laser melting and laser metal deposition. In: **Lasers in Manufacturing Conference**. 2015.

GRAF, Benjamin; GUMENYUK, Andrey; RETHMEIER, Michael. Laser metal deposition as repair technology for stainless steel and titanium alloys. **Physics Procedia**, v. 39, p. 376-381, 2012. https://doi.org/10.1016/j.phpro.2012.10.051

GUAN, Xiaoyi; ZHAO, Yaoyao Fiona. Numerical modeling of coaxial powder stream in laserpowder-based Directed Energy Deposition process. **Additive Manufacturing**, v. 34, p. 101226, 2020. https://doi.org/10.1016/j.addma.2020.101226

GUO, Nannan; LEU, Ming C. Additive manufacturing: technology, applications and research needs. **Frontiers of Mechanical Engineering**, v. 8, n. 3, p. 215-243, 2013. https://doi.org/10.1007/s11465-013-0248-8

HOUSE, M. A. et al. Rapid laser forming of titanium near shape articles: LaserCast. **In: 1996 International Solid Freeform Fabrication Symposium**. 1996.

IBARRA MEDINA, Juansethi Ramses. **Development and application of a CFD model of laser metal deposition**. 2013. Tese de Doutorado. University of Manchester.

IBARRA-MEDINA, Juansethi; VOGEL, Michael; PINKERTON, Andrew J. A CFD model of laser cladding: from deposition head to melt pool dynamics. In**: International Congress on Applications of Lasers Electro-Optics**. Laser Institute of America, 2011. p. 378-386.

JAVAID, Mohd; HALEEM, Abid. Current status and applications of additive manufacturing in dentistry: A literature-based review**. Journal of oral biology and craniofacial research**, v.9, n. 3, p. 179-185, 2019. https://doi.org/10.1016/j.jobcr.2019.04.004

JOGO COM 3 CASTANHAS EXTERNAS MONOBLOCO PARA PLACA UNIVERSAL Ø 160,0MM- JCE-K11160 MAWBRA, dispon´ıvel em https://www.worldtools.com.br/. Access in march 03, 2022.

HORNICK, John F.; **United States: 3D Printing Patent Landscape**, Mondaq, September 20, 2017

JOHNSON, Forrester T.; TINOCO, Edward N.; YU, N. Jong. Thirty years of development and application of CFD at Boeing Commercial Airplanes, Seattle. **Computers Fluids**, v. 34, n. 10, p. 1115-1151, 2005. https://doi.org/10.1016/j.compfluid.2004.06.005

KANTHA, Lakshmi H.; CLAYSON, Carol Anne. **Numerical models of oceans and oceanic processes**. Elsevier, 2000.

KOCH, J. L.; MAZUMDER, J. Rapid prototyping by laser cladding. In**: International Congress on Applications of Lasers Electro-Optics**. Laser Institute of America, 1993. p. 556-565.

KOLMOGOROV, Andrej Nikolaevich. Equations of turbulent motion in an incompressible fluid. In: **Dokl. Akad. Nauk SSSR**. 1941. p. 299-303.

KRANZ, Jannis; HERZOG, Dirk; EMMELMANN, Claus. Design guidelines for laser additive manufacturing of lightweight structures in TiAl6V4. **Journal of Laser Applications**, v. 27, n. S1, p. S14001, 2015. https://doi.org/10.2351/1.4885235

LARRANETA, Eneko; DOMINGUEZ-ROBLES, Juan; LAMPROU, Dimitrios A. Additive manufacturing can assist in the fight against COVID-19 and other pandemics and impact on the global supply chain**. 3D Printing and Additive Manufacturing**, v. 7, n. 3, p. 100-103, 2020. https://doi.org/10.1089/3dp.2020.0106

LEWIS, Gary K. et al. Directed light fabrication. In: **International Congress on Applications of Lasers Electro-Optic**s. Laser Institute of America, 1994. p. 17-26.

LEWIS, Gary K.; SCHLIENGER, Eric. Practical considerations and capabilities for laser assisted direct metal deposition. **Materials Design**, v. 21, n. 4, p. 417-423, 2000. https://doi.org/10.1016/S0261-3069(99)00078-3

LAÍN, Santiago; SOMMERFELD, Martin. Characterisation of pneumatic conveying systems using the Euler/Lagrange approach. **Powder Technology**, v. 235, p. 764-782, 2013. https://doi.org/10.1016/j.powtec.2012.11.029

LEE, Hyoung-Keun. Effects of the cladding parameters on the deposition efficiency in pulsed Nd: YAG laser cladding. **Journal of materials processing technology**, v. 202, n. 1-3, p. 321-327, 2008. https://doi.org/10.1016/j.jmatprotec.2007.09.024

LEVEQUE, Randall J. et al. **Finite volume methods for hyperbolic problems**. Cambridge university press, 2002. https://doi.org/10.1017/CBO9780511791253

LI, Wei; ZHANG, Xinchang; LIOU, Frank. Modeling analysis of argon gas flow rates effect on pre-mixed powder separation in laser metal deposition process and experimental validation. **The International Journal of Advanced Manufacturing Technology**, v. 96, n. 9-12, p.4321-4331, 2018. https://doi.org/10.1007/s00170-018-1909-x

LIN, Jehnming. Laser attenuation of the focused powder streams in coaxial laser cladding. Journal of laser applications, v. 12, n. 1, p. 28-33, 2000. https://doi.org/10.2351/1.521910

LIN, Jehnming. Numerical simulation of the focused powder streams in coaxial laser cladding. **Journal of Materials Processing Technology**, v. 105, n. 1-2, p. 17-23, 2000. https://doi.org/10.1016/S0924-0136(00)00584-7

LIN, J.; STEEN, W. M. Design characteristics and development of a nozzle for coaxial laser cladding. **Journal of Laser Applications**, v. 10, n. 2, p. 55-63, 1998. https://doi.org/10.2351/1.521821

LUPOI, R. et al. High speed titanium coatings by supersonic laser deposition**. Materials letters**, v. 65, n. 21-22, p. 3205-3207, 2011. https://doi.org/10.1016/j.matlet.2011.07.014

MENTER, Florian R. Two-equation eddy-viscosity turbulence models for engineering applications. **AIAA journal**, v. 32, n. 8, p. 1598-1605, 1994. https://doi.org/10.2514/3.12149

MOREIRA, Leonardo de Queiroz. Simulação de grandes escalas de jatos periódicos temporais utilizando a metodologia psedo-espectral de Fourier. 2007. Dissertação de Mestrado, Universidade Federal de Uberlândia, Uberlândia.

MOREIRA, L. Q., Modelagem Matemática de Jatos em Desenvolvimento Espacial Usando a Metodologia Pseudoespectral de Fourier. 2011. 191 f. Tese de Doutorado, Universidade Federal de Uberlândia, Uberlândia.

MORSI, S. A. J.; ALEXANDER, A. J. An investigation of particle trajectories in two-phase flow systems. **Journal of Fluid mechanics**, v. 55, n. 2, p. 193-208, 1972. https://doi.org/10.1017/S0022112072001806

NALAM, Yogesh et al. Gas flow study for development of a novel shielding gas nozzle for directed energy deposition processes using computational fluid dynamic simulations. In: IOP **Conference Series: Materials Science and Engineering**. IOP Publishing, 2021. p. 012016. https://doi.org/10.1088/1757-899X/1135/1/012016

NASA. NASA. Initial Page. Available in: <https://www.nasa.gov >. Accessed in: aug. 10, 2022.

NGO, Tuan D. et al. Additive manufacturing (3D printing): A review of materials, methods, applications and challenges. **Composites Part B: Engineering**, v. 143, p. 172-196, 2018. https://doi.org/10.1016/j.compositesb.2018.02.012

PETERS, B.; POZZETTI, G. Numerical analysis of powder deposition in direct material injection. **Granular Matter**, v. 22, n. 1, p. 1-12, 2020. https://doi.org/10.1007/s10035-019-0963-x

PETRAT, Torsten et al. Laser metal deposition as repair technology for a gas turbine burner made of inconel 718. **Physics Procedia**, v. 83, p. 761-768, 2016. https://doi.org/10.1016/j.phpro.2016.08.078

PAN, Heng; LIOU, Frank. Modeling of the Metal Powder Flow with Carrier Gas in Coaxial Nozzle for Direct Laser Deposition Process 523. In: **2004 International Solid Freeform Fabrication Symposium**. 2004.

PINKERTON, Andrew J.; LI, Lin. Modelling powder concentration distribution from a coaxial deposition nozzle for laser-based rapid tooling. **J. Manuf. Sci. Eng.**, v. 126, n. 1, p. 33-41, 2004. https://doi.org/10.1115/1.1643748

PINKERTON, Andrew J. Advances in the modeling of laser direct metal deposition. **Journal of laser applications**, v. 27, n. S1, p. S15001, 2015. https://doi.org/10.2351/1.4815992

POPE, Stephen B. **Turbulent flows**. 2001. https://doi.org/10.1017/CBO9780511840531

PRANDTL, Ludwig. 7. Bericht uber Untersuchungen zur ausgebildeten Turbulenz. ZAMM?¨ **Journal of Applied Mathematics and Mechanics/Zeitschrift fur Angewandte Mathematik und¨ Mechanik**, v. 5, n. 2, p. 136-139, 1925. https://doi.org/10.1002/zamm.19250050212

QI, Huan; MAZUMDER, Jyotirmoy; KI, Hyungson. Numerical simulation of heat transfer and fluid flow in coaxial laser cladding process for direct metal deposition. **Journal of applied physics**, v. 100, n. 2, p. 024903, 2006. https://doi.org/10.1063/1.2209807

RAYLEIGH, Lord. **Scientific Papers**, vol. 1, 1964. 1880. https://doi.org/10.1038/113570a0

RUIZ, Jose Exequiel et al. Study of the influence of shielding gases on laser metal deposition of Inconel 718 superalloy. **Materials**, v. 11, n. 8, p. 1388, 2018. https://doi.org/10.3390/ma11081388

SARGENT, John F.; SCHWARTZ, R. X. **3D printing: Overview, impacts, and the federal role. Congressional Research Service**, 2019.

SEBASTIAN, Johan Sebastian Grass Nunez Johan et al. Numerical and Experimental Analysis of Gas Flow in a Coaxial Nozzle Applied to Directed Energy Deposition (DED). International **Journal of Engineering Materials and Manufacture**, v. 6, n. 3, p. 102-113, 2021. https://doi.org/10.26776/ijemm.06.03.2021.01

SEXTON, L. et al. Laser cladding of aerospace materials. **Journal of Materials Processing Technology**, v. 122, n. 1, p. 63-68, 2002. https://doi.org/10.1016/S0924-0136(01)01121-9

SILVA, Renato Pacheco; DA SILVEIRA NETO, Aristeu; VALE, Millena Martins Villar. SIMULAÇÃO DO BREAKUP DE GOTÍCULAS DE FLUIDO EM UM ACOPLAMENTO EULERLAGRANGE DE DUAS VIAS, UTILIZANDO DIN MICA DOS FLUIDOS COMPUTACIONAL (CFD).

SILVEIRA-NETO, A **Escoamentos Turbulentos - Análise Física e Modelagem Teórica**. 1. ed. Uberlândia: Composer, 2020.

SPALART, Philippe; ALLMARAS, Steven. A one-equation turbulence model for aerodynamic flows. In: **30th aerospace sciences meeting and exhibit**. 1992. p. 439. https://doi.org/10.2514/6.1992-439

SUBRAMANIAM, Shankar. LagrangianEulerian methods for multiphase flows. **Progress in Energy and Combustion Science**, v. 39, n. 2-3, p. 215-245, 2013. https://doi.org/10.1016/j.pecs.2012.10.003

SVETLIZKY, David et al. Directed energy deposition (DED) additive manufacturing: Physical characteristics, defects, challenges and applications. **Materials Today**, v. 49, p. 271-295, 2021. https://doi.org/10.1016/j.mattod.2021.03.020

TAKEMURA, Shiho et al. Design of powder nozzle for high resource efficiency in directed energy deposition based on computational fluid dynamics simulation. **The International Journal of Advanced Manufacturing Technology**, v. 105, n. 10, p. 4107-4121, 2019. https://doi.org/10.1007/s00170-019-03552-1

TORO, Eleuterio F. Riemann solvers and numerical methods for fluid dynamics: a practical introduction. **Springer Science Business Media**, 2013. https://doi.org/10.1007/b79761

SUSAN-RESIGA, R. et al. Three-dimensional versus two-dimensional axisymmetric analysis for decelerated swirling flows. In: **Proceedings of the 13th International Conference on Fluid Flow**, Budapest, Hungary. 2009. p. 862-869.

VETTER, P. A.; ENGEL, Thierry; FONTAINE, Joel. Laser cladding: the relevant parameters for process control. In: **Laser Materials Processing: Industrial and Microelectronics Applications**. International Society for Optics and Photonics, 1994. p. 452-462. https://doi.org/10.1117/12.184751

VERSTEEG, Henk Kaarle; MALALASEKERA, Weeratunge. **An introduction to computational fluid dynamics: the finite volume method**. Pearson education, 2007.

VOLLER, V. R.; PORTE-AGEL, F. Moore's law and numerical modeling. **Journal of Computational Physics**, v. 179, n. 2, p. 698-703, 2002. doi:10.1006/jcph.2002.7083

WHITE, Frank M**. Fluid mechanics**. Tata McGraw-Hill Education, 1979.

WILCOX, David C. et al. **Turbulence modeling for CFD**. La Canada, CA: DCW industries, 1998. https://doi.org/10.1017/S0022112095211388

WOHLERS, T. Wohlers report 2020: 3D printing and additive manufacturing state of the industry: annual worldwide progress report. **Wohlers Associates**, 2020.

YAO, X. X. et al. Experimental and numerical studies of nozzle effect on powder flow behaviors in directed energy deposition additive manufacturing. **International Journal of Mechanical Sciences**, v. 210, p. 106740, 2021. https://doi.org/10.1016/j.ijmecsci.2021.106740

ZEKOVIC, Srdja; DWIVEDI, Rajeev; KOVACEVIC, Radovan. Numerical simulation and experimental investigation of gaspowder flow from radially symmetrical nozzles in laser-based direct metal deposition. **International Journal of Machine Tools and Manufacture**, v. 47, n. 1, p. 112-123, 2007. https://doi.org/10.1016/j.ijmachtools.2006.02.004

ZENG, Quanren et al. Advancement in additive manufacturing numerical modelling considerations of direct energy deposition process. In: Proceeding of the **14th International Conference on Manufacturing Research: Advances in Manufacturing Technology XXX**. Goy, YM Case, K.(eds.). Amsterdam: IOS Press. 2016. p. 104-109. https://doi.org/10.3233/978-1-61499-668-2-104

ZENG, Quanren et al. Numerical modelling of the gas-powder flow during the laser metal deposition for additive manufacturing. In: **Advances in Manufacturing Technology XXXI**: Proceedings of the 15th International Conference on Manufacturing Research, Incorporating the 32nd National Conference on Manufacturing Research, September 57, 2017, University of Greenwich, UK. IOS Press, 2017. p. 154.

ZHANG, Baicheng; CODDET, Christian. Numerical study on the effect of pressure and nozzle dimension on particle distribution and velocity in laser cladding under vacuum base on CFD. **Journal of Manufacturing Processes**, v. 23, p. 54-60, 2016. https://doi.org/10.1016/j.jmapro.2016.05.019

ZHONG, Chongliang et al. The influence of the powder stream on high-deposition-rate laser metal deposition with inconel 718. **Metals**, v. 7, n. 10, p. 443, 2017. https://doi.org/10.3390/met7100443

ZHU, Gangxian et al. Numerical simulation of metallic powder flow in a coaxial nozzle in laser direct metal deposition. **Optics Laser Technology**, v. 43, n. 1, p. 106-113, 2011. https://doi.org/10.1016/j.optlastec.2010.05.012